ABSTRACT

Title of dissertation: MAGNETIC ISLANDS PRODUCED BY RECONNECTION IN LARGE CURRENT LAYERS: A STATISTICAL APPROACH TO MODELING AT GLOBAL SCALES

Raymond Luis Lachica Fermo,
Doctor of Philosophy, 2011

Dissertation directed by: Professor James F. Drake
Department of Physics

Magnetic reconnection is a process responsible for the conversion of magnetic energy into plasma flows in laboratory, space, and astrophysical plasmas. A product of reconnection, magnetic islands have been observed in long current layers for various space plasmas, including the magnetopause, the magnetotail, and the solar corona. In this thesis, a statistical model is developed for the dynamics of magnetic islands in very large current layers, for which conventional plasma simulations prove inadequate. An island distribution function f characterizes islands by the flux they contain ψ and the area they enclose A. An integro-differential evolution equation for f describes their creation at small scales, growth due to quasi-steady reconnection, convection along the current sheet, and their coalescence with one another. The steady-state solution of the evolution equation predicts a distribution of islands in which the signature of island merging is an asymmetry in $\psi - r$ phase space. A Hall MHD (magnetohydrodynamic) simulation of a very long current sheet with large

numbers of magnetic islands is used to explore their dynamics, specifically their growth via two distinct mechanisms: quasi-steady reconnection and merging. The results of the simulation enable validation of the statistical model and benchmarking of its parameters. A PIC (particle-in-cell) simulation investigates how secondary islands form in guide field reconnection, revealing that they are born at electron skin depth scales not as islands from the tearing instability but as vortices from a flow instability. A database of 1,098 flux transfer events (FTEs) observed by Cluster between 2001 and 2003 compares favorably with the model's predictions, and also suggests island merging plays a significant role in the magnetopause. Consequently, the magnetopause is likely populated by many FTEs too small to be recognized by spacecraft instrumentation. The results of this research suggest that a complete theory of reconnection in large current sheets should account for the disparate separation of scales – from the kinetic scales at which islands are produced to the macroscale objects observed in the systems in question.

MAGNETIC ISLANDS PRODUCED BY RECONNECTION IN LARGE CURRENT LAYERS: A STATISTICAL APPROACH TO MODELING AT GLOBAL SCALES

by

Raymond Luis Lachica Fermo

Dissertation submitted to the Faculty of the Graduate School of the
University of Maryland, College Park in partial fulfillment
of the requirements for the degree of
Doctor of Philosophy
2011

Advisory Committee:
Professor James F. Drake, Chair/Advisor
Dr. Michael M. Swisdak
Professor Thomas M. Antonsen
Professor Daniel P. Lathrop
Professor Eve C. Ostriker

A limerick (and a plea) to Jim, Marc, Tom, Dan, and Eve:

A scientist lacking direction
Studied magnetic reconnection
But to get his degree
He'd never be free
From fear of his advisor's rejection

RLF

Composed on August 24, 2009
in response to a friend's challenge
to write a poem about my research.
May the work I've done here set me free.

Dedication

This thesis is dedicated to Telesforo Nacionales Lachica, or as I have always called him, *Lolo*. My grandfather was born April 15, 1912 in rural northern Philippines. He never surpassed the sixth grade because his mother – who encouraged him to study faithfully in school – passed away, leaving him to a father who preferred an extra body for the farm. I doubt anyone would've envisioned at the time the highest levels of education in the world just two generations after he left the sixth grade. But the educational values instilled by his mother remained, and were passed on to his children, who all attended college: Magdalena, Orlando, Potenciana, and Alejandro. Potenciana Perez Lachica received her degree in accounting from the University of the East, found a job in New York City, married Reymundo Almalvez Fermo, and then bore me. But it was *Lolo* who walked me to school daily, stayed with me while both parents worked, and encouraged me throughout my studies.

I keep just one framed picture in my bedroom. In it, I'm standing in a graduation gown just outside of the Stephen C. O'Connell Center at the University of Florida. I appear distracted, looking around, perhaps at another camera or maybe for my friends. But the center of the photo features a man standing next to me, attentively fixed upon the camera: *si Lolo*. He framed this photo for me along with a handwritten prayer he composed and a certificate for the President's Honor Roll that I had received at UF. He died on February 7, 2006, shortly after I started graduate school at the University of Maryland. Nevertheless, this photo of a man proudly standing with me is a reminder, not of a long-ago past, but of a present still happening. *Talagang salamat po. Mahal kita.*


UNIVERSITY OF
FLORIDA
President's Honor Roll
RAYMOND L FERMO

Acknowledgments

First, I thank my advisor, Prof. James F. Drake. Even with his many accomplishments, Jim has been a selfless advisor, helping me to grow as a scientist, showing me the ropes, and always putting my career needs first. I also thank Dr. Marc Swisdak, who has acted as a co-advisor in many respects, patiently helping me through my (many) daily problems. I am grateful to Prof. Tom Antonsen, Prof. Dan Lathrop, and Prof. Eve Ostriker for sitting on my thesis committee. To all of the members of our group, past and present, Prof. Paul Cassak (and Julie), Dr. Haihong Che, Dr. Yi-Hsin Liu (and Shania), Kevin Schoeffler, Tak-Chu Li, Joel Dahlin, Kalman Knizhnik, and Lora McMurtrie, I've truly enjoyed our shared learning experiences. I appreciate everyone at NASA Goddard who contributed the observational data for this research, welcomed me to their meetings, and gave helpful advice, especially Dr. David Sibeck, Dr. Yongli Wang, and Dr. Kyoung-Joo Hwang. I thank all the professors, scientists, and fellow students with whom I've interacted at GEM, SHINE, AGU, DPP, etc. I especially thank Prof. Merav Opher for the upcoming opportunity to work with her and her group at Boston University as a postdoc.

There are many faculty and staff at the Physics Department and IREAP worthy of my gratitude, but I name in particular Prof. Adil Hassam, Ed Condon, Mohini Kaul, Linda O'Hara, Jane Hessing, and Margaret Hess. I am also thankful for my fellow students in the Ph.D. program who helped me through it all: David Norris, Kevin and Ellie Twedt, Aron Wall, Brandon Anderson, Jupiter Bagaipo, Nick and Shaela Mecholsky (as well as Abram and my godson Roman). I'd be remiss not

to acknowledge those at the University of Florida who inspired me into a career in physics, especially Prof. Steven Detweiler for teaching my first university Physics course PHY 2048 (I subsequently changed my major to Physics) and Prof. Bernard Whiting for my undergraduate research experience with LIGO.

The many friends and family who have loved and supported me throughout are indispensable to me. My gratitude for the support of my mother and father knows no bounds. Graduate school was by no means a certainty in early 2005, but knowing where my heart lay, they encouraged me to apply with their blessing. My sister Christine has also been a huge part of my life, even if I don't tell her often enough. I'm proud to be her *Kuya*. I've received so much support from my family all across the globe, from Florida to New York to California to Germany and of course the Philippines. I truly miss the *pinsans*-night-outs with the cousins. Much love to all the Lumucsos, Medinas, Aquinos, Albays, and Cardinezes. Thanks also to Ate Clarisse "Bing" Andong, Ate Aileen Fermo Fernando (and family – I long to hear Isabella say *Ninong*), Kuya Rob Rebodos, Ate Grace Villanueva (and Aileen), and all my cousins everywhere. I have the best family ever. My achievements are not just my own but a credit to Fermos and Lachicas the world over.

I am truly fortunate to have been given wonderful friends; I can't imagine anything I've done to merit such a gift as these. I cannot possibly list by name everyone here, across the nation, and around the world, who has impacted my life, but I can start to try. First, a shout out to my fellow Gators, namely Palani Rathinasamy, Komal Kirtikar, Ryan Isaac, Atchar Sudhyadhom, Dana and Alison Ward, bonds which have lasted even as we've spread from UF throughout the country. I'm proud to

have known the families of Kevin and Jessica Hake, Joe and Daina Currano, Justin and Bernadette McClain, and their beautiful children Mercedes, Orlando, Marija, and John-Paul. I cannot forget my compatriot at the Little Sisters of the Poor, Bienvenida San Juan, who has been both a friend and my Filipina bonus-auntie-in-DC. I am profoundly grateful for Fr. George Wilkinson's spiritual guidance, and for having befriended Rod Cruz at Holy Redeemer and Ashwini Sebastian at Memorial Chapel. I can only begin to think of everyone in Communion and Liberation who has helped me to live with a new awareness and openness to life, but I'll just start with the CLU at UMD and CUA: Ellie Twedt, Caterina Poggi, Kevin Schoeffler, Abby Holtz, Chiara Tanzi, Meghan Cassidy, Ann Marie and Matt McPherson, Tyra Villadiego, Diana Liddi, Giacamo and Franny Fornasini, Emily Yang, John and Lauren Martino, Ellen and Marie Claire Roderick, Annie Devlin, Amy Sapenoff, Katrina Ten Eyck, Ryan Norris, Fr. Antonio Lopez, Fr. Pietro Rossotti, Fr. Paolo Prosperi, and in a particular way Dr. Liliana Maggioni, leader of my first SoC. I cherish what I've met through Msgr. Luigi Giussani and the faces of these friends.

In thanking all these family and friends "outside" of Physics, I emphasize that these relationships are not extraneous to my career. The acknowledgments here are not just academic. I am a better scientist because these people help me to seek, recognize, and love the truth in my life. Accompanied as I am, I can embrace my studying, my research, even my thesis-writing with the certainty that life is a gift, and neither my family nor my friends nor my work are extraneous to that life.

Lastly, I thank the God who has given me that life, and who, in Physics as in everything else, reveals to me every day a glimpse of the Mysteries of the universe.

Table of Contents

List of Figures

List of Abbreviations

AAS	American Astronomical Society
ACE	Advanced Composition Explorer
ACR	anomalous cosmic ray
AGU	American Geophysical Union
AIA	Atmospheric Imaging Assembly
CDF	cumulative distribution function
CME	coronal mass ejection
DPP	(American Physical Society) Division of Plasma Physics
ESA	European Space Agency
EUV	extreme ultraviolet
FTE	flux transfer event
GEM	Geospace Environment Modeling
GSM	Geocentric Solar Magnetospheric coordinate system
HXR	hard x-ray
ICME	interplanetary coronal mass ejection
IMF	interplanetary magnetic field
ISEE	International Sun-Earth Explorer
ISM	interstellar medium
IREAP	Institute for Research in Electronics and Applied Physics
LASCO	Large Angle and Spectrometric Coronagraph
LIGO	Laser Interferometer Gravitational-Wave Observatory
MESSENGER	Mercury Surface, Space Environment, Geochemistry and Ranging
MHD	magnetohydrodynamics
MMS	Magnetospheric Multiscale Mission
MST	Madison Symmetric Torus
MRX	Magnetic Reconnection Experiment
NASA	National Aeronautics and Space Administration
PIC	particle-in-cell (simulation)
RHESSI	Reuven Ramaty High Energy Solar Spectroscopic Imager
SAD	supra-arcade downflow
SADL	supra-arcade downflowing loop
SDO	Solar Dynamics Observatory
SGR	soft γ-ray repeater
SHINE	Solar, Heliospheric, and Interplanetary Environment
SOHO	Solar and Heliospheric Observatory
SSX	Swarthmore Spheromak Experiment
SUMER	Solar Ultraviolet Measurement of Emitted Radiation
SXR	soft x-ray
SXT	Soft X-ray Telescope
THEMIS	Time History of Events and Macroscale Interactions during Substorms
TRACE	Transition Region and Coronal Explorer
UT	Universal Time
VTF	Versatile Toroidal Facility
XRT	X-Ray Telescope

Chapter 1

A history of magnetic reconnection research

1.1 The pursuit of a theory for solar flares

The original impetus for the development of magnetic reconnection theory was a desire to understand the nature of solar flares. Among the first recorded observations of a solar flare[1] was the famed Carrington Event of 1859, independently observed by English amateur astronomers Richard Carrington and Richard Hodgson. In describing this experience, the former wrote, "While engaged in the forenoon of Thursday, Sept. 1, in taking my customary observation of the forms and positions of the solar spots, an appearance was witnessed which I believe to be exceedingly rare.... My first impression was that by some chance a ray of light had penetrated a hole in the screen attached to the object-glass, by which the general image is thrown into shade, for the brilliancy was fully equal to that of direct sun-light; but ... I saw I was an unprepared witness of a very different affair. I thereupon noted down the time by the chronometer, and seeing the outburst to be very rapidly on the increase, and being somewhat flurried by the surprise, I hastily ran to call some one to witness the exhibition with me, and on returning within 60 seconds, was mortified to

[1] A Chinese record dated December 9, 1638 possibly suggests a much earlier observation of a white light flare. The observer writes, "Within the Sun there was a black spot, and black and blue white vapors." [7]

find that it was already much changed and enfeebled." [19] In an article titled "On a curious appearance seen in the sun," Hodgson expressed a similar astonishment in front of what had just happened: "While observing a group of solar spots on the 1st September, I was suddenly surprised at the appearance of a very brilliant star of light, much brighter than the sun's surface, most dazzling to the unprotected eye, illuminating the upper edges of the adjacent spots and streaks, not unlike in effect the edging of the clouds at sunset; the rays extended in all directions; and the centre might be compared to the dazzling brilliancy of the star α *Lyræ* when seen in a large telescope with low power. It lasted for some five minutes, and disappeared instantaneously about 11.25 A.M." [78]. To this date, that very flare, the first one to be observed, was also probably the most powerful [32]; the subsequent magnetic storms generated auroras as far south as Cuba.

Fig. 1.1(a) shows a photograph similar to what Carrington and Hodgson might have seen. This image from 1891 was one of the first photographic images of a solar prominence by American solar astronomer George Hale [71]. Of course, the technology that enabled the scientists of that era to marvel at this newly discovered phenomenon (for Hodgson, a nineteenth century telescope with a 6-inch aperture) pales in comparison to the instruments used today to observe these events. So one could only imagine what awe might have been inspired in Carrington and Hodgson had they seen a solar prominence through the eyes of the recently launched Solar Dynamics Observatory (SDO) as in Fig. 1.1.

Even following this first observation, however, an explanation for solar flares eluded scientists for decades. Hale in 1908 showed that sunspots exhibit flow vor-

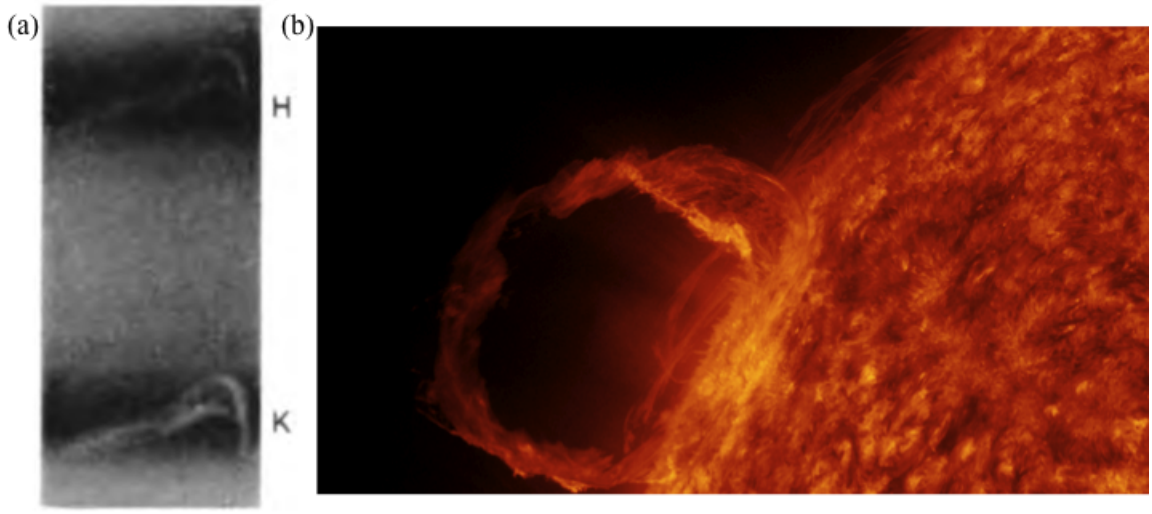

Figure 1.1: (a) A solar prominence eruption photographed on October 20, 1891 at 2:30 P.M. by George Hale in the hydrogen (H) and potassium (K) lines. Reprinted with permission from Hale (1892) [71]. ©1892 by the Insitute of Physics. (b) A solar prominence eruption imaged on March 30, 2010 by the Solar Dynamics Observatory's AIA (Atmospheric Imaging Assembly) shortly after its launch, showing a wavelength band centered around 304 Å, an extreme ultraviolet (EUV) emission line from He II at a temperature of approximately 50,000 K. Courtesy of NASA.

tices [73] and are accompanied by a strong magnetic field [72]. Nonetheless, because the coupling between these processes was poorly understood, models for the solar atmosphere relied solely upon hydrodynamics. In fact, writing about a "great magnetic storm" that immediately followed the Carrington Event of 1859, Carrington himself suggested that "while the contemporary occurrence may deserve noting, he [Carrington] would not have it supposed that he even leans towards hastily connecting them. 'One swallow does not make a summer.'" [19] Without a proper understanding of how magnetic fields interact with a plasma, and how these effects can propagate across the interplanetary medium, it was understandably difficult to connect two events separated by 17 hours when light takes only eight minutes to reach the earth from the sun. In an address to the Royal Society, Lord Kelvin proclaimed, "Guided by Maxwell's electromagnetic theory of light ... it seems as if we may also be forced to conclude that the supposed connexion between magnetic storms and sun-spots is unreal, and that the seeming agreement between the periods has been a mere coincidence." [92] The causal connection between solar phenomena and terrestrial magnetic storms was finally established in 1905 by British astronomer Edward Maunder, on the basis of a 27-day recurrence of magnetic storms correlated with the sun's 27-day rotation period [109]. Even still, an ultraviolet light theory of magnetic storms proposed in 1929 asserted that solar flares were no more than a burst of ultraviolet radiation that excited and ionized atoms in the upper atmosphere [108].

It would eventually be shown that the exorbitant amount of energy released in a flare (3×10^{32} erg) can only come from the magnetic field; neither thermal

nor gravitational energy would be adequate [131]. (The relevant calculations can be seen in Appendix A.) Therefore, the key needed to unlock this mystery was the connection between electromagnetics and hydrodynamics. The first step was defining the notion of a plasma. In 1918, the British mathematician Sydney Chapman proposed a theory that geomagnetic storms could be the result of a solar beam of either protons or electrons reaching the Earth's atmosphere [23]. When Frederick Lindemann rightly questioned whether repulsive effects would prevent such a beam from reaching Earth [103], Chapman revised his theory to a neutral beam consisting of both protons and electrons [24]. American chemist and Nobel laureate Irving Langmuir dubbed this new phase of matter a *plasma*, simply because it reminded him of the blood plasma [96].

The second and decisive step came in 1942 with the emergence of Hannes Alfvén's theory of magnetohydrodynamics (MHD) [3]. For a quasineutral plasma (number density $n \approx n_i \approx n_e$ for ions and electrons) in a homogeneous magnetic field B, the Swedish physicist showed that a perturbation to the density generates a perturbation in the magnetic field, and the field line tension acts as the restoring force. The resulting wave propagates along the magnetic field line with speed

$$c_A = \frac{B}{\sqrt{4\pi n m_i}} \tag{1.1}$$

where m_i is the ion mass. This first magnetohydrodynamic wave (since dubbed the *Alfvén wave*) inspired the ideal magnetohydrodynamics equations, which (true to the name given to them) combine Maxwell's equations from electromagnetism and the

inviscid Navier-Stokes equations (a.k.a. the Euler equations) from hydrodynamics:

$$\frac{\partial n}{\partial t} + \nabla \cdot (n\mathbf{v}) = 0 \tag{1.2}$$

$$nm_i \left(\frac{\partial \mathbf{v}}{\partial t} + \mathbf{v} \cdot \nabla \mathbf{v} \right) = \frac{1}{c} \mathbf{J} \times \mathbf{B} - \nabla p \tag{1.3}$$

$$\frac{\partial}{\partial t} \left(\frac{1}{2} nm_i v^2 + \frac{B^2}{8\pi} + \frac{p}{\gamma - 1} \right) + \nabla \cdot \left[\left(\frac{1}{2} nm_i v^2 + \frac{\gamma p}{\gamma - 1} \right) \mathbf{v} + \frac{c}{4\pi} \mathbf{E} \times \mathbf{B} \right] = 0 \tag{1.4}$$

$$\nabla \cdot \mathbf{B} = 0 \tag{1.5}$$

$$\frac{\partial \mathbf{B}}{\partial t} = -\frac{1}{c} \nabla \times \mathbf{E} \tag{1.6}$$

$$\mathbf{J} = \frac{c}{4\pi} \nabla \times \mathbf{B} \tag{1.7}$$

$$\mathbf{E} + \frac{\mathbf{v} \times \mathbf{B}}{c} = 0. \tag{1.8}$$

These equations are, respectively: the continuity equation, the momentum equation, the energy equation[2], Gauss' law for magnetism (absence of magnetic monopoles)[3], Faraday's law, Ampère's law[4], and Ohm's law. In these equations, t is time, n the number density, $\mathbf{v}$ the bulk flow velocity, m_i the ion mass, $\mathbf{J}$ the current density, $\mathbf{B}$ the magnetic field, $p = nT$ the pressure, T the temperature, γ the ratio of specific heats, c the speed of light, and $\mathbf{E}$ the electric field. As essentially the founding father of plasma physics, Hannes Alfvén was awarded the 1970 Nobel Prize in Physics.

1.2 The advent of magnetic reconnection theory

Armed with this new tool, physicists could now couple the plasma ejected by the prominences in Fig. 1.1, and the latent magnetic field observed in solar

[2]The heat flux $\mathbf{Q}$ is ignored to complete closure of the moment equations.

[3]Gauss's law for electricity $\nabla \cdot \mathbf{E} = 4\pi\rho$ is not used. The electric field $\mathbf{E}$ is given by Ohm's law.

[4]The displacement current term $-(1/4\pi)\partial\mathbf{E}/\partial t$ is ignored.

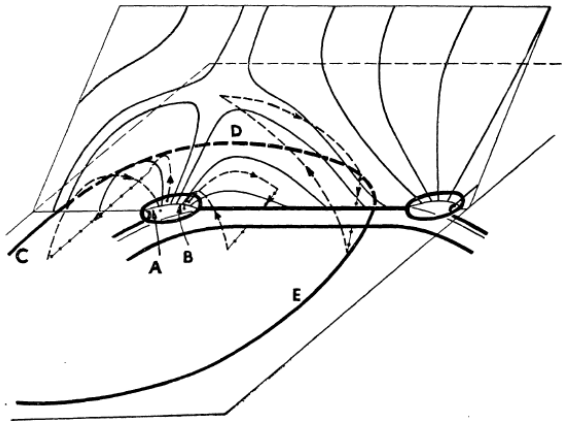

Figure 1.2: The magnetic fields within a plane connecting two sunspots, with a neutral point near the center, as proposed by Ronald Giovanelli. Reprinted with permission from Giovanelli (1947) [67]. ©1947 by the John Wiley & Sons, Inc.

active regions (regions containing sunspots). With this in mind, Australian physicist Ronald Giovanelli proposed in 1947 that flares could be the result of a current sheet containing a magnetic neutral point, as seen in Fig. 1.2 [67]. The magnetic field vanishes at this neutral point, implying that it must reverse direction on either side of the current sheet. Famed British astronomer Fred Hoyle discussed this problem with Giovanelli [81], and subsequently suggested it as a project for his graduate student, James Dungey.

In the coming years, Dungey would study oppositely directed magnetic field lines separated by a thin current sheet, as in Fig. 1.3(a). The picture in Fig. 1.3(b), however, would be impossible in ideal MHD, i.e., when the plasma has a high collision frequency ν, low resistivity η, and relevant length scales L much larger than the ion skin depth $d_i = c/\omega_{pi}$ (where c is the speed of light, ω_{pi} is the ion plasma

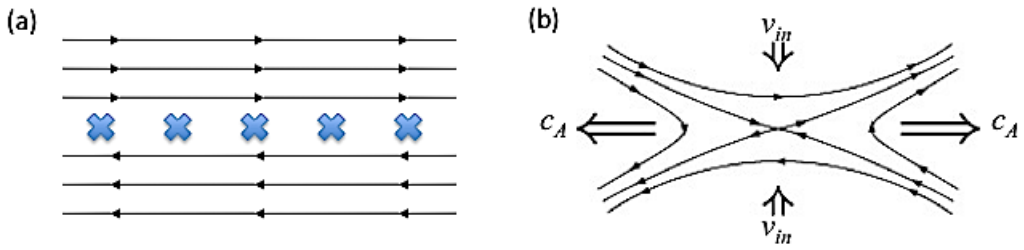

Figure 1.3: (a) The initial setup of oppositely directed magnetic fields separated by a sheet of current into the plane. (b) As the current sheet thins, upstream plasma is pulled into the x-line at the center, where the magnetic field lines cross-connect and accelerate away from at the center at the Alfvén speed (dragging plasma along with it) c_A.

frequency $\omega_{pi} = \sqrt{4\pi n_i e^2/m_i}$ and e is the electron charge). This is because for ideal MHD, substituting the ideal Ohm's law Eq. (1.8) into Faraday's law Eq. (1.6) gives the magnetic induction equation

$$\frac{\partial \mathbf{B}}{\partial t} = \nabla \times (\mathbf{v} \times \mathbf{B}) \tag{1.9}$$

where $\mathbf{v}$ is the bulk plasma flow. Helmholtz's second theorem states that when a field obeys this induction equation, the plasma remains "frozen" to that field. In other words, the bulk plasma flow carries not only the particles but also the magnetic field $\mathbf{B}$ along with it, so that two particles connected by a single magnetic field line at one time t would remain connected by the same field line at some later time $t + \Delta t$. This "frozen-in" condition therefore prohibits any changes in magnetic field line topology, as exhibited in Fig. 1.3(b).

On the other hand, Dungey proposed that by introducing a finite resistivity η

into Eq. (1.8),

$$\mathbf{E} = -\frac{\mathbf{v} \times \mathbf{B}}{c} + \eta \mathbf{J} \tag{1.10}$$

where $\mathbf{J}$ is the current density, the topology of magnetic field lines would be able to change near a magnetic neutral point. This would enable magnetic field lines to cross-connect at the x-line in the center of Fig. 1.3(b). The tension in the newly formed field lines would propel those field lines away from the x-line. Once outside of the dissipation region near the x-line, the frozen-in condition holds once again, and so the magnetic field drags plasma along with it downstream. Dungey coined the term *magnetic reconnection* to describe this process [48, 49].

Soon thereafter, at the 1956 International Astronomical Union Symposium on Electromagnetic Phenomena in Cosmical Physics in Stockholm, Sweden, the English physicist Peter Sweet presented his theory, which modeled solar flares by the reconnection of two bipolar magnetic fields as in Fig. 1.4(a) [174]. Sweet proposed that, with a finite resistivity and sufficiently low pressure, a hydrostatic equilibrium such as that in Fig. 1.4(b) is unstable to reconnection as the magnetic field flattens along the neutral line N (where the magnetic pressure is weakest). He draws an analogy with "the flattening of a motor tyre when loaded" in which, as long as the internal pressure P is not too strong, an external driving force F can force the gas to flow out at high speeds. Fig. 1.4(c) illustrates the same idea using an idealized hydrodynamic analogy, in which an external force pushes together two plates, forcing a high-speed outflow of the fluid between them. (It should be noted that the external driving force is not actually necessary for reconnection. Once reconnec-

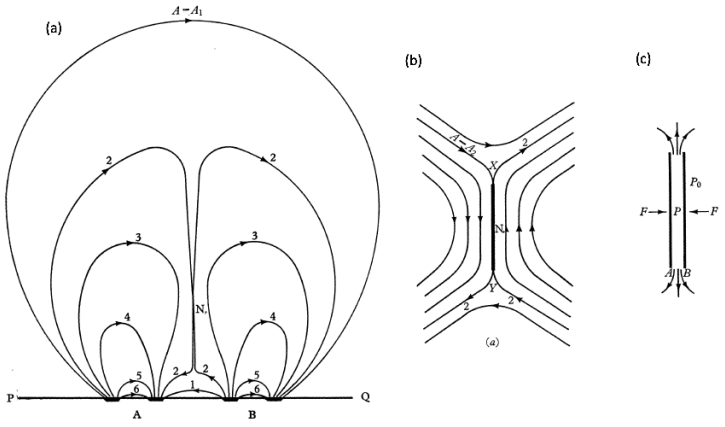

Figure 1.4: (a) Two bipolar magnetic fields reconnecting at the point N, according to the model proposed by Peter Sweet. (b) The reconnection configuration with a long, thin neutral line N. (c) An idealized hydrodynamic model, with external forcing F on two plates forcing the fluid in between to flow out the sides at high speeds. Reprinted with permission from Sweet (1958) [174]. ©1958 by the International Astronomical Union.

tion begins and plasma is expelled from the dissipation region, the density void in the dissipation region draws in new plasma upstream. Therefore, reconnection is a self-driven process.)

At this same conference, American astrophysicist Eugene Parker witnessed Sweet's talk and, on his way home, performed the scaling analysis of Sweet's theory using resistive MHD. Substituting Eq. (1.10) and Ampère's law Eq. (1.7) into Faraday's law Eq. (1.6) gives the resistive induction equation

$$\frac{\partial \mathbf{B}}{\partial t} = \nabla \times (\mathbf{v} \times \mathbf{B}) + \frac{\eta c^2}{4\pi} \nabla^2 \mathbf{B}. \tag{1.11}$$

In a steady state, the magnetic diffusion term must balance the dynamical term $\nabla \times (\mathbf{v} \times \mathbf{B})$. If we consider this for the dissipation region diagrammed in Fig. 1.5, with width δ corresponding to the characteristic length of the gradient in B_x, then balancing the right hand side of Eq. (1.11) gives us a relation for the inflow velocity

$$v_{in} \sim \frac{\eta c^2}{4\pi\delta}. \tag{1.12}$$

We consider the continuity equation $\partial n/\partial t + \nabla \cdot (n\mathbf{v}) = 0$ for a steady state and an incompressible plasma ($\nabla \cdot \mathbf{v} = 0$) in order to ensure mass conservation. If the dissipation region has length L as in Fig. 1.5, we can relate the inflow and outflow speeds to the aspect ratio:

$$\frac{v_{in}}{\delta} = \frac{v_{out}}{L}. \tag{1.13}$$

Likewise, if the energy required to push that outflow v_{out} comes from the upstream magnetic field B_x, then we can calculate the outflow speed explicitly from energy conservation:

$$\frac{1}{2} n m_i v_{out}^2 = \frac{B_x^2}{8\pi} \Longrightarrow v_{out} = \frac{B_x}{\sqrt{4\pi n m_i}} = c_A. \tag{1.14}$$

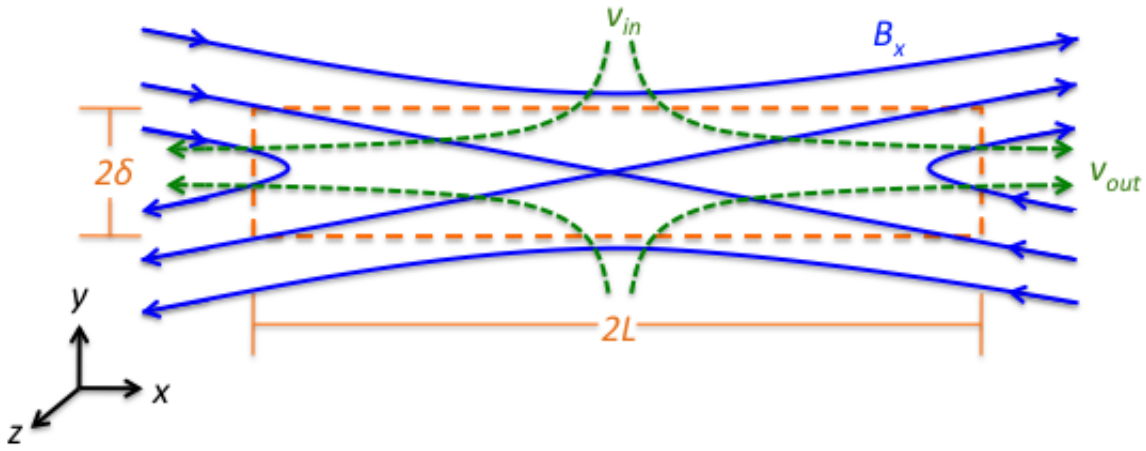

Figure 1.5: The dissipation region of a reconnection site (in orange), defined by its dimensions $L \times \delta$. The reconnecting magnetic field (in blue) is characterized by the upstream horizontal magnetic field B_x. The plasma flow (in green) enters the dissipation region with speed v_{in} and flows out with speed v_{out}.

Thus, the reconnection outflow speed is equal to the upstream Alfvén speed defined in Eq. (1.1). Substituting for v_{out} and δ from Eq. (1.13) into Eq. (1.12), we get

$$v_{in} = \sqrt{\frac{\eta c^2 c_A}{4\pi L}} \tag{1.15}$$

$$E' \equiv \frac{\delta}{L} = \frac{v_{in}}{v_{out}} = \sqrt{\frac{\eta c^2}{4\pi c_A L}} = S^{-1/2} \tag{1.16}$$

where E' is a dimensionless reconnection rate and $S = 4\pi c_A L/\eta c^2$ is the Lundquist number (also known as the magnetic Reynolds number). The reconnection rate is denoted as E' because it is proportional to the out-of-plane electric field E_z, which by the integral form of Faraday's law can be related to the rate at which magnetic flux enters the $x - z$ plane.

1.3 The time-scale problem

However, Sweet and Parker's model for reconnection had a major flaw: it was still too slow to explain observations. For the systems in question, L can be very large, the resistivity η quite low, and subsequently the Lundquist number S is exceptionally large. For example, in the corona, $L \sim 10^9$ cm, $\eta = 10^{-16}$ s, $S \sim 10^{14}$, and so $E' \sim 10^{-7}$. Although the time-scales for Sweet-Parker reconnection ($\tau_{SP} \sim L/v_{in} \sim 1.4 \times 10^7$ s ~ 4 months) are much faster than diffusive time-scales ($\tau_R \sim 4\pi L^2/\eta c^2 \sim 10^{14}$ s ~ 4 million years), this model is still far too slow to explain the solar flare that lasted but a disappointing 5 minutes for Carrington [19, 78].

In light of this limitation, Sweet, Parker, and others continued to seek a mechanism to enable faster reconnection – Joule dissipation, ambipolar diffusion, various forms of Sweet's mechanism – but without immediate success [124]. Finally, in 1963, Harry Petschek, an American physicist[5], presented a theory that employed standing slow shocks outside of the diffusion region to convert the magnetic energy into plasma flow [127]. In Sweet-Parker reconnection as in Fig. 1.6(a), nothing will prevent the dissipation region from expanding into the system size $2L$. In contrast, Petschek reconnection as in Fig. 1.6(b) can have plasma accelerated by the slow shocks (thick black lines) without having to go through the dissipation region, now

[5] "American physicist" is a rather lacking description. Harry Petschek was born in Prague, Czechoslovakia, to Jewish parents who fled the Nazi invasion. Besides his noteworthy contributions to physics, he invented an automated device for extracting DNA samples and collaborated on the invention of the intra-aortic balloon pump, a device for treating heart failure. He was also a civil rights activist, responsible for staging 1960s rallies in Lexington, Kentucky.

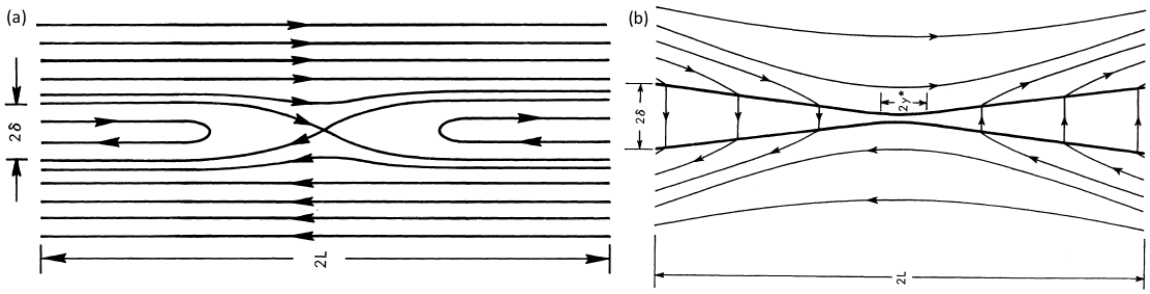

Figure 1.6: (a) The magnetic field configuration for Sweet-Parker reconnection, with a long dissipation region of length $2L$. (b) The magnetic field configuration for Petschek reconnection, with a much smaller dissipation region of length $2y^* \ll 2L$. The bold lines that define the boundary layer are slow shocks. Reprinted with permission from Petschek (1964) [127]. ©1964 by NASA Science and Technical Information Division.

much smaller ($2y^* \ll 2L$). As a result, Petschek calculates a reconnection rate E' that only weakly (logarithmically) depends on S, and coronal time-scales $\tau_P \sim 100$ s, fast enough to explain solar flares. When Petschek presented this theory at the AAS-NASA symposium, Peter Sweet enthusiastically proclaimed to Petscheck, "I am in favor of your theory, which I thoroughly approve. Dr. Parker and I have been living with this problem for several years and have got the feel of it. Your solution struck me at once as the solution for which we have been seeking." [127]

It would not prove to be so simple. Petschek reconnection was widely accepted as having solved the problem, but ultimately would fail to be validated by numerical simulations except with a locally enhanced resistivity [145]. Uniform resistivity failed to produce the slow-mode shocks predicted by Petschek [13]. Turbulence and

certain collisionless instabilities [83, 47] have been proposed as mechanisms for such an anomalous resistivity, but a more general theoretical explanation is still lacking.

An alternative to anomalous resistivity came about with the consideration of collisionless effects. In particular, it was discovered that the Hall effect, by which ions are decoupled from electrons, can trigger sufficiently fast reconnection rates to explain flares. The Hall effect is encapsulated by the $\mathbf{J} \times \mathbf{B}$ term in the generalized Ohm's law [139]

$$\mathbf{E} = -\frac{\mathbf{v} \times \mathbf{B}}{c} + \eta \mathbf{J} + \frac{\mathbf{J} \times \mathbf{B}}{nec} - \frac{\nabla \cdot \mathbf{P}_e}{ne} + \frac{m_e}{e^2} \frac{d}{dt} \left(\frac{\mathbf{J}}{n} \right). \tag{1.17}$$

The generalized Ohm's law adds to the resistive Ohm's law, Eq. (1.10), three additional terms on the right hand, which describe the Hall effect, the electron pressure, and electron inertia, respectively. The Hall term introduces the first intrinsic length scale into the MHD equations: the ion skin depth d_i, or the ion Larmor radius $\rho_i = c_s/\Omega_{ci} = \sqrt{\beta} d_i$ (where $c_s = \sqrt{T/m_i}$ is the sound speed, $\Omega_{ci} = eB/m_i c$ the ion cyclotron frequency, and $\beta = 8\pi nT/B^2$ the plasma beta parameter, the ratio between thermal and magnetic energy). Ideal MHD breaks down near the x-line precisely for this reason. As the ions near the magnetic field reversal, their gyro-orbits reverse direction mid-orbit, and the frozen-in condition is no longer valid. Meanwhile, the electrons remain frozen-in because they have a smaller Larmor radius on account of their much smaller mass $m_e \ll m_i$. They eventually decouple as well within their own electron dissipation region, but at even smaller scales, within the electron skin depth $d_e = c/\omega_{pe} = \sqrt{m_e c^2/4\pi n e^2} \ll d_i$ [42].

It is worth noting that the Hall effect does not in itself enable reconnection.

In fact, at the smallest scales near the x-line within the electron dissipation region, the Hall term vanishes because the electrons are decoupled from the magnetic field as well as the ions [42]. Some other dissipation mechanism is required to break field lines. Rather, the role of the Hall effect is to enhance the reconnection rate by opening the outflow region into a Petschek-like configuration, similar to Fig. 1.6(b) but without the requirement of standing slow shocks. In place of slow shocks, the Hall effect employs whistler waves to open the outflow nozzle (or a kinetic Alfvén wave if there is a guide field, a component of the magnetic field B_z perpendicular to the reconnecting plane) [43]. Suppose for instance that we treat the reconnected magnetic field (say, the leftmost and rightmost blue curves in Fig. 1.5) as a sine-wave perturbation to B_y with wave number k_y. Whistlers are dispersive waves (dispersion relation $\omega = k_y^2 c_{Ay} d_i$), meaning that the outflow speed ω/k_y increases proportionally as the scales get smaller (k_y gets larger). This is in contrast with non-dispersive waves (e.g., the Alfvén wave with dispersion relation $\omega = k_y c_{Ay}$), for which the outflow speed is a constant c_{Ay}, forcing a bottleneck at small scales.

Because whistler waves are circularly polarized, the Hall effect also tends to pull the magnetic field up and out of the plane in z. The result is a quadrupolar magnetic field as seen in Fig. 1.7, the primary signature for Hall reconnection [168]. This quadrupole structure has since been observed in the magnetopause [114, 152], magnetosheath [129], magnetotail [119, 118, 140], and laboratory plasmas [33, 136].

A major test for the Hall effect was the GEM Reconnection Challenge, an attempt to simulate reconnection using different types of simulation methods – resistive MHD, Hall MHD, hybrid, and full particle-in-cell – on the same initial con-

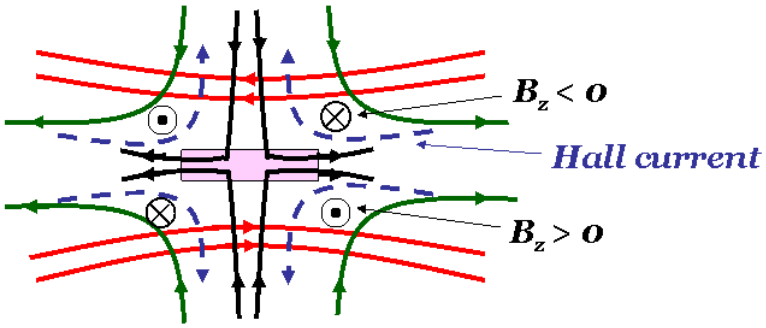

Figure 1.7: The Hall magnetic field signature predicted by Sonnerup [168]. Reprinted with permission from Cassak (2006) [20]. ©2006 by Paul Cassak.

ditions [11]. The resistive MHD simulation simply solves Eqs. (1.2)-(1.7) along with Eq. (1.10) numerically. Hall MHD adds the Hall term $\mathbf{J} \times \mathbf{B}/nec$ to Eq. (1.10). The hybrid simulation treats the electrons as a fluid but simulates the ions as particles. The particle-in-cell (PIC) simulation treats both ions and electrons as particles. Particles in hybrid and PIC simulations are stepped forward in time using

$$\frac{d\mathbf{x}}{dt} = \mathbf{v} \tag{1.18}$$

and the relativistic Lorentz force law

$$\frac{d(\gamma m \mathbf{v})}{dt} = q\left(\mathbf{E} + \frac{\mathbf{v} \times \mathbf{B}}{c}\right) \tag{1.19}$$

where here, $\gamma = 1/\sqrt{1 - v^2/c^2}$ is the Lorentz factor (as opposed to the ratio of specific heats in Eq. (1.4)). The latter three types of simulations all include the Hall term in one form or another. Fig. 1.8 summarizes the conclusion of this study, that while resistive MHD only produced slow Sweet-Parker reconnection, the other three simulations that include the Hall effect gave similarly fast reconnection rates.

One participant in the GEM reconnection challenge, Michael Shay, has gone

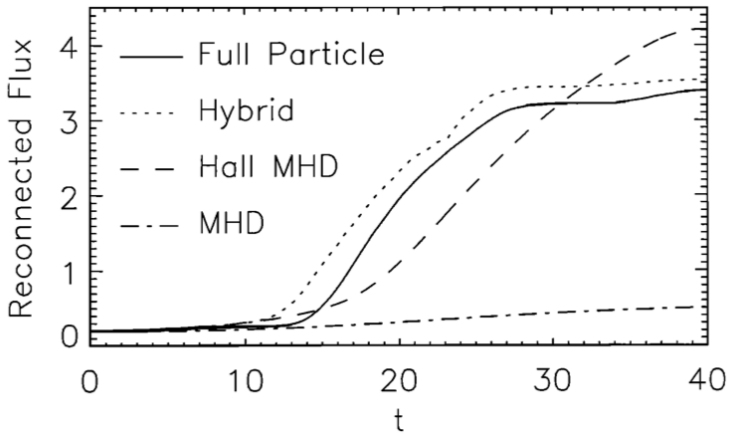

Figure 1.8: The reconnected magnetic flux as a function of time t for four different simulation methods: resistive MHD, Hall MHD, hybrid, and PIC. Reprinted with permission from Birn et al. (2001) [11]. ©2001 by the American Geophysical Union.

so far as to suggest that the reconnection rate is a universal constant of order $E' \sim 0.1$ independent of system parameters such as the mass ratio m_i/m_e, the resistivity η, or the system size L [153]. In the corona, this would give an inflow speed $v_{in} \sim E' c_A \sim 700$ km/s and a time-scale for reconnection of $\tau \sim 14$ s, certainly fast enough to explain flare energy release times, and orders of magnitude faster than Sweet-Parker reconnection $E_{SP} \sim 10^{-7}$, $\tau_{SP} \sim 4$ months.

Nonetheless, a theory for why the reconnection rate should take on this particular value of 0.1 has remained elusive and controversial. Alternative theories have sought fast reconnection through an anomalous resistivity, magnetic islands (to be discussed in Sec. 2.3), or various other terms in the generalized Ohm's law, Eq. (1.17).

1.4 Reconnection in the magnetosphere

The conversion of magnetic energy into plasma flows is not just confined to solar flares. One important application is in the Earth's magnetosphere, the region of space dominated by the Earth's magnetic field, which deflects the solar wind. The concept of a magnetosphere originated with Sydney Chapman and Vincenzo Ferraro in 1930 trying to develop a theory for the magnetic storms that Maunder had correlated with solar phenomena [109]. Chapman and Ferraro suggested that a "cloud" of plasma from the sun occasionally envelops the Earth, and the Earth's magnetic field would carve out a "cavity" in that cloud [25, 26]. In truth, the streams of particles from the sun are not from isolated clouds, but rather from a steady solar wind (as suggested by the German astronomer Ludwig Biermann in 1951 [9] and by Eugene Parker in 1958 [123], then verified observationally by the Soviet satellite Luna 1 in 1959 on its way to the moon), and the resulting cavity is not a temporary response to transient events but the magnetosphere. The intermittency of magnetic storms is due to coronal mass ejections (CMEs), a burst of plasma and magnetic field originating from the corona, often associated with solar flares.

Even as Dungey was first considering the applicability of his ideas to flares, he was already considering reconnection also in the context of the Earth's magnetosphere. In particular, Dungey specified two candidate locations in the magnetosphere where reconnection would take place: the magnetopause and the magnetotail [50]. The magnetopause is the border between the magnetosphere and the interplanetary magnetic field (IMF) facing the sun; the magnetotail is the extended region

of the magnetosphere opposite the sun. The Earth's dipole field points northward, so when the IMF points southward, the oppositely directed field lines reconnect at the magnetopause. (See field lines 1 and 1' in Fig. 1.9.) The magnetic field lines are suddenly opened (having only one footpoint in the Earth) and flung anti-sunward by the solar wind (lines 2-5 and 2'-5'). Eventually, those field lines pinch together in the magnetotail (lines 6 and 6') and reconnect a second time (lines 7 and 7'). The newly reconnected fields (lines 7 and 7') retreat Earthward back into a dipole configuration (line 8), then convect around the Earth (through the dusk-side) back to the dayside magnetosphere (line 9). The transfer of magnetic flux described here is called the Dungey cycle.

As in the sun, magnetic reconnection in the magnetosphere can also lead to particle energization. In the tail, Syun-Ichi Akasofu and Sydney Chapman suggested that magnetic disturbances (dubbed *substorms* by Chapman) generate auroras [2, 1], the result of accelerated plasma colliding with the atmosphere, and whose spectacular light shows in the skies have inspired great awe and wonder throughout human history. The tie-in with reconnection and the Dungey cycle was firmly established in 1966 by Donald Fairfield, when he showed that substorms are closely associated with the IMF B_z (the north-south component). Southward IMF triggers subsolar reconnection and generates frequent substorms, whereas northward IMF was associated with quiet intervals [59, 58].

Definitive evidence for magnetospheric reconnection came in in the 1970s, starting in 1971 with a Bengt Sonnerup paper on a magnetopause crossing by Explorer-12 [167], and later in 1978 from the ISEE spacecraft, from which Christo-

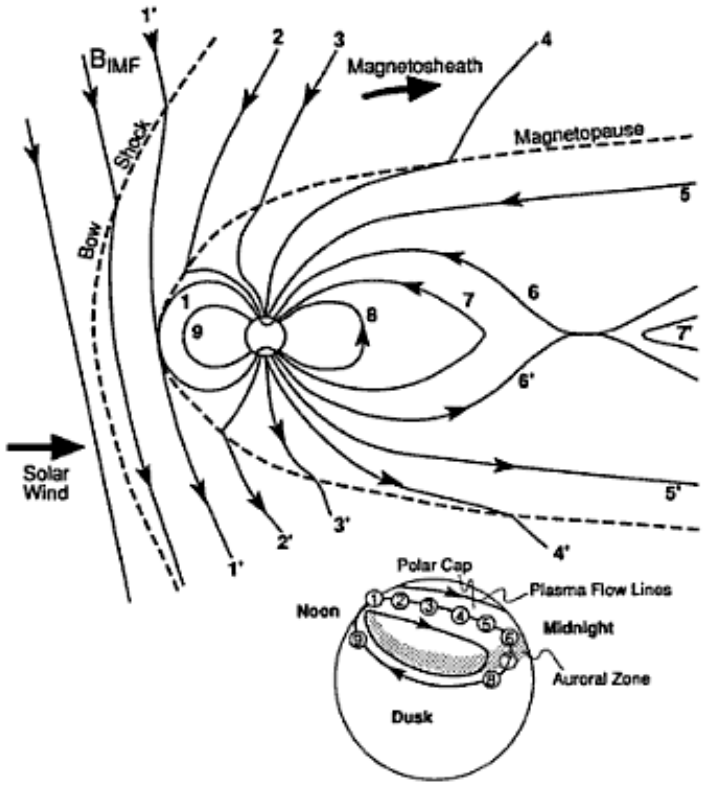

Figure 1.9: The Earth's magnetosphere, and interactions with the interplanetary magnetic field B_{IMF}. Lines 1-9 outline the convection of magnetic flux known as the Dungey cycle. Reconnection occurs at the magnetopause (lines 1 and 1') and in the magnetotail (lines 6 and 6'). The inset shows the footpoints of the respective field lines on Earth. Reprinted with permission from Hughes (1995) [84]. ©1995 by NASA Science and Technical Information Division.

pher Russell and Rick Elphic identified flux tubes generated by reconnection in the magnetopause [141, 142]. (The nature of these flux tubes shall be discussed in further detail in §2.2.1.) Similar structures were observed soon thereafter in the magnetotail [80, 56]. The relationship between reconnection in the magnetotail, current disruptions nearer to the Earth, and auroral events remains a significant area of current research and the primary mission of the THEMIS spacecraft [107, 4].

1.5 Reconnection in laboratory, space, and astrophysical plasmas

Although solar and magnetospheric plasmas served as the primary motivations for research in reconnection, the conversion of magnetic energy into plasma flows is in fact a ubiquitous process in many varied laboratory, space, and astrophysical plasmas.

Following the success of Dungey's reconnection model in space plasmas, Harold Furth, John Killeen, and Marshall Rosenbluth in 1963 wanted to study this new concept for applications in laboratory plasmas. In so doing, they determined conditions under which a collisional plasma with a magnetic field reversal would be linearly unstable to the formation of x-lines and subsequent magnetic islands [64]. They named this mode the *tearing instability* (to be discussed in greater detail in §2.1). This would prove to be important for the fusion community. The high temperatures required for fusion necessitated some means of confining this very hot plasma. *Tokamaks* are one such attempt to accomplish this confinement using a helical magnetic field wrapped around a torus. However, early tokamaks exhibited instabilities

that would disrupt confinement, such as the sawtooth crash (so named because the temperature would steadily increase, then suddenly crash to a much lower temperature before rising again, forming the shape of a sawtooth when plotted in time) [182]. In 1975, Soviet scientist Boris Kadomtsev identified the sawtooth crash as a reconnection event [89].

A number of experiments have delved into the reconnection problem for applications to both fusion and space plasmas. Some of these include the Madison Symmetric Torus (MST) at the University of Wisconsin [130], the Swarthmore Spheromak Experiment (SSX) at Swarthmore College [16], the Magnetic Reconnection Experiment (MRX) at the Princeton Plasma Physics Laboratory [186], and the Versatile Toroidal Facility (VTF) at the Massachusetts Institute of Technology [54].

Reconnection may also play a role in the coronal heating problem. The problem was first brought to light by the solar eclipse of August 7, 1869, during which Harkness and Young observed an inexplicable green emission line spectrum at 530.3 nm in the coronal spectrum [105]. Initially, this wavelength did not correspond to any known elements, so a new element called *coronium* was proposed [31]. Finally, in the 1930s and 1940s, German astronomer Walter Grotrian [70] and Swedish physicist Bengt Edlén [52, 53] identified this wavelength with multiply-ionized iron, Fe^{13+}. The discovery originally was not widely accepted because ionization to this level would require temperatures in the millions of kelvins, while the photosphere, much closer to the fusion energy source at the center of the sun, was observed at just ~ 5000 K. One theory proposed by the French astrophysicist Evry Schatzman

suggested that Alfvén waves and magneto-acoustic waves launched by turbulence could carry energy into the corona, and shock waves dissipate that energy as heat into the corona [150]. A competing theory put forth by Eugene Parker in 1987 asserted that random footpoint motion could lead to numerous small reconnection events called *nanoflares* [125, 126]. The magnetic energy is converted into plasma flows, but at such small scales, turbulence and viscosity quickly transforms it into heat. The power law behavior observed in statistical distributions of observed flare sizes is consistent with coronal heating by this mechanism [27]. Nonetheless, this remains a wide open question. The planned spacecraft Solar Probe Plus, a NASA mission schedule for a 2015 launch, will approach the sun to within $8.5R_\odot$ (where the solar radius $R_\odot = 6.955 \times 10^5$ km) from the surface of the sun and hopefully answer many of these lingering questions [65].

Although most *in situ* observational evidence for reconnection exists in the magnetosphere, where spacecraft can be directed towards the regions where reconnection is predicted to occur, observations of reconnection exhausts in the solar wind recently have become prevalent. In a 2006 paper by Phan et al., three separate spacecraft – ACE, Cluster-3, and Wind – measured a magnetic field reversal and reconnection exhaust in the solar wind [128]. The reconnection signatures in the three spacecraft were nearly identical despite spanning an astounding $390R_E$ (where the Earth radius $R_E = 6378.1$ km) in separation in the z direction (using the coordinate system of Fig. 1.5). The observations suggest that a very large and nearly two-dimensional reconnection event can operate at a quasi-steady state. Other observations in the solar wind have suggested that reconnection can occur in

conjunction with interplanetary coronal mass ejections (ICMEs, or CMEs that have escaped the corona into the interplanetary medium) [69, 68].

Reconnection is expected to be important for other planetary magnetospheres just as on Earth. MESSENGER flybys of Mercury have shown that the Hermean magnetosphere is perhaps even more sensitive to reconnection, on extreme occasions possibly even having all of its dayside flux depleted by reconnection [162, 163]. In Jupiter, both the Galileo and Ulysses spacecraft found reconnection signatures in the Jovian magnetotail and magnetopause [143, 117]. Likewise, the Cassini mission has shown that reconnection occurs in Saturn's magnetosphere [87, 110].

Further away from home, reconnection may also be taking place in the outer heliosphere. As the sun rotates, its dipole magnetic field twists into the famed Parker spiral [123], causing the heliospheric current sheet to flap like a ballerina skirt as in Fig. 1.10. One recent theory proposes that out past the termination shock, where the solar wind transitions from supersonic to subsonic, these flaps pile up and compress as they approach the heliopause, the border between the sun's magnetic field and that of the interstellar medium (ISM). The result is a sectored magnetic field and thin current sheets that can undergo reconnection. This has been proposed as a possible source of anomalous cosmic rays (ACRs) [98, 41, 122].

The dissipation of magnetic energy can easily be generalized to various astrophysical plasmas as well. Stellar flares have been observed on a number of sun-like stars such as Kappa Ceti [138], binary star systems such as II Pegasi [40], and even on magnetars such as SGR 1806-20 [85]. Reconnection is also a possible mechanism for supernova shocks to release their magnetic energy to generate X-ray gas in the

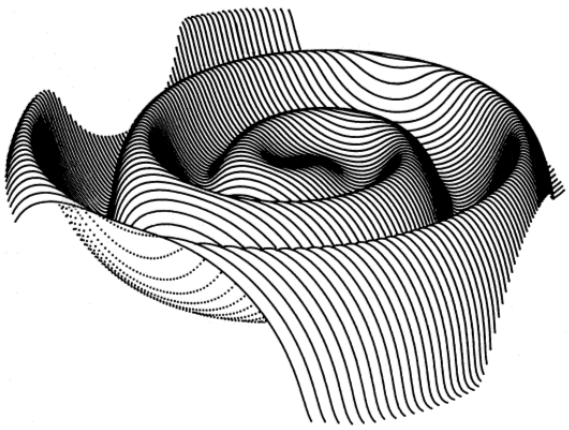

Figure 1.10: The heliospheric current sheet undergoing the Parker spiral. Reprinted with permission from Jokipii and Thomas (1981) [88]. ©1981 by the Institute of Physics.

galaxy [177]. Black hole accretion disks can also develop coronae with strong magnetic fields, which naturally would also be prone to flaring [14, 66]. Lastly, MHD models of the jets associated with rapidly spinning black holes suggest that the effect of reconnection on the global topology of magnetic fields can hinder jet formation [6].

Chapter 2

Magnetic islands in theory, simulations, and observations

An important byproduct of reconnection is the topological structure called a *magnetic island* (or *plasmoid* in some literature), the result of the magnetic field between two x-lines reconnecting into a closed structure. Islands can be a result of patchy reconnection, meaning the current sheet breaks up into multiple x-lines [99]. Fig. 2.1(a) exemplifies a simple 2-D magnetic island.

In our 3-D reality, magnetic islands take the form of flux tubes (or flux ropes), as in Fig. 2.1(b). Most reconnection simulations historically have been performed in 2-D, and observational evidence of extended x-lines in the solar wind [128] and of azimuthally long flux tubes in the magnetopause [61] suggests that, at least in some cases, the 2-D picture is a fair representation. The 3-D dynamics of flux tubes could be an important factor in other systems (e.g., the corona) but the 3-D nature of reconnection and of flux tubes is not yet well understood.

2.1 The tearing instability

As mentioned in §1.5, the theory of the tearing instability was first developed by Furth, Killeen, and Rosenbluth [64]. In this derivation of the tearing mode, we start with a magnetic field configuration called the *Harris sheet* [74], consisting of a

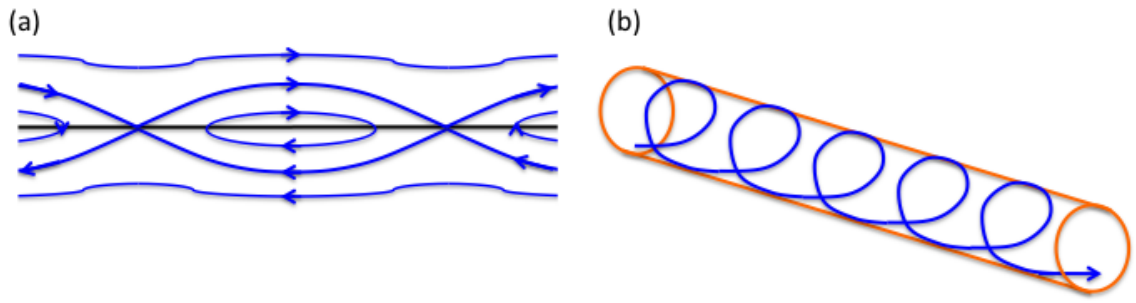

Figure 2.1: (a) A 2-D magnetic island enclosed by the separatrices of two x-lines. (b) A flux tube, the 3-D analogue of a magnetic island.

current sheet separating a magnetic field reversal:

$$\mathbf{B}_0(y) = B_0 \tanh\left(\frac{y}{w}\right)\hat{\mathbf{x}} \tag{2.1}$$

$$\mathbf{J}_0(y) = \frac{c}{4\pi}\nabla \times \mathbf{B}_0 = \frac{cB_0}{4\pi w}\,\mathrm{sech}^2\left(\frac{y}{w}\right)\hat{\mathbf{z}} \tag{2.2}$$

where B_0 is the asymptotic magnetic field and w the width of the current sheet. Both B_x and J_{z0} are shown in Fig. 2.2. An important feature of this configuration is that it is a Vlasov equilibrium, i.e., a Maxwellian distribution of particles is a steady state solution to the Vlasov equation

$$\frac{\partial f}{\partial t} + \mathbf{v}\cdot\nabla f + \frac{q}{m}\left(\mathbf{E} + \frac{\mathbf{v}\times\mathbf{B}}{c}\right)\cdot\frac{\partial f}{\partial \mathbf{v}} = 0. \tag{2.3}$$

Other similar configurations (e.g., the current slab $B_{x0} = B_0 y/w$ or the sine sheet $B_{x0} = B_0 \sin(\pi y/2w)$ for $|y| < w$, $B_{x0} = B_0|y|/y$ otherwise) will give similar results. We shall also assume that a pressure gradient or guide field (an out-of-plane component B_{z0}) exists to maintain pressure balance (i.e., $n_0 T_0 + B_0^2/8\pi = \text{constant}$) and ensure that the initial plasma is in equilibrium.

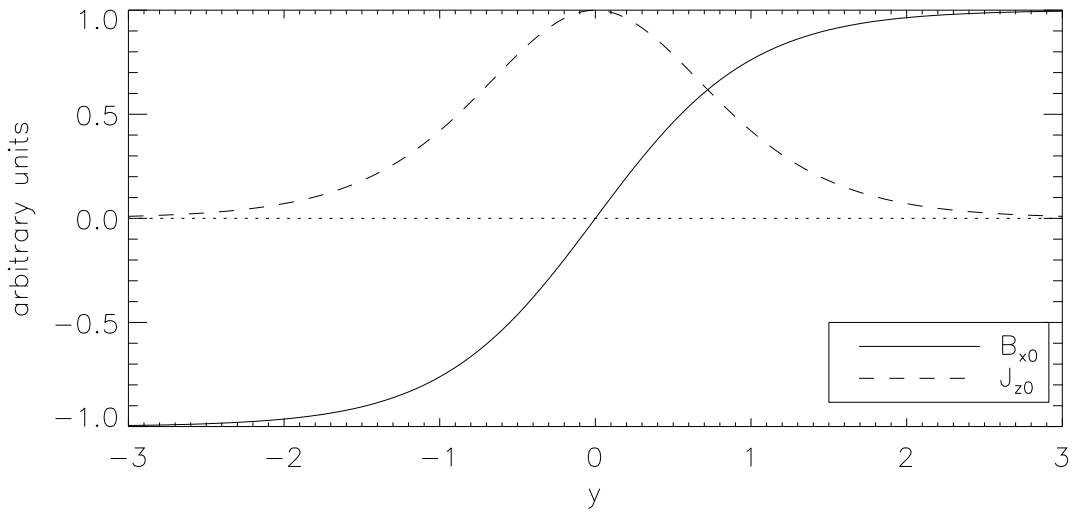

Figure 2.2: The Harris sheet B_{x0} (solid line) and J_{z0} (dashed line) described by Eqs. (2.1)-(2.2), for $w = 1$.

Because the Harris sheet is a one-dimensional equilibrium ($\partial/\partial x = \partial/\partial z = \partial/\partial t = 0$), a quantity ξ perturbed from its equilibrium value ξ_0 can be written as

$$\xi(x, y, t) = \xi_0 + \tilde{\xi}(y)e^{ikx - i\omega t} \tag{2.4}$$

for $k_z = 0$ modes as we shall assume here. If we apply such a perturbation to the Harris sheet configuration in resistive MHD and linearize the induction equation, Eq. (1.11), we get

$$\frac{\partial \tilde{\mathbf{B}}}{\partial t} = \nabla \times (\tilde{\mathbf{v}} \times \mathbf{B}_0) + \frac{\eta c^2}{4\pi}\nabla^2 \tilde{\mathbf{B}}. \tag{2.5}$$

In the resistive layer, the narrow region of y in which $\tilde{B}_y$ varies sharply, we write $\nabla^2 \approx \partial^2/\partial y^2$, in which case the y-component of Eq. (2.5) becomes

$$-i\omega \tilde{B}_y = ikB_{x0}\tilde{v}_y + \frac{\eta c^2}{4\pi}\frac{\partial^2 \tilde{B}_y}{\partial y^2}. \tag{2.6}$$

This equation shows why, even when η is very small for many of the plasmas we consider, the resistivity is essential for the tearing instability to occur. Without the resistivity term, in the reversal plane $y = 0$ where $B_{x0} = 0$, Eq. (2.5) can be satisfied only if $\tilde{B}_y = 0$, and the ideal MHD equations will produce an Alfvén wave but no instability. The resistivity allows a non-zero $\tilde{B}_y$ to develop across the current sheet and gives the plasma more freedom to find ways to dissipate the magnetic energy in B_{x0} through a $\tilde{B}_y$.

We now derive the instability criterion for the linear tearing mode from the 2-D reduced MHD equations. We define the flux function ψ such that

$$\mathbf{B} = \hat{\mathbf{z}} \times \nabla\psi + B_z\hat{\mathbf{z}} \tag{2.7}$$

and the stream function ϕ such that

$$\mathbf{v} = \hat{\mathbf{z}} \times \nabla\phi. \tag{2.8}$$

The former equation is valid since $\nabla \cdot \mathbf{B} = 0$; the latter likewise assumes that $\nabla \cdot \mathbf{v} = 0$. This assumption of incompressibility is broadly valid as long as the reconnection time scale is short compared with the magnetosonic propagation time across the system. Under these conditions, the magnetosonic wave smooths out the total pressure as reconnection proceeds so that local compressions do not take place and $\nabla \cdot \mathbf{v} = 0$. This assumption is most accurate during reconnection with a guide field where compressions of guide field rapidly propagate away from reconnection sites. With these definitions, Ampère's law Eq. (1.7) becomes $J_z = (c/4\pi)\nabla^2\psi$, Faraday's law Eq. (1.6) becomes $cE_z = \partial\psi/\partial t$, and substituting into the resistive

Ohm's law Eq. (1.10), we get for the z-component

$$\frac{\partial \psi}{\partial t} + \mathbf{v} \cdot \nabla \psi = \frac{\eta c^2}{4\pi} \nabla^2 \psi \tag{2.9}$$

The other reduced MHD equation comes from taking the z-component of the curl of the momentum equation, Eq. (1.3):

$$4\pi n m_i \left(\frac{\partial}{\partial t} \nabla^2 \phi + \mathbf{v} \cdot \nabla \nabla^2 \phi \right) = \mathbf{B} \cdot \nabla \nabla^2 \psi. \tag{2.10}$$

Linearizing Eqs. (2.9)-(2.10) with respect to perturbations $\tilde{\psi}$ and $\tilde{\phi}$ gives

$$\frac{\partial \tilde{\psi}}{\partial t} - B_{x0} \frac{\partial \tilde{\phi}}{\partial x} = \frac{\eta c^2}{4\pi} \nabla^2 \tilde{\psi} \tag{2.11}$$

$$4\pi n_0 m_i \frac{\partial}{\partial t} \nabla^2 \tilde{\phi} = B_{x0} \frac{\partial}{\partial x} \nabla^2 \tilde{\psi} - \frac{d^2 B_{x0}}{dy^2} \frac{\partial \tilde{\psi}}{\partial x}. \tag{2.12}$$

We then multiply Eq. (2.12) by $\tilde{\phi}$, then integrate over all space:

$$\int d^3x 4\pi n_0 m_i \tilde{\phi} \frac{\partial}{\partial t} \nabla^2 \tilde{\phi} = \int d^3x B_{x0} \tilde{\phi} \frac{\partial}{\partial x} \nabla^2 \tilde{\psi} - \int d^3x \frac{d^2 B_{x0}}{dy^2} \tilde{\phi} \frac{\partial \tilde{\psi}}{\partial x}. \tag{2.13}$$

Integrating by parts for each term and assuming that $\tilde{\phi}$ and $\tilde{\psi}$ vanish at ∞ gives us

$$-\int d^3x 4\pi n_0 m_i \nabla \tilde{\phi} \cdot \frac{\partial}{\partial t} \nabla \tilde{\phi} = -\int d^3x B_{x0} \frac{\partial \tilde{\phi}}{\partial x} \nabla^2 \tilde{\psi} + \int d^3x \frac{d^2 B_{x0}}{dy^2} \frac{\partial \tilde{\phi}}{\partial x} \tilde{\psi}. \tag{2.14}$$

From Eq. (2.11) we solve for $\partial \tilde{\phi} / \partial x$:

$$\frac{\partial \tilde{\phi}}{\partial x} = \frac{1}{B_{x0}} \left(\frac{\partial \tilde{\psi}}{\partial t} - \frac{\eta c^2}{4\pi} \nabla^2 \tilde{\psi} \right) \tag{2.15}$$

and substitute into the latter two terms of Eq. (2.14) to get

$$\begin{aligned} \int d^3x n_0 m_i \nabla \tilde{\phi} \cdot \frac{\partial}{\partial t} \nabla \tilde{\phi} = \frac{1}{4\pi} \int d^3x \left(\frac{\partial \tilde{\psi}}{\partial t} - \frac{\eta c^2}{4\pi} \nabla^2 \tilde{\psi} \right) \nabla^2 \tilde{\psi} \\ - \frac{1}{4\pi} \int d^3x \frac{1}{B_{x0}} \frac{d^2 B_{x0}}{dy^2} \left(\frac{\partial \tilde{\psi}}{\partial t} - \frac{\eta c^2}{4\pi} \nabla^2 \tilde{\psi} \right) \tilde{\psi}. \end{aligned} \tag{2.16}$$

The first term on the right hand side can be integrated by parts as before, with $\tilde{\psi} \to 0$ at ∞. Then collecting the $\partial/\partial t$ terms (using, for example, $\tilde{\psi}\partial\tilde{\psi}/\partial t = \frac{1}{2}\partial|\tilde{\psi}|^2/\partial t$) gives an equation for the energy integral:

$$\frac{\partial}{\partial t}\int d^3x \left(\frac{1}{2}n_0 m_i \left|\nabla\tilde{\phi}\right|^2 + \frac{1}{8\pi}\left|\nabla\tilde{\psi}\right|^2 + \frac{1}{8\pi}\frac{1}{B_{x0}}\frac{d^2B_{x0}}{dy^2}\left|\tilde{\psi}\right|^2\right) = \\ -\int d^3x \frac{\eta c^2}{16\pi^2}\left(\left|\nabla^2\tilde{\psi}\right|^2 - \frac{1}{B_{x0}}\frac{d^2B_{x0}}{dy^2}\tilde{\psi}\nabla^2\tilde{\psi}\right). \tag{2.17}$$

The first term on the left hand side is the kinetic energy of the perturbation. The latter two terms are the potential energy due to the magnetic field perturbation

$$\delta W_B = \frac{1}{8\pi}\int d^3x \left(\left|\nabla\tilde{\psi}\right|^2 + \frac{1}{B_{x0}}\frac{d^2B_{x0}}{dy^2}\left|\tilde{\psi}\right|^2\right). \tag{2.18}$$

The tearing mode is unstable when the perturbation releases magnetic energy, i.e., when $\delta W_B < 0$. The first term in δW_B is positive-definite and therefore stabilizes the tearing mode; the second term is negative, since for the Harris sheet described by Eq. (2.1),

$$\frac{1}{B_{x0}}\frac{d^2B_{x0}}{dy^2} = -\frac{2}{w^2}\mathrm{sech}^2\left(\frac{y}{w}\right). \tag{2.19}$$

Therefore, the instability is driven by a strong current gradient.

A simple scaling analysis on Eq. (2.18) readily produces the tearing instability criterion. The first term scales as $\nabla^2 \sim k^2$, whereas (for our Harris current sheet configuration) the latter scales as $B_{x0}^{-1}d^2B_{x0}/dy^2 \sim 1/w^2$, so the tearing mode is unstable when

$$kw \lesssim 1. \tag{2.20}$$

In other words, the Harris sheet is more unstable to long-wavelength (small k) perturbations. The physical reason for this criterion is that it requires energy to bend

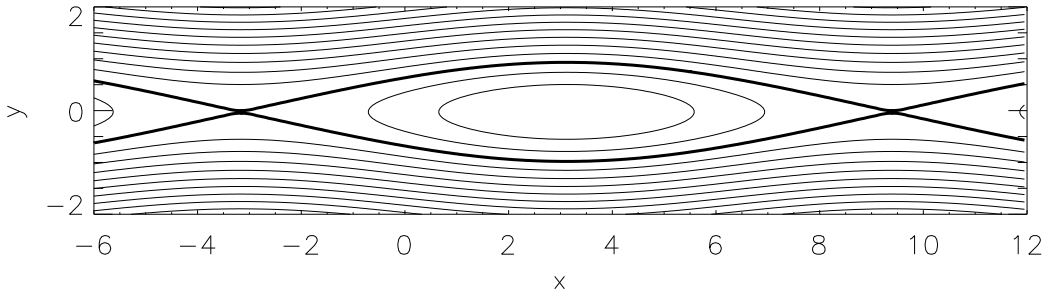

Figure 2.3: A magnetic island generated by the tearing mode, with $B_x = B_0 \tanh(y/w)$ and $B_y = \bar{B}_y e^{\gamma t} \cos(kx)$ with $B_0 = 1$, $w = 1$, $\bar{B}_y = 0.1$, $\gamma t = 0$, and $k = 0.5$. The thick lines are the separatrices that define the borders of the magnetic island.

field lines, and short-wavelength perturbations are highly bent. On the other hand, for sufficiently long wavelengths, the energy released by magnetic field annihilation more than compensates for the energy required to bend the field lines to the perturbation.

When the tearing mode goes unstable according to Eq. (2.20), the perturbation will grow exponentially as long as it remains in the linear phase. If we write the real part of $\tilde{B}_y$ at some particular time as $\tilde{B}_y = \bar{B}_y e^{\gamma t} \cos(kx)$ (where $\bar{B}_y$ is approximately independent of y near the resistive layer $y = 0$), we can plot magnetic field lines for this perturbation added to the Harris equilibirium Eq. (2.1). Fig. 2.3 shows how an elongated ($kw = 0.5$) magnetic island can grow from the tearing instability.

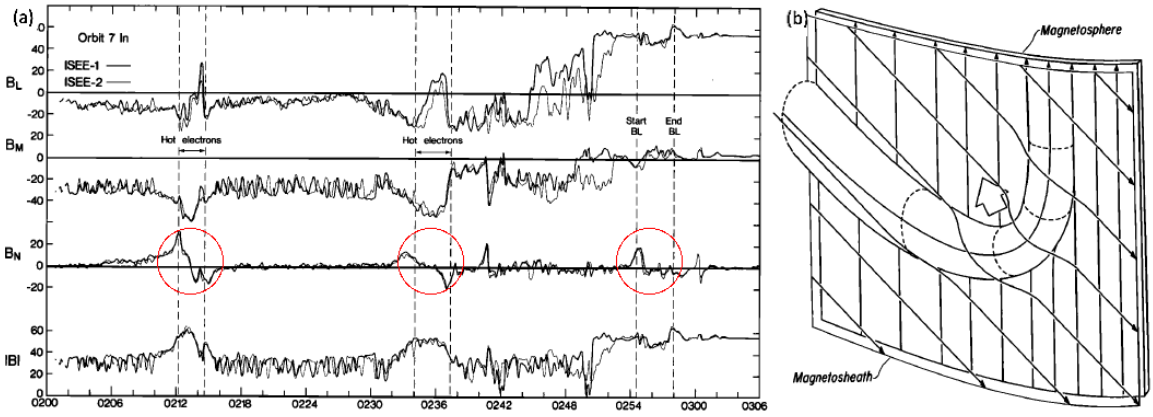

Figure 2.4: (a) A magnetopause crossing by ISEE-1 and ISEE-2 featuring the bipolar signatures in B_N now identified as flux transfer events. (b) A qualitative sketch by Russell and Elphic of how they interpreted this event as a flux tube on the surface of the magnetopause. Reprinted with permission from Russell and Elphic (1979) [142]. ©1979 by the American Geophysical Union.

2.2 Magnetic islands in nature

2.2.1 Flux transfer events on the magnetopause

One of the first *in situ* observations to evidence magnetic reconnection was published by Russell and Elphic [141, 142], who inferred reconnection by the presence of magnetic flux tubes. The ISEE-1 and ISEE-2 spacecraft crossed the magnetopause on November 8, 1977, and they found bipolar behavior in the component of the magnetic field perpendicular to the surface of the magnetopause, B_N, highlighted in Fig. 2.4(a). Russell and Elphic called these structures *flux transfer events* (FTEs) and interpreted them as flux tubes on the surface of the magnetopause, as sketched in Fig. 2.4(b).

In the original Russell and Elphic FTE picture, the flux tube on each side of the magnetopause is aligned with the local magnetosphere or magnetosheath magnetic field, respectively, and the reconnected flux tube kinks at the reconnection site, forming an elbow. A few years later, Lee and Fu expanded on this picture, arguing that FTEs are the result of multiple x-line (patchy) reconnection at the magnetopause, possibly due to the tearing instability [99]. Another idea independently developed in 1988 by Scholer [151] and Southwood [169] proposed that a single x-line with a bursty (time-dependent) reconnection rate can also generate flux tubes. These three descriptions are visually summarized in Fig. 2.5 [61]. A recent study of flux transfer events observed by ESA's Cluster spacecraft suggests that these flux tubes have a very long azimuthal extent, substantiating a 2-D picture of magnetic islands in opposition to the elbow reconnection model [61]. THEMIS observations of a 2007 flux transfer event found evidence for x-lines on both sides of the FTE [75]. The magnetic islands we shall consider in this thesis therefore shall be of the form proposed by Lee and Fu [99].

The interpretation of the bipolar signature of FTEs as a flux tube (or a magnetic island) is consistent with a spacecraft trajectory in Fig. 2.3 along x, where the magnetopause surface is basically the $y = 0$ plane. Even though the spacecraft crosses the magnetopause, the FTE is in fact traveling along the current sheet much faster than the spacecraft. Effectively, ISEE is standing still while the FTE flows through it. We imagine the spacecraft at the magnetopause traveling towards positive x and measuring B_y, corresponding to B_N in Fig. 2.4(a). Initially, at the first x-line near $x = \pi$, $B_y = 0$. Then, as it passes through the island, the spacecraft

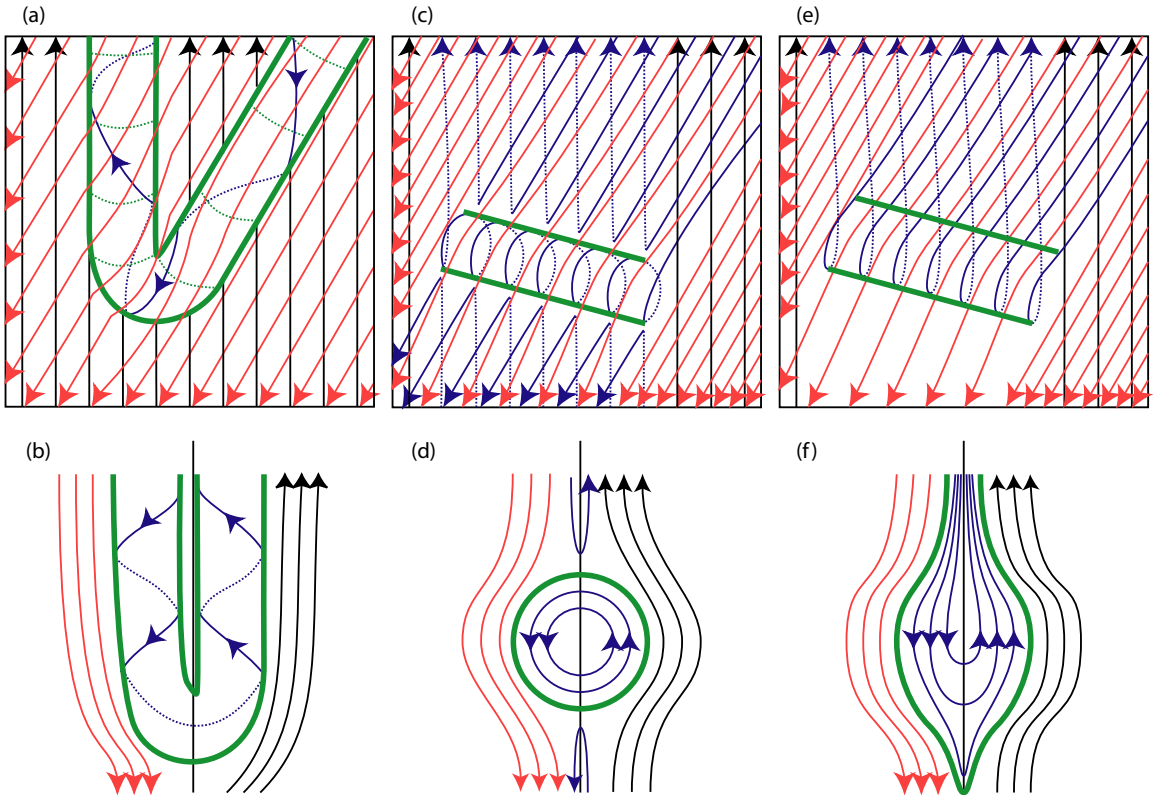

Figure 2.5: Three different models for FTEs. (a)-(b) The Russell and Elphic elbow reconnection model [141, 142]. (c)-(d) The Lee and Fu patchy reconnection model [99]. (e)-(f) The Scholer [151] and Southwood [169] bursty reconnection model. The top row (a), (c), and (e) shows views along the magnetopause normal; the bottom row (b), (d), and (f) shows views tangential to the magnetopause. Black curves represent closed magnetosphere field lines, red curves the magnetosheath field lines, blue curves reconnected field lines, and green curves the borders of the FTE. Reprinted with permission from Fear et al. (2008) [61]. ©2008 by the European Geosciences Union.

encounters a positive B_y. (Note that the magnetic field is clockwise within the island to match $B_x > 0$ for $y > 0$ as required by Eq. (2.1).) Then, B_y goes to 0 at the o-line in the center of the island and proceeds to a negative B_y at the other end of the island. Finally, B_y returns to 0 at the right-hand x-line. The result is a bipolar B_y similar to those highlighted in Fig. 2.4(a). This will be discussed in greater detail in §7.1.

Flux transfer events remain an area of emphasis in space research because of their role at the beginning of the Dungey cycle. As spacecraft capabilities improve, we are starting to see FTEs as small as 200 km, generated within the Hall electromagnetic field region [178]. The upcoming Magnetospheric Multiscale Mission (MMS), with capabilities of resolving these inertial scales, will shine more light on the microphysics of reconnection and FTE formation. Meanwhile, simulations and observations continue to explore their creation [135, 38, 178], their internal structure [60, 188, 161], their evolution [121, 189], and the conditions under which they form [184, 185].

2.2.2 Plasmoids in the magnetotail

In 1979, Edward W. Hones, Jr. predicted similar structures in the magnetotail generated by a magnetic x-line $10 - 25R_E$ from the Earth [79]. This prediction was borne out a few years later in 1984, when ISEE-3 detected these plasmoid structures flowing tailward (anti-sunward) at roughly $X_{GSM} \sim -220R_E$ [80]. (In GSM coordinates, the origin is the Earth, X_{GSM} points towards the sun, Y_{GSM}

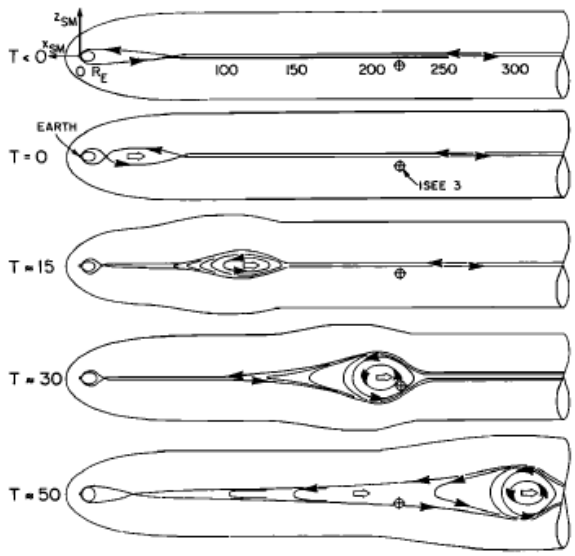

Figure 2.6: A plasmoid structure in the magnetotail flowing tailward. Based on the flow speed of $500 - 1000$ km/s and the ~ 30 min delay from observed auroral activity, it was estimated that the plasmoid was formed at $X_{GSM} \gtrsim -70R_E$ before flowing past ISEE-3 at $X_{GSM} \approx -220R_E$. Reprinted with permission from Hones et al. (1984) [80]. ©1984 by the American Geophysical Union.

roughly duskward, and Z_{GSM} roughly northward, so that the $X - Z$ plane contains the dipole axis.) This is illustrated in Fig. 2.6 [80]. As with the FTEs discussed in §2.2.1, plasmoids in the magnetotail can be identified by a bipolar signature in B_Z [116, 29].

These tailward flowing plasmoids are likely generated by reconnection in the tail at $20 - 30R_E$ [115]. Of course, earthward flowing plasmoids have also been seen [190], even as a result from reconnection in the near tail $X_{GSM} \sim -10R_E$ [164]. More recently, spacecraft have been able to explore the small-scale x-line structure of the magnetotail plasma sheet, in particular the Hall electromagnetic field and the

formation of secondary islands in the extended electron current sheet [51, 28].

An important result related to these islands in the magnetotail was the discovery that energetic electrons peaked in flux within them [29]. The observed energies of these highly energetic electrons (as high as 100 keV) cannot be explained by simply invoking the traditional reconnection outflow c_A, even at its largest possible values corresponding to only about ~ 2 keV. The data suggests that some other mechanism, likely involving magnetic islands, is responsible for electron acceleration. One such theory will be discussed further at the end of §2.3.

2.2.3 Supra-arcade downflows in the solar corona

For quite a while, the canonical picture for solar flares has appeared something like Fig. 2.7 [158, 180]. In the soft x-ray (SXR) loop, the observed radiation mostly comes from the spectral lines of thermal plasma heated to millions of kelvins. In the hard x-ray (HXR) region in Fig. 2.7, the radiation is dominated by *brehmsstrahlung* from nonthermal (accelerated) electrons decelerating as they come into contact with thermal ions. According to this model, the accelerated plasma gains its energy at a reconnection x-line above the loop, as observed by Lin et al. (2005) [100]. The downward reconnection outflow generates the hard x-rays, while upward reconnection outflow can escape the corona as a coronal mass ejection.

How is the plasma accelerated to such high energies? Observed emissions allude to the fact that the bulk of the magnetic energy goes into energetic ($10 - 100$ keV) electrons [101, 102, 57, 95]. RHESSI has observed electron energies $>$

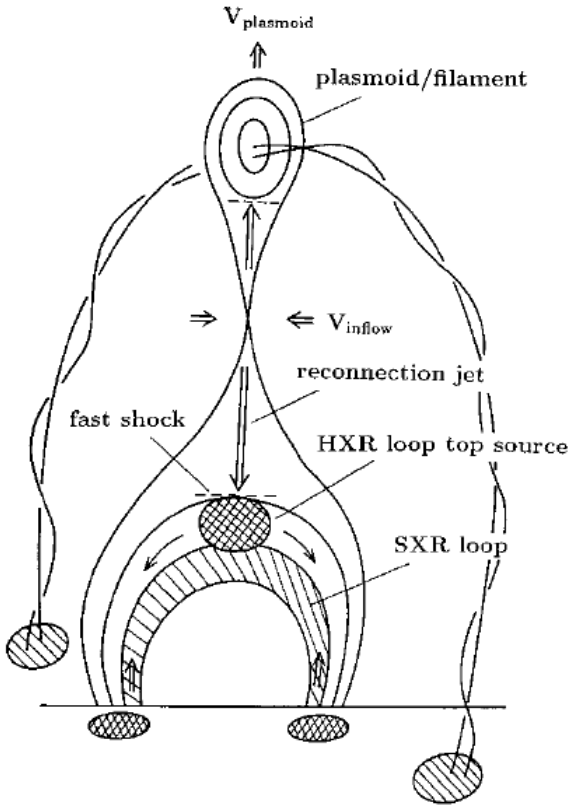

Figure 2.7: The canonical single x-line model for solar flares. Reprinted with permission from Shibata et al. (1995) [158]. ©1995 by the Institute of Physics.

300 keV (and up to $\sim$ 10 MeV) and ions $>$ 30 MeV (up to $\sim$ 1 GeV), meaning that an adequate theory must include a common acceleration mechanism for both species [160]. Yet as with the energetic electrons in the magnetotail [29] discussed in §2.2.2, the energies observed here cannot be attained from a simple Alfvénic reconnection outflow jet. Neither is the parallel electric field a suitable mechanism for particle acceleration because 3-D PIC simulations of guide field reconnection show that it remains localized within density cavities along the separatrices [133]. Mounting evidence suggests that the single x-line model does not explain observations of energetic particles.

An alternative to the single x-line model of Fig. 2.7 is one where bursty or patchy reconnection generates many magnetic islands. Observational evidence for this kind of picture is presented in Fig. 2.8, which shows a 2002 TRACE image of "tadpole"-like structures flowing down into the postflare loop [156]. Comparing these results with MHD simulations of localized reconnection on a current sheet, Linton and Longcope interpreted these "tadpoles" as reconnected flux tubes descending from the reconnection site higher in the corona [104]. McKenzie had seen similar structures using lower resolution Yohkoh data and came to a similar interpretation of these dark voids [111], later using an automated algorithm to perform a wide-ranging statistical study of *supra-arcade downflows* (SADs) seen by TRACE, SOHO/LASCO, SOHO/SUMER, and Hinode/XRT [112]. Other structures seen in post-CME arcades, seen as downflowing shrinking loops called *supra-arcade downflowing loops* (SADLs), have been identified as instances of SADs from a perpendicular viewing angle [149].

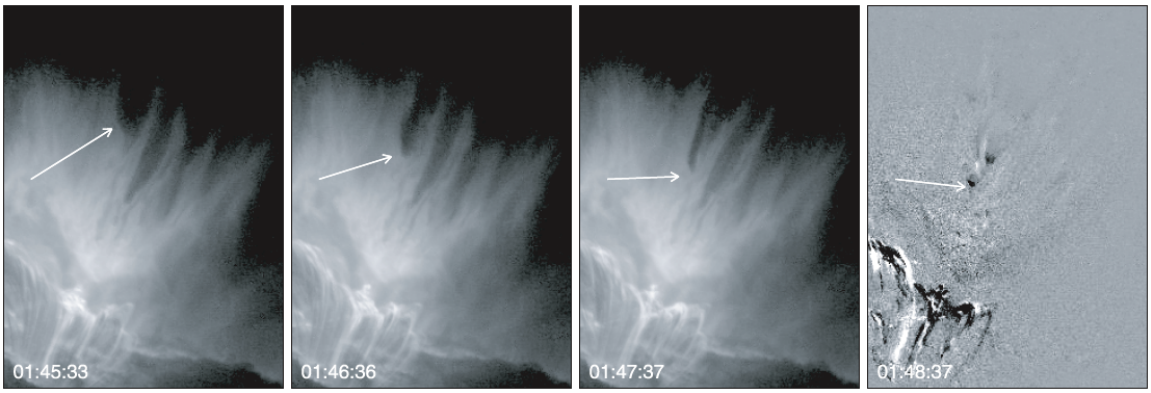

Figure 2.8: A 195 Å filtergram of an April 21, 2002 flare on the west limb, as recorded by TRACE. The vertical dimension of each panel is approximately 117 Mm. The postflare loops visible in the lower left are emitting in Fe XII 195 Å. The diffuse plasma cloud in the center (corresponding to the Fe XXIV 192 Åline) is penetrated by downflowing "tadpole"-shaped voids, highlighted by the arrow in successive images. The fourth panel is a difference image, indicating the change from 0147:37 UT to 0148:37 UT. Reprinted with permission from Sheeley et al. (2004) [156]. ©1995 by the Institute of Physics.

SOHO/LASCO images also have revealed very long current sheets left behind in the wake of an ejected CME [94, 173]. Large, bright, blob-like structures seen on these current sheets could also be interpreted as magnetic islands generated by bursty reconnection [100]. These current sheets are observed to be very thick, much thicker than the predictions of reconnection models employing classical or anomalous resistivity [30]. A possible explanation for the observed thickness is the presence of many magnetic islands along the course of the current sheet.

2.3 Recent theories and simulations of islands

2.3.1 Islands and fast reconnection in MHD

Tearing mode notwithstanding, the theory of island formation remains incomplete. The tearing mode is only a linear theory; it allows a small perturbation to grow, but the theory breaks down once the system escapes the linear phase of the instability.

MHD simulations have shown that islands form for sufficiently high Lundquist number $S = Lc_A/\eta > S_{crit}$, empirically estimated at $S_{crit} \approx 10^4$ [13, 97, 144, 22, 82]. Fig. 2.9(a) shows islands generated in a resistive MHD simulation with Lundquist number $S = 3 \times 10^6$ [82]. A more recent theory by Loureiro et al. (2007) based on the reduced MHD equations predicts a plasmoid instability with growth rate $\gamma \sim S^{1/4} c_A/L$ (where L is the length of the current sheet) [106]. The theory is supported by MHD simulations [144], but again, only through the linear growth stage, before other dynamics such as island convection and coalescence become

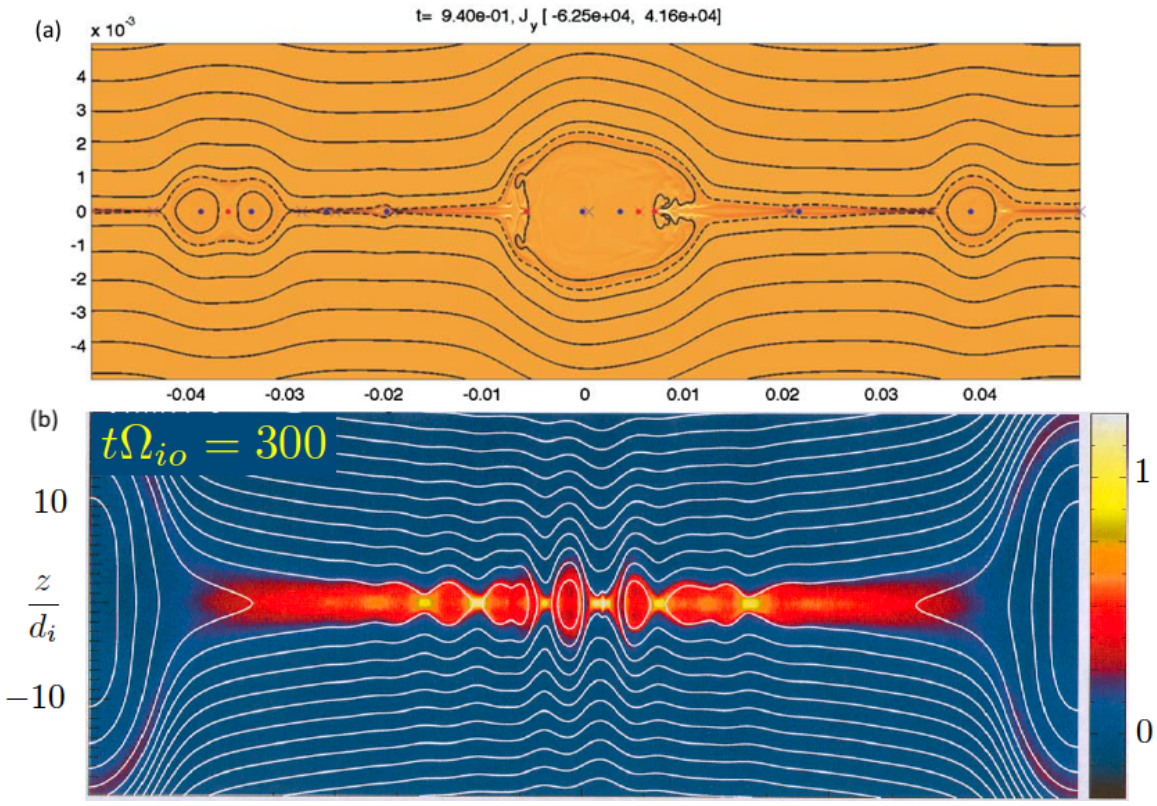

Figure 2.9: Magnetic island formation in (a) a resistive MHD simulation with $S = 3 \times 10^6$ [82], and (b) a full PIC simulation with Fokker-Planck collisions and $S = 5000 - 11700$ [36]. In both simulations, the color signifies out-of-plane current density J_z and contour lines correspond to magnetic field lines. Reprinted with permission from Huang and Bhattacharjee (2010) [82] and Daughton et al. (2009) [36], respectively. (a) ©2009 by the American Institute of Physics. (b) ©2010 by the American Physical Society.

important.

In 2009, Cassak et al. considered how a rescaling of Sweet-Parker reconnection that accounts for the presence of magnetic islands could enhance the reconnection rate by $\sqrt{N}$, where N is the number of islands [22]. This is because the diffusion region (of length L_{SP}) is divided into N regions of length $L' \sim L_{SP}/N$. If each segment can be described by the Sweet-Parker theory of §1.2, then from Eqs. (1.13), (1.14), and (1.15), the thickness of each segment scales as

$$\delta = \sqrt{\frac{\eta c^2 L}{4\pi c_A}} \tag{2.21}$$

meaning that $\delta \sim \delta_{SP}/\sqrt{N}$ where δ_{SP} is the classical Sweet-Parker thickness [36]. Consequently, the global reconnection rate scales as $E \sim \delta/L \sim E_{SP}\sqrt{N}$. Fluid simulations with high Lundquist number S supported this scaling [22]. It was thought that this could give fast reconnection if large current sheets produced many islands. The Loureiro et al. (2007) theory predicted that the number of islands would scale as $N \sim S^{3/8}$ [106], and S is generally very large for the systems in question, but his theory again applies only to the linear regime. A subsequent theory suggested that in the nonlinear regime, plasmoids dominate until the effective Lundquist number for the shortened current sheet between plasmoids becomes small enough to suppress the plasmoid instability $S_{local} \lesssim S_{crit} \approx 10^4$ [82]. According to this theory, the number of plasmoids would scale as $N \sim S/S_{crit}$, predicting a reconnection rate weakly dependent on the Lundquist number: $E \sim S_{crit}^{-1/2} \sim 0.01$ [82, 181].

Despite the recent studies in how islands could boost the effective reconnection rate, Eq. (2.21) presents a significant drawback to these theories. All theories

of fast reconnection by islands requires the inter-plasmoid current sheets to thin out according to Eq. (2.21). However, Daughton et al. in 2009 showed using PIC simulations with a Fokker-Planck collision operator that as the inter-plasmoid current sheet thickness δ approaches the ion inertial length d_i, the transition to kinetic scales triggers Hall physics [36]. The reconnection electric field escalates beyond the runaway limit, forming an electron current layer unstable to the continual formation of new plasmoids. Substituting coronal parameters to Eq. (2.21), even using a global length scale $L \sim 10^9$ cm, the Sweet-Parker current sheet thickness comes to $\delta \sim 1$ m, already smaller than $d_i \sim 4$ m. Therefore, the inter-plasmoid current sheets should transition immediately into Hall physics before they even have a chance to thin out according to Eq. (2.21). This also suggests that secondary island formation probably involves kinetic effects, and that a complete theory of island formation should include kinetic scale physics.

2.3.2 Secondary islands in collisionless guide field reconnection

Accordingly, island formation has also been seen in full particle-in-cell simulations. For example, Drake et al. (2006) showed that component reconnection (including a guide field B_z) becomes bursty [46]. In a collisionless plasma, the nature of component reconnection is quite different from the anti-parallel Hall reconnection discussed in §1.3. The key difference is that the reconnection electric field E_z now has a component parallel to the magnetic field [42]. The resulting parallel acceleration of electrons produces a strong J_{ez}, but the in-plane components of

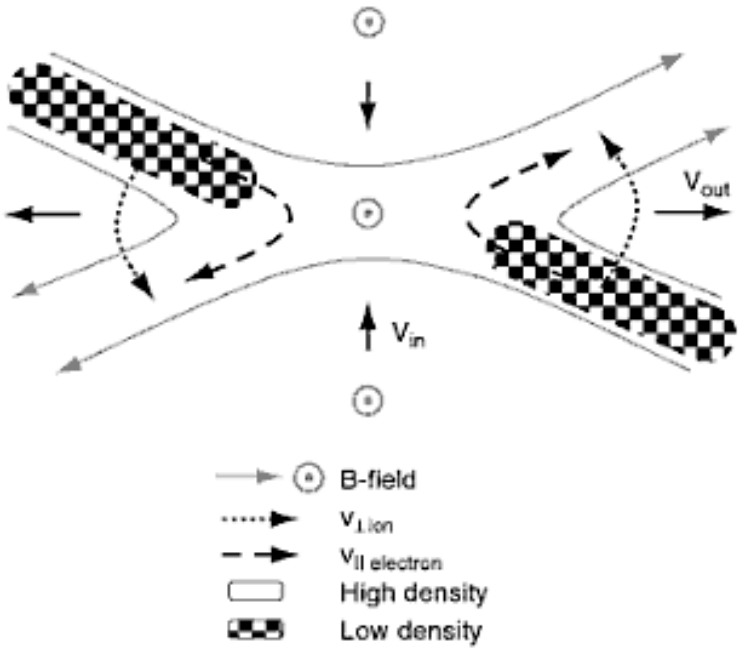

Figure 2.10: Schematic of quadrupolar density perturbation in reconnection with a guide field showing the density asymmetry across the dissipation region. Reprinted with permission from Drake and Shay (2007) [42]. ©2007 by Cambridge University Press.

the $E_{\|}$ acceleration results in electron streaming along the newly reconnected field lines. The electron flow across the current layer results in a density depletion on one side of the current sheet and a density enhancement on the other, as shown in Fig. 2.10.

An alternative way to describe Fig. 2.10 is to consider that the guide field B_z is now complemented by the quadrupolar Hall magnetic field. If even a small Hall magnetic field $\tilde{B}_z$ perturbs the guide field, the change in magnetic pressure

$$\Delta p_m = \frac{(B_z + \tilde{B}_z)^2}{8\pi} - \frac{B_z^2}{8\pi} \approx \frac{B_z \tilde{B}_z}{4\pi} \tag{2.22}$$

must be counteracted by a corresponding change in the plasma density $\tilde{n}$ given by

$$\tilde{n}T = -\frac{B_z \tilde{B}_z}{4\pi} \tag{2.23}$$

in order to maintain pressure balance. (Note that in the absence of a guide field, the change in magnetic pressure is second order in $\tilde{B}_z$, and so this density asymmetry does not occur.) Thus, the regions where the guide field is enhanced by the quadrupolar Hall magnetic field are accompanied by a density depletion, whereas the regions where the guide field and quadrupolar Hall magnetic field are of opposite sign show a density enhancement [20].

The configuration in Fig. 2.10 is characteristic of the kinetic Alfvén wave, which replaces the whistler wave described in §1.3 as the mediator of fast reconnection. A consequence of this is that the separatrix with the enhanced density (the upper-right and lower-left of Fig. 2.10) carries most of the current, and so the electron current sheet with $J_{ez} = -n_e e v_{ez}$ becomes tilted along the density enhancement. This twist in the current sheet has been observed in simulations of component reconnection [176, 132, 133, 44], such as in Fig. 2.11. Furthermore, simulations have shown that the electron current layer becomes very narrow (width less than d_e) [77] and long in the vicinity of the x-line, ripe for the formation of secondary islands seen in Drake et al. (2006) [46].

Other kinetic simulations have seen secondary island formation without a guide field as well [35, 63, 90, 93]. Fig. 2.9(b), for example, shows islands generated in a full PIC simulation with Fokker-Planck collisions with Lundquist number ranging from $S_0 = 5000$ (based on the initial resistivity) to $S_{max} = 11700$ (due to electron

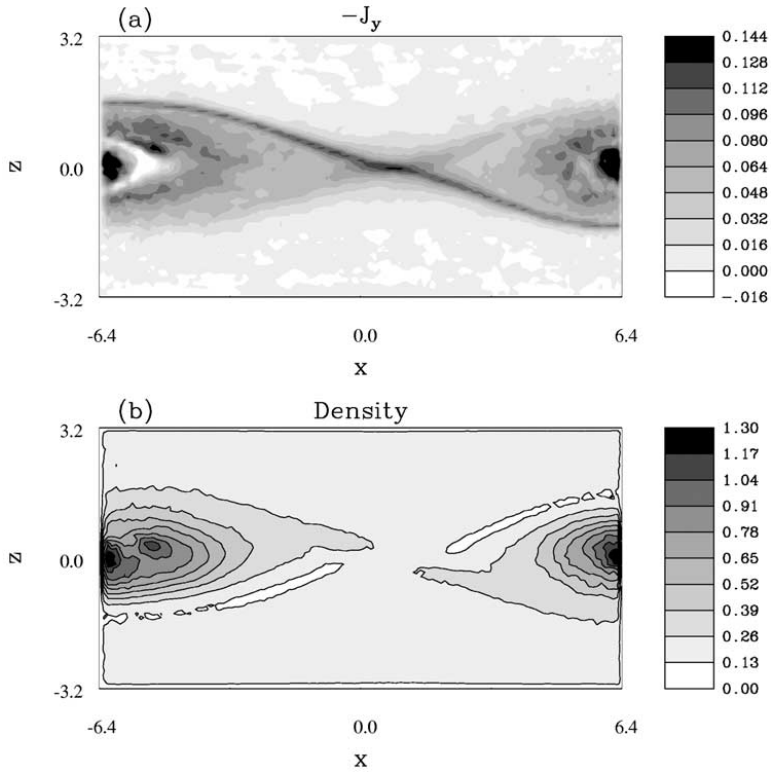

Figure 2.11: Contours of (a) the out-of-plane current density $-J_y$ (J_z in the coordinates used here) and (b) the ion density n_i for a simulation of component reconnection. Reprinted with permission from Pritchett and Coronoiti (2004) [133]. ©2004 by the American Geophysical Union.

heating in the current layer) [36]. Recently, 3-D PIC simulations exploring the electron physics of turbulent reconnection show that 3-D flux ropes develop from the tearing mode [37].

2.3.3 Particle energization by the Fermi mechanism

An important application of magnetic islands is the role they could play in particle acceleration. In 2006, Drake et al. suggested that electrons could gain energy by a classic Fermi mechanism within contracting magnetic islands [46]. The process is analogous to a ball bouncing between two converging walls, gaining energy with each reflection. An elongated magnetic island will contract until its magnetic tension is released, with the ends closing in typically at the Alfvén speed c_A. Consequently, super-Alfvénic particles within the island would potentially have the chance to traverse between both ends of the island multiple times. This process is illustrated for a test particle in a PIC simulation in Fig. 2.12(a). Fig. 2.12(b) shows how the particle gains parallel energy $\mathcal{E}_\parallel = mv_\parallel^2/2$ with each bounce. When the island finally crosses the separatrix, the parallel energy is scattered into perpendicular energy $\mathcal{E}_\perp$ as in Fig. 2.12(c). If the system consists of many volume-filling islands as sketched in Fig. 2.12(d), scattered particles can repeat this process indefinitely and attain very high energies.[1] The rate of energy gain

$$\frac{d\mathcal{E}_\parallel}{dt} = -2\mathcal{E}_\parallel \frac{v_x B_x^2}{\delta_x B^2} \tag{2.24}$$

[1]Such a picture is possible in 3-D, for which resonance surfaces of the tearing instability (those where $\mathbf{k}\cdot\mathbf{B} = 0$) are not constrained to the $y = 0$ symmetry line.

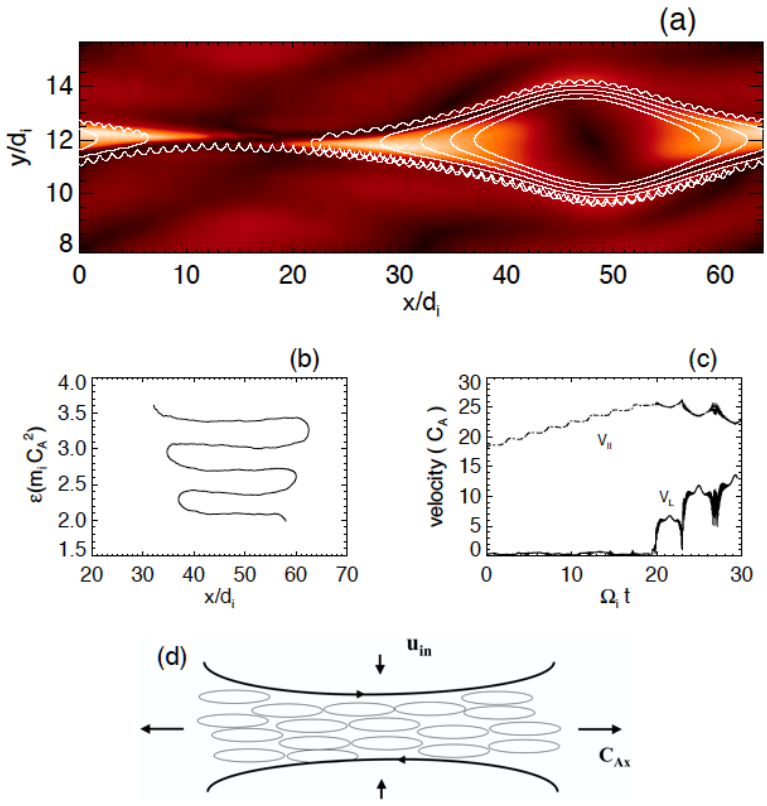

Figure 2.12: Fermi acceleration of a test particle within a PIC simulation of a contracting magnetic island. (a) The test particle trajectory; the electromagnetic fields are frozen, but are still present, so the test particle still feels the island "contracting" with each reflection. (b) The particle's kinetic energy $\mathcal{E}$ as it bounces in x. (c) The particle's parallel and perpendicular velocities $v_{\parallel}$ and $v_{\perp}$ in time. (d) A sketch of reconnection by many volume-filling islands. Reprinted with permission from Drake et al. (2006) [45]. ©2006 by Macmillan Publishers Limited.

is independent of mass, so this could be an efficient heating mechanism for both ions and electrons.

If volume-filling islands dominate coronal current sheets as suggested in §2.2.3, the Fermi mechanism could be a factor in electron acceleration. In the outer heliosphere, where ACRs were unexpectedly observed well beyond the termination shock by Voyager 1 and Voyager 2 [170, 171], Opher et al. have suggested that sectored magnetic fields could undergo reconnection, generate islands, and accelerate particles into ACRs [122, 41]. Other mechanisms for particle energization within magnetic islands have been proposed as well. One theory asserts that electrons can be accelerated at a merging x-line, the site where two magnetic islands coalesce with one another [120]. The energetic electrons associated with plasmoids in the magnetotail discussed in §2.2.2 also support particle energization in islands [29]. Power law spectra of energetic particles in the magnetotail observed by Wind are consistent with Fermi acceleration [118], although this remains an open question [55].

2.4 The dynamics of many magnetic islands

It is now apparent that a complete understanding of current sheets in the magnetosphere, solar corona, and other relevant space and astrophysical plasmas requires a proper understanding of magnetic islands. As computational capabilities increase, we have begun to see that secondary islands form at kinetic scales [46, 35, 63, 90, 93, 36]. Observations of islands within an extended electron current sheet in the Hall region also suggest that kinetic physics are key to their formation

[51, 28, 178]. Yet in the magnetopause, the magnetotail, and in the solar corona, what we most frequently observe are macroscale objects. Magnetic islands on the magnetopause can be as large as several R_E [137, 146, 61] or even larger in the magnetotail [56, 166]. Likewise, the downflowing coronal voids in Fig. 2.8 are measured in megameters (d_i in the corona is on the order of meters) [156]. The large blob-like structures seen on post-CME current sheets are visible on SOHO/LASCO C3, a white light coronograph that images from $3.7 - 32R_\odot$. An important question then is: How do magnetic islands grow from small kinetic scales into macroscale objects?

To answer this question, we need to understand the dynamics of magnetic islands. To this end, we observe the secondary islands generated by PIC simulations of guide field reconnection performed by Drake et al. [46]. The simulation is initialized with a perturbation that allows for just a single x-line on each current sheet. In Fig. 2.13(a), we see an elongated electron current layer form. The current layer becomes unstable to the formation of secondary islands in Fig. 2.13(b). As reconnection proceeds, the islands gain flux and grow larger in Fig. 2.13(c). By the end of the simulation in Fig. 2.13(d), the islands have convected away from the original x-line and have started to merge with the primary island. We also see a new secondary island starting to form in the lower current sheet. The dynamics of the magnetic islands observed in this simulation include their formation, growth, convection, and coalescence. Although these dynamics of magnetic islands have been investigated in preexisting literature (for example, formation [64, 46, 35, 106], growth [76, 5, 86], convection [34, 12, 159], and coalescence [134, 39]), in this thesis we begin to study these processes together in a single model.

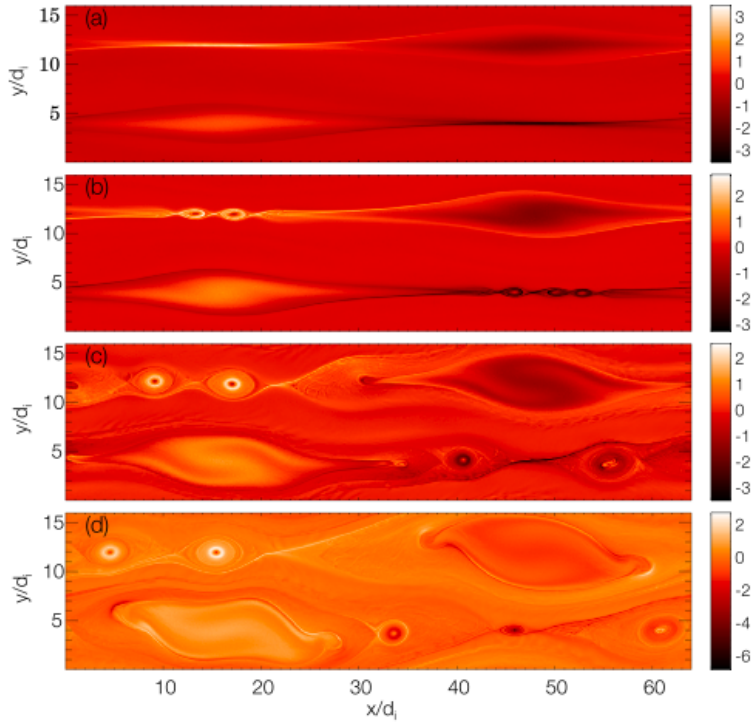

Figure 2.13: The out-of-plane electron current density J_{ez} in a PIC simulation of reconnection with a guide field $B_g = B_{x0}$, shown at times (a) $t = 11\Omega_{ci}^{-1}$, (b) $t = 14\Omega_{ci}^{-1}$, (c) $t = 20\Omega_{ci}^{-1}$, and (d) $t = 24\Omega_{ci}^{-1}$. Reprinted with permission from Drake et al. (2006) [46]. ©2006 by the American Geophysical Union.

However, the dynamics of islands in very large current layers are not yet well understood. On the one hand, even the largest particle-in-cell (PIC) simulations come nowhere near the system sizes of these current layers. In the magnetopause $L \sim 4000d_i$, $L \sim 6000d_i$ for the magnetotail plasma sheet, and $L \sim 10^4$ km $\sim 10^7 d_i$ in the corona. On the other hand, $L = 64d_i$ in Fig. 2.13 [46], and even the largest, most recent 2-D PIC simulations, only reach $L \lesssim 1000d_i$ [36]. Although global fluid simulations can encompass these large scales[135, 38], they fail to capture the small scale dynamics of reconnection within the dissipation region. This presents a challenge because it is extraordinarily difficult to perform sufficiently large scale simulations of many magnetic islands while still capturing the separation of scales and kinetic effects.

In light of these limitations, this thesis will consider a novel statistical method for treating magnetic islands in large current layers. We shall define a distribution function that describes islands in the whole current layer and develop an evolution equation for that distribution based on the dynamics observed in Fig. 2.13. We then present steady state solutions, which show how the merger of smaller islands drives the growth of large islands. To validate this model, we shall perform large Hall MHD simulations of many islands and compare the resulting distributions of islands to the predictions of our model. We shall also explore the formation of secondary islands in PIC simulations similar to those shown in Fig. 2.13 and investigate how they are formed at small scales. Lastly, we continue the validation of our model with a large database of FTEs observed by the Cluster spacecraft.

Chapter 3

Formulation of a statistical model

In order to be able to describe systems as large as the magnetopause, the magnetotail, or especially coronal current sheets, it is beneficial to try to reduce the number of degrees of freedom. To make an analogy with thermodynamics, it can be quite cumbersome to try to follow the state of every individual particle; it is much easier (and more illuminating) to deal with distribution functions of particles or even macro-state parameters such as temperature and density. In this case, it is very difficult to achieve through simulations the separation of scales necessary to understand island dynamics. Consequently, we might consider a distribution of islands, characterized by a few key but simple parameters, that describes islands over the whole current sheet of length L.

3.1 Defining the statistical distribution function $f(\psi, A)$

Our choice of parameters derives from the relatively simple picture of a magnetic island in Fig. 2.3. We choose to describe this island by the in-plane magnetic flux it contains ψ and the area it encloses A. To be more precise, both of these quantities can be defined in terms of the flux function Ψ such that $B = \hat{\mathbf{z}} \times \nabla\Psi$.[1]

[1] In Ch. 2, the flux function was denoted by ψ. Henceforth, we shall use Ψ for the flux function in order to distinguish it from the island parameter ψ.

The in-plane magnetic flux of the island is just the difference in Ψ from the x-line to the o-line:

$$\psi = \left| \int_{\text{x-line}}^{\text{o-line}} dx B_y \right| = |\Psi_X - \Psi_O|. \tag{3.1}$$

The area A is simply the area enclosed by the separatrix (the emboldened field line in Fig. 2.3). In reality, even the 2-D picture is never quite as simple as Fig. 2.3, because the separatrices for the two x-lines in general might not coincide. A more precise definition in this more general case is discussed for our Hall MHD simulations in §5.2, but the more relevant point is that regardless of the particular definition, both ψ and A are easily quantifiable in simulations of magnetic islands such as those in Fig. 2.9.

How do these parameters translate to the case of 3-D flux tubes? The area A is of course simply the cross-sectional area of a 2-D cut through the flux tube. With regards to the flux ψ, it is worth differentiating between the magnetic flux through such a cross-section $\int d\mathbf{A} \cdot \mathbf{B}$ (or in Fig. 2.3, $\int dA B_z$) and the in-plane magnetic flux we use here. The former definition of flux is used in some contexts, but for our purposes, the in-plane flux is the more fundamental parameter. Whereas the magnetic flux through a cross-section of the flux tube is related to the guide field, the in-plane magnetic flux is a better indicator of the amount of *reconnected* flux.

To a large extent, ψ and A are sufficient to characterize the state of an island because many of the important characteristics of the island can be described in terms of these two quantities. A simple case is the characteristic scale-size for the

island, which can be defined as

$$r = \sqrt{\frac{A}{\pi}}. \tag{3.2}$$

(We will eventually use r interchangeably with A as our dependent variable. The island need not be circular, however; r merely acts as a proxy for the more physical quantity A.) We assume that the plasma is basically incompressible, so that the total mass of plasma in the island is basically nA. A typical in-plane magnetic field strength within the island is given by

$$B = \psi/r = \psi\sqrt{\pi/A}. \tag{3.3}$$

Lastly, we can calculate the magnetic energy within the island as the magnetic energy density multiplied by the island size

$$W = (B^2/8\pi)A \sim \psi^2/8. \tag{3.4}$$

Thus, we confidently model the islands using a distribution function f in terms of the island's flux ψ and area A. Defined in this manner, $dN = f(\psi, A)d\psi dA$ signifies the number of magnetic islands in the entire system that have flux in the range $[\psi, \psi + d\psi]$ and area in $[A, A + dA]$. The total number of islands is then

$$N = \int_0^\infty d\psi \int_0^\infty dA f(\psi, A). \tag{3.5}$$

3.2 Rules governing island behavior

We can expand the distribution function to include a time-dependence. Now, $f(\psi, A, t)$ evolves in time in the phase space of (ψ, A). We now establish rules for the behavior of magnetic islands, based on what is observed in simulations such as

in Fig. 2.13, and formalize mathematically how these rules affect the distribution. Ultimately, our goal is to write down an equation for how $f(\psi, A, t)$ evolves in time. In §2.4, we described four dynamical process that we would like to describe in our model: island creation, growth, convection, and coalescence. We now consider those four processes here.

3.2.1 Creation, growth, and convection of islands

Islands first form at kinetic scales between the electron d_e and ion d_i skin depths in the current layers near x-lines [46, 35, 93, 36, 51, 28, 178]. The evolution equation therefore should include a source term $S(\psi, A)$ at this scale. The most important feature of the source term is its magnitude

$$S_N = \int_0^\infty d\psi \int_0^\infty dA S(\psi, A), \tag{3.6}$$

which describes the total number of islands generated at d_e to d_i scales per unit time. If there is a sufficient separation of scales between kinetic and global scales (i.e., $L \gg d_i$), S_N is in fact the only feature of the source term of global importance. Although our choice of $S(\psi, A)$ treats islands down to the d_e scale, the model remains valid even if the classical tearing mode without kinetic effects acts as the source term. Furthermore, although we will use a log-normal distribution in ψ and A, the particular shape of $S(\psi, A)$ gets washed out by the time the distribution reaches global scales.

The model must also account for the growth of magnetic islands due to reconnection. Magnetotail observations reveal that plasmoids grow as they flow tailward

[76, 5, 86]. PIC simulations have shown that once reconnection reaches a nonlinear stage, the normalized reconnection rate plateaus at roughly $\varepsilon \approx 0.1$ [154]. Given this quasi-steady reconnection rate and an asymptotic reconnection magnetic field of B_0, the magnetic flux of an island increases at the rate $\dot{\psi} = v_{in} B_x = \varepsilon c_A B_0$. Likewise, if the plasma is largely incompressible, the island's characteristic radius r increases at a constant rate $\dot{r} = \varepsilon c_A$, and so the area increases at the rate $\dot{A} = 2\pi r v_{in} = 2\varepsilon c_A \sqrt{\pi A}$.

We wish to model the convection of islands along the current sheet at the Alfvén speed [159]. However, $f(\psi, A)$ describes the distribution islands over the whole current sheet of length L without regard for their positions in the current sheet. Ultimately though, those islands convect outwards and leave the system. For example, FTEs generated at the subsolar magnetopause convect poleward, eventually colliding with the cusps, where they disintegrate due to secondary reconnection [121]. In the magnetotail, islands meet their end at the Earth or in the distant tail. The downflowing coronal voids seen by Sheeley et al. are probably flux tubes that have convected down from a reconnection site higher up [156]. Therefore, as islands convect outwards at the Alfvén speed, a sink term models the convection of islands out of the system at the rate c_A/L.

3.2.2 Properties of island coalescence

We now describe the rules for island coalescence: the merger of two islands yields an island with an area A equal to the sum of the two initial areas and a flux ψ equal to the higher of the two initial fluxes. The area adds assuming incompress-

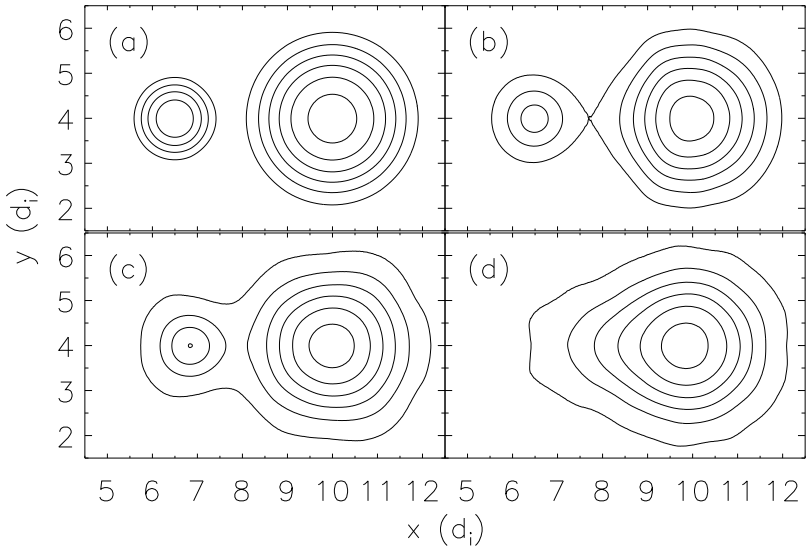

Figure 3.1: The results of a PIC simulation of island merger, showing the magnetic field lines at (a) $t = 0\Omega_{ci}^{-1}$, (b) $t = 0.3\Omega_{ci}^{-1}$, (c) $t = 4.0\Omega_{ci}^{-1}$, and (d) $t = 8.0\Omega_{ci}^{-1}$, where Ω_{ci} is the ion cyclotron frequency. The smaller island initially has 75% of the flux and 25% of the area of the larger island.

ibility. The flux does not add because magnetic reconnection does not increase or decrease magnetic flux but simply changes its connectivity. Thus, field lines from the island with more flux reconnect with those from the island with less flux until all of the latter's flux is depleted. The simplicity of these rules reflect our choice of ψ and A as the variables defining our phase space. Fig. 3.1 shows results from a PIC simulation that demonstrates this in the simple case of two isolated flux bundles. The simulation was performed using the code P3D [187].[2] Magnetic field contours are shown at various times during the merging process, with the outermost field line

[2]The computational methodology for P3D will be discussed in greater detail in §6.1.

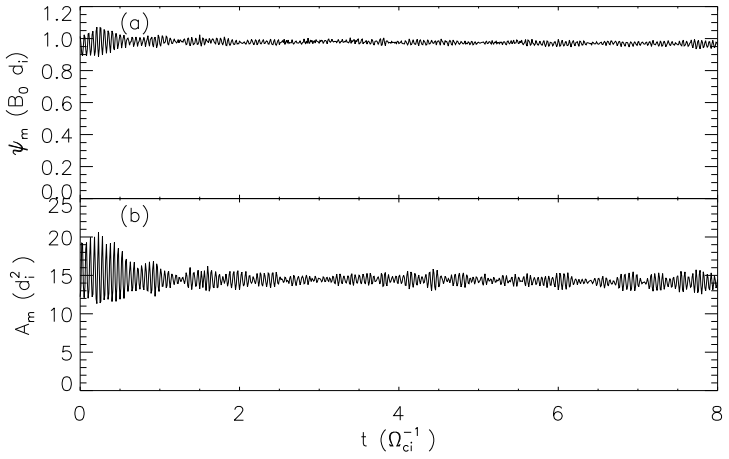

Figure 3.2: The maximum flux ψ_m and combined area A_m of the coalescing islands in time t from the start of the simulation. The variations in ψ and A have respective standard deviations of 2% and 7% from the mean.

representing the boundary of the island for the purposes of computing area. Initially, while the two islands are separate, we define the maximum flux $\psi_m = \max\{\psi_1, \psi_2\}$ and the combined area $A_m = A_1 + A_2$. At some point, the merging x-line and the o-line of the smaller island meet, and the merging process is essentially complete, after which we simply define ψ_m and A_m as the flux and area of the resultant merged island. Fig. 3.2 shows that both ψ_m and A_m remained nearly constant throughout the simulation.

These merging rules reveal why the merging process is energetically favorable: the dissipation of magnetic energy in the reconnection process. We can write the magnetic energy in an island as according to Eq. (3.4). Before the merger the energy is given by $W_i \propto \psi_1^2 + \psi_2^2$, and after the merger the energy (supposing $\psi_1 \leq \psi_2$

without loss of generality) is $W_f \propto \psi_2^2 < W_i$.

3.3 An equation for f

We now derive an equation for the island distribution f. The equation will parallel the collisional Boltzmann equation [15]

$$\frac{\partial f}{\partial t} + \frac{\mathbf{p}}{m} \cdot \nabla f + \mathbf{F} \cdot \frac{\partial f}{\partial \mathbf{p}} = \left.\frac{\partial f}{\partial t}\right|_{\text{coll}} \tag{3.7}$$

with island growth by quasi-steady reconnection playing the roles of $\mathbf{p}$ and $\mathbf{F}$ and island coalescence acting like a collision operator. As such, the growth terms will have the form $\dot{\psi}\partial f/\partial\psi$ and $\dot{A}\partial f/\partial A$.

3.3.1 Mathematical formalism for the merging rules

Modeling the merging terms will prove to be more complicated. As islands convect through the current sheet, we hypothesize that the probability of two islands merging with one another over some time interval Δt is roughly $v\Delta t/L$, where v is some merging velocity which is characteristically the Alfvén speed in the MHD limit. More generally, for islands larger than d_i, we want v to resemble the predicted outflow speed for asymmetric reconnection, that is, the hybrid Alfvén velocity $v^2 \approx B_1 B_2/4\pi n m_i$ where constant density n is assumed [21, 175]. For smaller islands, down to the electron skin depth d_e, $v^2 \approx \psi_1\psi_2 d_i^2/4\pi n m_i r_1^2 r_2^2 \approx k^2 d_i^2 c_A^2$ in agreement with the dispersion relation $\omega^2 = k^4 d_e^4 \Omega_e^2 = k^4 d_e^2 c_{Ae}^2 = k^4 d_i^2 c_A^2$ of the whistler dynamics that dominate this regime [43]. Lastly, $v \to 0$ as $r \to 0$ would be desirable. We therefore write an *ad hoc* merging velocity of two islands with fluxes

ψ_1, ψ_2 and areas A_1, A_2 as

$$v^2(\psi_1, A_1, \psi_2, A_2) = \frac{\psi_1 \psi_2 r_1 r_2 (r_1^2 + d_i^2)^{1/2} (r_2^2 + d_i^2)^{1/2}}{4\pi n m_i (r_1^2 + d_e^2)^{3/2} (r_2^2 + d_e^2)^{3/2}} \tag{3.8}$$

where the dependence on A_1 and A_2 is implicit in r_1 and r_2 according to Eq. (3.2). This expression is consistent with the prescribed limits for the cases $r \gg d_i$, $d_e \ll r \ll d_i$, and $r \ll d_e$, respectively.

Now we consider the number of islands $\Delta N|_{mrg+}(\psi, A)$ formed by merging. A merged island with flux ψ arises from an island of flux ψ that has merged with another island with flux $\psi' \leq \psi$. Likewise, an island with area A must come from an island with $A' < A$ that has merged with an island of area $A - A'$. The probability of those two islands merging within a time Δt is given by $v(\psi, A', \psi', A - A')\Delta t/L$, so

$$\Delta N|_{mrg+} = \int_0^A dA' f(\psi, A') \int_0^\psi d\psi' \frac{v\Delta t}{L} f(\psi', A - A') \Delta\psi \Delta A. \tag{3.9}$$

A similar analysis yields the number of islands lost through merging $\Delta N|_{mrg-}(\psi, A)$. Such an island is lost if it merges with any island of finite flux ψ' and area A'. As before, the probability of merger depends on $v(\psi, A, \psi', A')\Delta t/L$, and so

$$\Delta N|_{mrg-} = -\int_0^\infty dA' \int_0^\infty d\psi' \frac{v\Delta t}{L} f(\psi', A') f(\psi, A) \Delta\psi \Delta A. \tag{3.10}$$

The proposed rate of merging is only an approximation, however, so we will introduce a dimensionless coefficient to the merging terms K_{mrg}. A value of $K_{mrg} = 1$ corresponds most similarly to a current sheet in which the islands are like point-particles and the current sheet is a string-of-beads. Of course in reality, islands occupy a finite volume, so $K_{mrg} > 1$ is likely. In Ch. 5, we will fit the parameter K_{mrg} to simulation results.

3.3.2 The evolution equation

The change in f due to merging is simply $\Delta N|_{mrg}/\Delta\psi\Delta A\Delta t$, with $\Delta N|_{mrg}$ given by adding Eqs. (3.9)-(3.10) multiplied by K_{mrg}. Combining this expression in differential form with the change in f due to quasi-steady reconnection, the source term $S(\psi, A)$, and the convective loss term proportional to c_A/L, we get our evolution equation:

$$\begin{aligned}\frac{\partial f}{\partial t} + \frac{\partial}{\partial \psi}\left(\dot{\psi} f\right) + \frac{\partial}{\partial A}\left(\dot{A} f\right) &= S(\psi, A) - \frac{c_A}{L} f \\ &+ \frac{K_{mrg}}{L}\int_0^A dA' f(\psi, A') \int_0^\psi d\psi' v(\psi, A', \psi', A - A') f(\psi', A - A') \\ &- \frac{K_{mrg}}{L} f(\psi, A) \int_0^\infty dA' \int_0^\infty d\psi' v(\psi, A, \psi', A') f(\psi', A'). \end{aligned} \tag{3.11}$$

On the left-hand side, the time-derivative of f results from the growth in flux $\dot{\psi}$ and area $\dot{A}$ due to reconnection. On the right-hand side, we have the source term $S(\psi, A)$ responsible for island creation, a sink term proportional to c_A/L representing island convection out of the system, and the merging terms. Consistent with the merging rules, the merging terms in Eq. (3.11) preserve total area. (This is demonstrated in Appendix B.)

3.3.3 A non-dimensional form

Although Eq. (3.11) appears to contain several parameters (the current sheet length L, the reconnection rate ε, the merging coefficient K_{mrg}, and the source term strength S_N), in reality it only has one free parameter. By normalizing time to $t/t^* = L/c_A$, island flux to $\psi/\psi^* = \varepsilon B_0 L$, island area to $A/A^* = (\varepsilon L)^2$, the merging

velocity to $v/v^* = c_A$, and the distribution function to $f/f^* = 1/K_{mrg}(\varepsilon L)^3 B_0$, then Eq. (3.11) reduces to a non-dimensional evolution equation

$$\begin{aligned}\frac{\partial f^*}{\partial t^*} + \frac{\partial}{\partial \psi^*}\left(\dot{\psi}^* f^*\right) + \frac{\partial}{\partial A^*}\left(\dot{A}^* f^*\right) &= \frac{K_{mrg}L}{c_A} S_N S^*(\psi^*, A^*) - f^* \\ &+ \int_0^{A^*} dA^{*\prime} f^*(\psi^*, A^{*\prime}) \int_0^{\psi^*} d\psi^{*\prime} v^*(\psi^*, A^{*\prime}, \psi^{*\prime}, A^* - A^{*\prime}) f^*(\psi^{*\prime}, A^* - A^{*\prime}) \\ &- f^*(\psi^*, A^*) \int_0^{\infty} dA^{*\prime} \int_0^{\infty} d\psi^{*\prime} v^*(\psi^*, A^*, \psi^{*\prime}, A^{*\prime}) f^*(\psi^{*\prime}, A^{*\prime}) \end{aligned} \tag{3.12}$$

where S^* is a non-dimensional source term of unit magnitude: $\int_0^\infty d\psi^* \int_0^\infty dA^* S^* = 1$. As suggested in §3.1, so long as there is a sufficient separation of scales – mathematically, if S^* is non-zero only in a localized region of $\psi^* \ll 1$ and $A^* \ll 1$ – the particular form of S^* (e.g., delta function, Gaussian, log-normal etc.) does not affect the global solution f^*. It is now apparent that the sole free parameter in Eq. (3.12) is the coefficient of S^*, which we define as the normalized source amplitude

$$S_N^* = \frac{K_{mrg}L}{c_A} S_N. \tag{3.13}$$

The significance of this statement is that we can effectively model any system solely by varying S_N. For example, we might set $L = 4000 d_i$ in order to model the magnetopause, but if we want to model a coronal current sheet of length $L = 10^6 d_i$ with otherwise the same parameters (i.e., the same reconnection rate, etc.), the solution obtained by increasing S_N by three orders of magnitude will suffice.

Chapter 4

Steady state solutions

We seek steady state solutions to Eq. (3.11). We expect such a steady state solution to occur when the island source $S(\psi, A)$ balances the sink $-c_A/Lf$. Such a solution could then be used to predict the distribution of islands in long current sheets such as the magnetopause, the magnetotail, coronal current sheets, and various other space and astrophysical systems. This is not to say that the current sheet is itself at a steady state. Rather, we suppose that the system after some time has reached a point where the distribution of islands is representative of the distribution at any other time, a sort of statistical steady state. The distribution of islands at the steady state shall be denoted $f_\infty(\psi, A)$.

4.1 The no-merging solution

The complexity of the merging terms make Eq. (3.11) impossible to solve analytically. We therefore first consider the case where the merging terms are negligible. This is valid if there are few islands in the layer, e.g., if $S(\psi, A)$ is small. For simplicity, we now change variables from the area A to the characteristic radius r, with $A = \pi r^2$, and consider the statistical distribution function $F(\psi, r)$. Island number must be conserved under this transformation, so $dN = f(\psi, A)d\psi dA = F(\psi, r)d\psi dr$,

and

$$F(\psi, r) = f(\psi, A)\frac{dA}{dr} = 2\pi r f(\psi, \pi r^2). \tag{4.1}$$

Substituting $f = F/2\pi r$, $\dot{A} = 2\pi r\dot{r}$, and $\partial/\partial A = (2\pi r)^{-1}\partial/\partial r$ into Eq. (3.11), the evolution equation without merging becomes

$$\frac{\partial F}{\partial t} + \frac{\partial}{\partial \psi}\left(\dot{\psi}F\right) + \frac{\partial}{\partial r}\left(\dot{r}F\right) = S(\psi, r) - \frac{c_A}{L}F \tag{4.2}$$

where $\dot{r} = \varepsilon c_A$. The form of $\dot{r}$ reveals why we have transformed from A to r. Whereas $\dot{A} \propto \sqrt{A}$, for our assumption of quasi-steady reconnection both $\dot{\psi}$ and $\dot{r}$ are constants.

With a delta function source

$$S(\psi, r) = S_N \delta(\psi - \psi')\delta(r - r') \tag{4.3}$$

the steady state solution F_G is given by the Green's function

$$F_G(\psi, r, \psi', r') = \frac{S_N}{\varepsilon c_A}\exp\left(-\frac{r - r'}{\varepsilon L}\right)H(r - r')\delta\left((\psi - \psi') - B_0(r - r')\right) \tag{4.4}$$

where $H(r)$ is the Heaviside function, which simply ensures that islands are no smaller than those generated by the delta function source. (No mechanism exists for making islands smaller.) The delta function in $\delta((\psi - \psi') - B_0(r - r'))$ ensures that all islands in this solution have a characteristic in-plane magnetic field strength B_0, equal to the ambient magnetic field (assuming $\psi' = B_0 r'$). The solution in $\psi - r$ phase space is a decaying exponential along the line $\psi = B_0 r$, starting at $\psi = \psi'$ and $r = r'$.

A key feature of Eq. (4.4) is the characteristic island size $\hat{r} = \varepsilon L$ in the exponential. This length scale arises from balancing the rate of island growth $\dot{r} =$

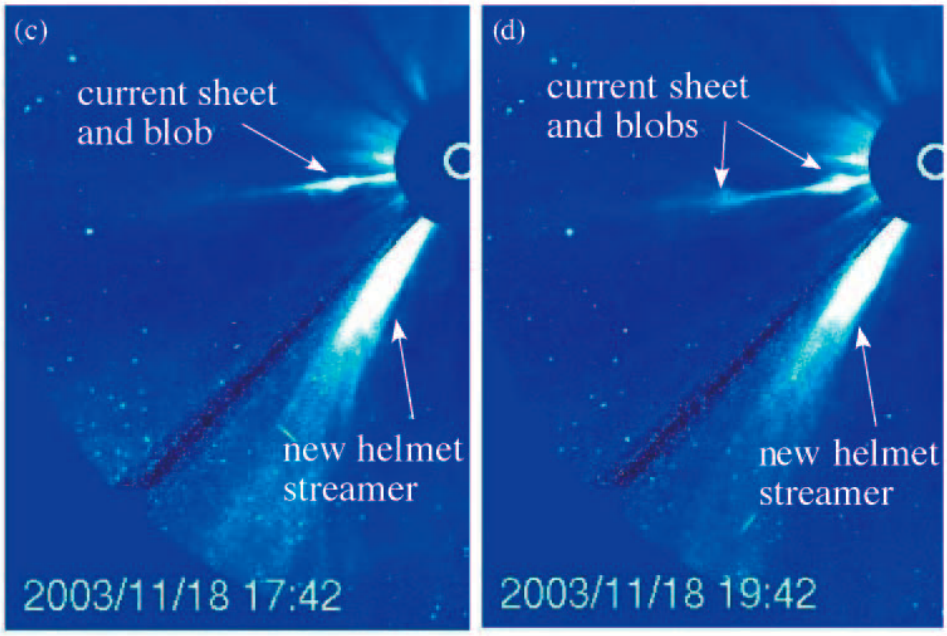

Figure 4.1: A November 18, 2003 CME current sheet and helmet streamer imaged by the white light coronagraph LASCO C3 on the SOHO spacecraft. Times shown are in UT. Reprinted with permission from Lin et al. (2005) [100]. ©1981 by the Institute of Physics.

εc_A with a system transit time of L/c_A. For example, with a reconnection rate of $\varepsilon \sim 0.1$ on the magnetopause where $L \sim 30\,R_E$, this simple model predicts islands of size $\sim 3\,R_E$. A survey of flux transfer events along the magnetopause [137, 146] determined that typical scale sizes are $0.5\,R_E \times 2\,R_E$, for which $r \approx 1\,R_E$. Such island sizes are also consistent with those seen in direct observations of current sheets formed by CMEs. Fig. 4.1 shows what is believed to be a post-CME current sheet, featuring macroscale "blobs," which could be interpreted as magnetic islands that have grown to nearly one-tenth of the current sheet length [100].

4.2 Numerical solution with merging and the $\psi - r$ asymmetry

If the merging terms are kept, the resulting integro-differential equation must be solved computationally. As discussed in §3.3.3, S_N^* is the only free parameter in Eq. (3.12), so any parameter regime can be explored by solely modifying S_N^*. As such, we choose $L = 4000d_i$ (the size of the magnetopause), $\varepsilon = 0.1$ (corresponding to fast reconnection [154]), $K_{mrg} = 1$, and vary S_N over three orders of magnitude from $S_N = 0.01\Omega_{ci}$ to $S_N = 10\Omega_{ci}$.

Fig. 4.2 shows the evolution of the distribution function in (ψ, r) phase space for $S_N = 1\Omega_{ci}$, or $S_N^* = 4000$. The source function $S(\psi, r)$ generates islands at the d_e to d_i scales, in the far bottom left corner. Growth due to quasi-steady reconnection increases both ψ and r at a constant rate, as discussed in §4.1. In (ψ, r) phase space, this gives growth along a line of slope $\dot{\psi}/\dot{r} = B_0$. Therefore, the no-merging solution described by Eq. (4.4) would remain localized along the line $\psi = B_0 r$, shown as the dashed diagonal lines in Fig. 4.2. On the other hand, the merging terms break this symmetry. Island coalescence increases area but not flux, so the distribution in Fig. 4.2 curves away from the diagonal $\psi = B_0 r$. The $\psi - r$ asymmetry introduced by the merging terms is an important aspect of this model and will receive much attention for the duration of this thesis.

The integration of Eq. (3.11) eventually reaches the steady state island distribution, $F_\infty(\psi, r)$, as seen by the nearly identical Fig. 4.2(c)-(d). The steady state distribution is shown for four values of S_N in Fig. 4.3. Note that the $\psi - r$ asymmetry due to merging appears in various degrees among the four solutions. In the $S_N^* = 40$

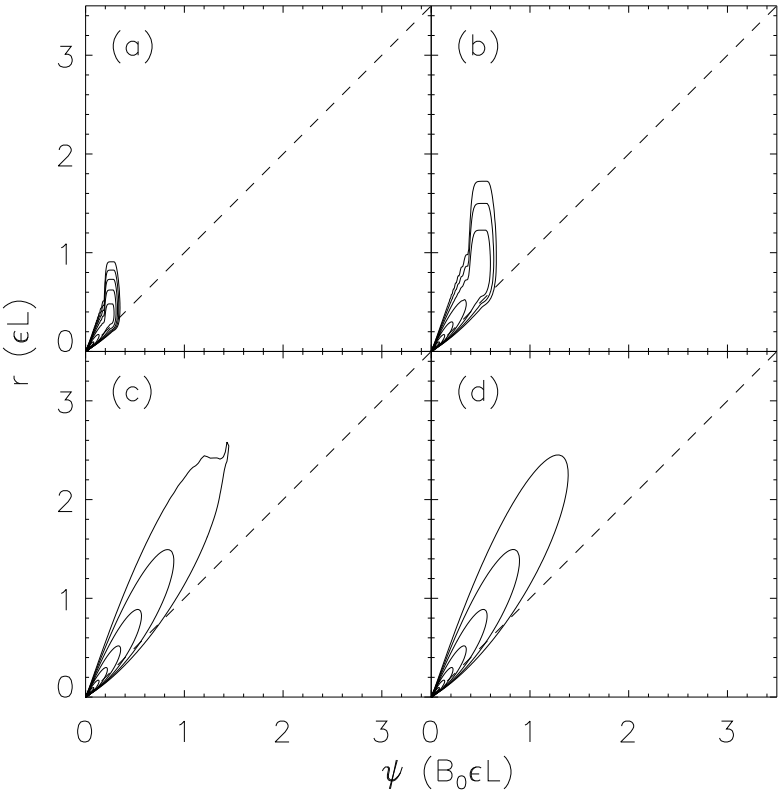

Figure 4.2: The time evolution of $F(\psi, r)$ with $S_N^* = 4000$ at (a) $t = 1000\Omega_{ci}^{-1}$, (b) $t = 2000\Omega_{ci}^{-1}$, (c) $t = 7000\Omega_{ci}^{-1}$, and (d) $t = 17000\Omega_{ci}^{-1}$. The contours are smoothed and on a logarithmic, such that F decreases by a factor of 4 for each contour going outwards.

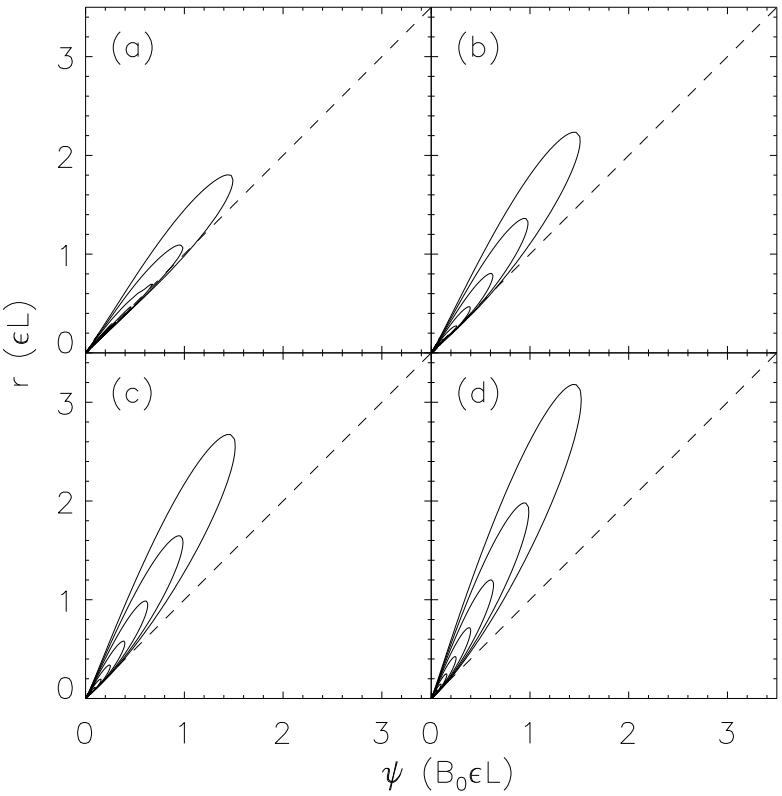

Figure 4.3: The steady state distribution function $F_\infty(\psi, r)$ for (a) $S_N^* = 40$, (b) $S_N^* = 400$, (c) $S_N^* = 4000$, and (d) $S_N^* = 40000$. The contours are logarithmic as in Fig. 4.2.

case, the solution barely deviates from the no-merging solution along the $\psi = B_0 r$ diagonal. In other words, island coalescence is not playing a significant role. As S_N^* increases, the degree of asymmetry follows suit. This should not surprise, since S_N governs the number of islands in the system N, and the merging terms are the only N^2 terms in Eq. (3.11). Naturally, the more islands present in the current sheet, the more likely island coalescence will play a role. Because islands gain area in merging, the large S_N^* solutions also attain larger r. This will be shown more formally in the following sections.

4.3 Moments of the evolution equation

4.3.1 Total island number N

The moments of Eq. (3.11) are of interest because the resulting equations predict quantities of global relevance. For example, integrating Eq. (3.11) in ψ and A will produce an equation for the total number of islands N, defined in Eq. (3.5). With the simplifying assumption that the merging velocity $v \approx c_A$, the moment equation for N becomes soluble. The analytical solution for N can then be compared with the numerical solution in Fig. 4.2.

Applying the operator $\int_0^\infty d\psi \int_0^\infty dA$ to the left-hand side of Eq. (3.11), the $\partial f/\partial\psi$ and $\partial f/\partial A$ terms vanish since $f \to 0$ as $\psi, A \to 0$ or $\psi, A \to \infty$. (More intuitively, those terms are responsible for island growth, so by necessity they conserve island number.) On the right-hand side, the source term simply becomes S_N, and if we assume that $v \approx c_A$, the merging integrals $\propto -N^2/2$. The factor of $-\frac{1}{2}$ derives

from the simple fact that two islands coalesce into one. The resulting equation for N is

$$\frac{dN}{dt} = S_N - \frac{c_A}{L}N - \frac{c_A}{2L}N^2. \tag{4.5}$$

Eq. (4.5) is a Riccati equation and can be solved analytically. We separate variables and integrate both sides to get

$$\begin{aligned} t - t_0 &= \int \frac{dN}{S_N - \frac{c_A}{L}N - \frac{c_A}{2L}N^2} = -\frac{2L}{c_A}\int \frac{dN}{(N+1)^2 - (2S_N^* + 1)} \\ &= \frac{2L}{c_A}(2S_N^* + 1)^{-\frac{1}{2}} \tanh^{-1}\left(\frac{N+1}{(2S_N^*+1)^{\frac{1}{2}}}\right) \end{aligned} \tag{4.6}$$

where S_N^* is as defined in Eq. (3.13). Solving for $N(t)$, we get

$$N(t) = (2S_N^* + 1)^{\frac{1}{2}} \tanh\left(\frac{t - t_0}{t_s}\right) - 1 \tag{4.7}$$

where

$$t_s = \frac{2L}{c_A}(2S_N^* + 1)^{-\frac{1}{2}} \tag{4.8}$$

is the time-scale for the system to reach a statistical steady state. To solve for the integration constant t_0, we employ the initial condition $N(0) = 0$, for which we find that

$$t_0 = -t_s \tanh^{-1}(2S_N^* + 1). \tag{4.9}$$

Substituting this back into Eq. (4.7), after some algebra we get

$$N(t) = \frac{(N_f + 2)\tanh\left(\frac{t}{t_s}\right)}{N_f + 1 + \tanh\left(\frac{t}{t_s}\right)} N_f \tag{4.10}$$

where

$$N_f = (2S_N^* + 1)^{\frac{1}{2}} - 1 \tag{4.11}$$

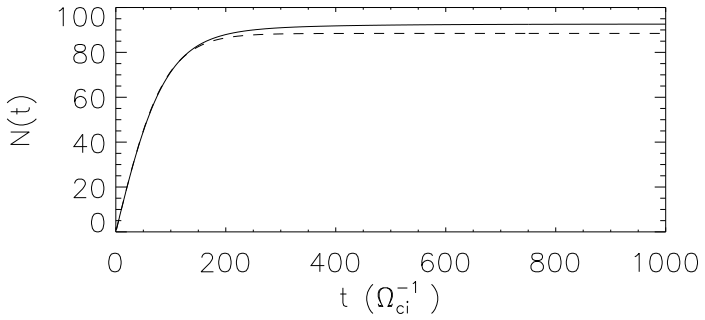

Figure 4.4: The number of islands N vs. t in the numerical solution (solid line; $S_N^* = 4000$, as in Fig. 4.2) and predicted by Eq. (4.10) (dashed line; $t_s \approx 89\Omega_{ci}^{-1}$, $N_f = 88$).

is the asymptotic number of islands in steady state when $t \gg t_s$. The form of $N(t)$ predicted by Eq. (4.10) shown in Fig. (4.4) compares favorably to that of the numerical solution, validating both the numerically integrated solution and the assumption that $v \approx c_A$.

4.3.2 Total island area A_T

Another quantity of interest is the total area of all the islands in the system

$$A_T = \int_0^\infty dA \int_0^\infty d\psi A f(\psi, A). \tag{4.12}$$

An equation for A_T can also be obtained by taking a moment of Eq. (3.11). However, a simpler approach is to take advantage of the known fact that the merging terms conserve A_T. Therefore, we instead take the second moment of Eq. (4.2), the evolution equation for $F(\psi, r)$ without merging. By applying the operator $\int_0^\infty \int_0^\infty dr\pi r^2$

to both sides, we get

$$\frac{dA_T}{dt} + \varepsilon c_A \int_0^\infty d\psi \int_0^\infty dr \pi r^2 \frac{\partial F}{\partial r} = \pi d_i^2 S_N - \frac{c_A}{L} A_T \tag{4.13}$$

where, as in the moment equation for N, the $\partial F/\partial\psi$ term vanished because $F(0,r) = F(\infty,r) = 0$, and we have used the delta function source given by Eq. (4.3) with $r' = d_i$. The second term can be integrated by parts:

$$\int_0^\infty d\psi \int_0^\infty dr \pi r^2 \frac{\partial F}{\partial r} = \int_0^\infty d\psi \; \pi r^2 F(\psi,r)\big|_{r=0}^\infty - \int_0^\infty d\psi \int_0^\infty dr 2\pi r F(\psi,r) \tag{4.14}$$

where, again, the former term vanishes since $F(\psi,0) = F(\psi,\infty) = 0$, and the second term is of course the first moment of F:

$$r_T = \int_0^\infty dA \int_0^\infty d\psi r F(\psi,r). \tag{4.15}$$

Thus, Eq. (4.13) becomes

$$\frac{dA_T}{dt} = \pi d_i^2 S_N + 2\pi\varepsilon c_A r_T - \frac{c_A}{L} A_T. \tag{4.16}$$

At late time, when the system has reached a statistical steady state, $dA_T/dt = 0$ and the source term is negligible. (Newly created islands are of negligible size compared to the existing islands.) Balancing the remaining two terms, we find that

$$A_T = 2\pi\varepsilon L r_T. \tag{4.17}$$

One might be tempted here to take the first moment of Eq. (4.2) and obtain closure for the moment equations by solving for r_T. Unfortunately, this does not work because the merging terms cannot be neglected. Whereas simple rules exist for N and A_T, r_T does not simplify so easily in the merging terms.

4.4 Solutions at large A

Of greatest interest in the distribution of islands are the largest, most easily observed islands. The behavior of these curves for the largest islands can be deduced from Eq. (3.11) for large A. As usual, simplifying the merging term requires some assumptions. We again assume that the merging velocity $v \approx c_A$, but also that the bulk of the islands are much smaller than A. Consequently, if we define

$$\int_A^\infty dA \bar{f}(A) \ll \int_0^\infty dA \bar{f}(A) \tag{4.18}$$

where

$$\bar{f}(A) = \int_0^\infty d\psi f(\psi, A). \tag{4.19}$$

is the distribution of islands in A with the ψ dependence integrated away. A similar assumption is made of ψ, so that $\int_0^\psi d\psi' \approx \int_0^\infty d\psi'$. The merging terms can then be written as

$$\begin{aligned}\left(\frac{\partial \bar{f}}{\partial t}\right)_{mrg} &\approx \frac{K_{mrg} c_A}{L} \int_0^\infty dA' \bar{f}(A') \bar{f}(A - A') - \bar{f}(A) \int_0^\infty dA' \bar{f}(A') \\ &\approx \frac{K_{mrg} c_A}{L} \int_0^\infty dA' \bar{f}(A') \left(\bar{f}(A - A') - \bar{f}(A)\right). \end{aligned} \tag{4.20}$$

where of course the source term does not contribute since it only generates small A islands. Again, since the majority of the islands are small compared to A, the contributions to $\int_0^\infty dA' \bar{f}(A')$ come primarily from $A' \ll A$. A Taylor expansion for $\bar{f}(A - A')$ about A gives:

$$\bar{f}(A - A') \approx \bar{f}(A) - A' \frac{\partial \bar{f}}{\partial A} + ... \tag{4.21}$$

Then Eq. (4.20) simplifies to

$$\left(\frac{\partial \bar{f}}{\partial t}\right)_{mrg} \approx -\frac{K_{mrg} c_A}{L} \int_0^\infty dA' A' \bar{f}(A') \frac{\partial \bar{f}}{\partial A}$$
$$\approx -\frac{K_{mrg} c_A}{L} A_T \frac{\partial \bar{f}}{\partial A} \tag{4.22}$$

With this expression for the merging terms, applying the $\int_0^\infty d\psi$ operator to Eq. (3.11) gives an evolution equation for $\bar{f}$ at large A:

$$\frac{\partial \bar{f}}{\partial t} + \frac{\partial}{\partial A}\left(\dot{A}\bar{f}\right) + \frac{K_{mrg} c_A}{L} A_T \frac{\partial \bar{f}}{\partial A} = -\frac{c_A}{L}\bar{f} \tag{4.23}$$

The third term on the left side, which arises from the merging terms, describes how large islands grow in area by devouring smaller islands. The coefficient $K_{mrg} c_A A_T / L$ is the rate at which the total area A_T of all the smaller islands is consumed.

Of course, A_T as defined by Eq. (4.12) is clearly dependent upon $\bar{f}$, but we will henceforth treat A_T as a constant determined by Eq. (4.16) and the moment equations. By balancing the second and third terms on the left side we obtain a characteristic length scale above which growth via reconnection dominates growth via merging. Accordingly, we would expect

$$\bar{F} \sim \exp\left(\frac{-r}{\hat{r}}\right) \tag{4.24}$$

with $\hat{r} = \varepsilon L$ in that regime, in accordance with Eq. (4.4) from the solution without merging. Recalling that $\dot{A} = 2\pi\varepsilon c_A r$, we find that the transition occurs at

$$R_T = \frac{K_{mrg} A_T}{2\pi\varepsilon L} = K_{mrg} r_T \tag{4.25}$$

from Eq. (4.17). In reality, by the very definition of r_T, all islands in the system must have $r < r_T$, so unless $K_{mrg} \ll 1$,[1] this regime will never be attained. Never-

[1] We will find in §5.2 that this is not the case.

theless, we will find it constructive to think of the solution as steadily approaching exponential-like behavior as we consider larger and larger r. In particular, we will find that Eq. (4.24) is close to valid for large r, with

$$\hat{r} = -\frac{1}{\dfrac{d}{dr}\ln \bar{F}_\infty} \tag{4.26}$$

approaching εL as $r \to \infty$.

Transforming Eq. (4.23) into an equation for $\bar{F}$ and substituting in R_T, we have

$$\frac{\partial \bar{F}}{\partial t} + \varepsilon c_A \frac{\partial \bar{F}}{\partial r} + \varepsilon c_A R_T \left(\frac{1}{r}\frac{\partial \bar{F}}{\partial r} - \frac{\bar{F}}{r^2} \right) = -\frac{c_A}{L}\bar{F} \tag{4.27}$$

from which we can solve for the steady state solution

$$\bar{F}_\infty(r) = \int_0^\infty d\psi F_\infty(\psi, r) \tag{4.28}$$

since Eq. (4.27) is now just a first-order differential equation in r. The result is

$$\int \frac{d\bar{F}_\infty}{\bar{F}_\infty} = \frac{1}{\varepsilon L}\int dr \frac{\varepsilon L R_T - r^2}{r(r+R_T)} = \frac{1}{\varepsilon L}\int dr \left(\frac{\varepsilon L}{r} + \frac{R_T - \varepsilon L}{r+R_T} - 1 \right) \tag{4.29}$$

$$\ln\left(\frac{\bar{F}_\infty}{\bar{F}_0}\right) = \ln\left(\frac{r}{\varepsilon L}\right) + \left(\frac{R_T}{\varepsilon L} - 1\right)\ln\left(\frac{r+R_T}{\varepsilon L}\right) - \frac{r}{\varepsilon L} \tag{4.30}$$

$$\bar{F}_\infty = C r \big(r + R_T\big)^{R_T/\varepsilon L - 1} \exp\left(-\frac{r}{\varepsilon L}\right) \tag{4.31}$$

where $\bar{F}_0$ and C are constants of integration. As previously suggested, the exponential behavior of Eq. (4.31) will dominate the polynomial factors for sufficiently large r. This self-consistently validates our assumption in Eq. (4.18).

Fig. 4.5(a) shows the distributions of islands in radius $\bar{F}_\infty(r)$ for each S_N (the ψ-integrated solutions from Fig. 4.3). The distribution function is shown on a log-

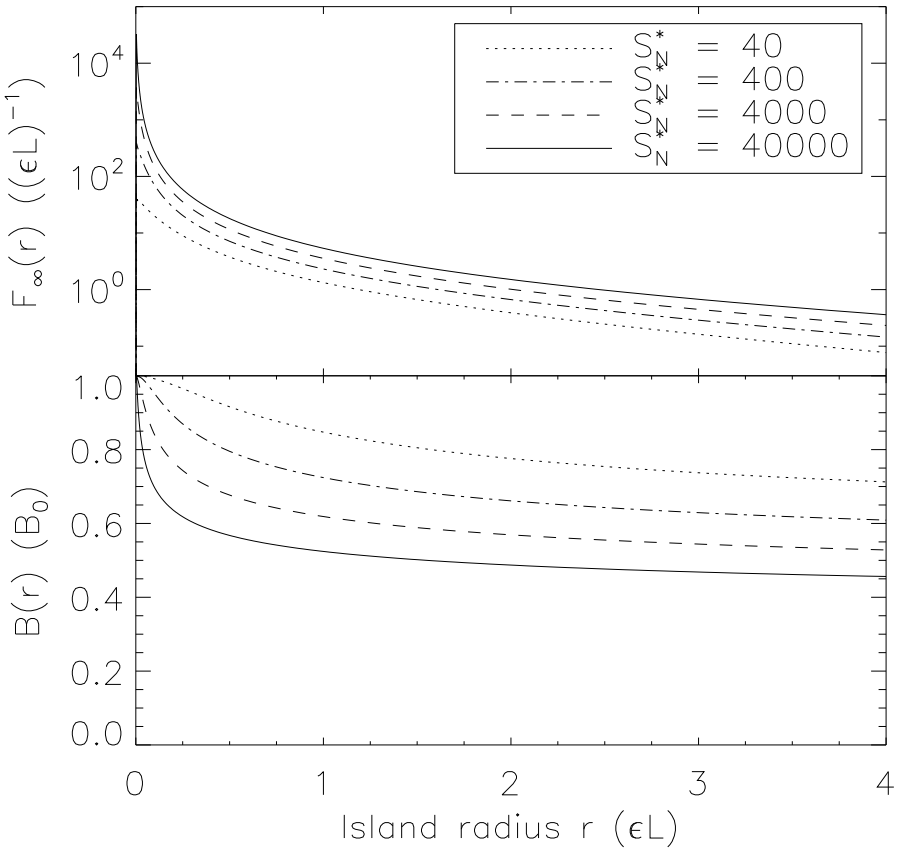

Figure 4.5: (a) The steady state distribution function in r, given by $F_\infty(r)$ as defined in Eq. (4.28) for various S_N. (b) The average magnetic field strength B as a function of island radius r for various S_N.

linear plot, so the nearly straight lines for large r are indicative of the exponential behavior in $\bar{F}_\infty$ predicted by Eq. (4.31).

The characteristic in-plane magnetic field $B = \psi/r$ will also be affected by island merging because merging increases island size but not flux. The largest islands, which may have attained their sizes from multiple mergers, typically have a weaker in-plane B. For larger S_N, where merging plays a more prominent role, this effect is more pronounced. This is borne out in Fig. 4.3(a), in that the steady state solution for larger S_N tilts farther away from the $\psi = B_0 r$ diagonal. Fig. 4.5(b) shows, for various S_N, that the average magnetic field strength as a function of island radius

$$B(r) = \frac{\int_0^\infty d\psi \frac{\psi}{r} F_\infty(\psi, r)}{\int_0^\infty d\psi F_\infty(\psi, r)} \tag{4.32}$$

is weaker for the largest islands, especially for larger S_N. In order to maintain force balance with the outside plasma, a weakened in-plane magnetic field should be accompanied by a compressed guide field B_z. Enhanced core fields are routinely observed in FTEs [141] and in magnetotail plasmoids [165].

It is now evident that both island merging and quasi-steady reconnection contribute to the growth of islands into macroscale objects. In the following chapter, we will further explore the competition between these two distinct mechanisms for island growth using a Hall MHD simulation of a large current sheet. This simulation is the first of its kind to investigate both mechanisms for island growth in a system of many islands.

Chapter 5

A Hall MHD simulation of many islands

We shall use the Hall MHD code F3D to test the model described in Ch. 3 against a simulated 2-D current sheet of length $L \sim 1638.4 d_i$. It is worth noting, however, that the simulation is not a perfect replica of the systems described by our model; some of the dynamics included in the statistical model are missing from the simulation. Nonetheless, it is useful in validating those aspects of the model that it does describe accurately, in particular the two mechanisms for island growth: quasi-steady reconnection and merging.

For the first of these mechanisms, the growth of islands is governed by a normalized reconnection rate ε. The characteristic radius $r = \sqrt{A/\pi}$ increases at the rate $\dot{r} = \varepsilon c_A$ and the flux increases at the rate $\dot{\psi} = \varepsilon c_A B_0$. In full particle-in-cell simulations of reconnection, after reaching a nonlinear stage, the normalized reconnection rate often plateaus at roughly $\varepsilon = 0.1$ [154]. Although resistive MHD simulations do not show reconnection rates this fast, the inclusion of the Hall term has been shown to enable reconnection rates comparable to those including kinetic effects explicitly [11]. Therefore, the Hall MHD simulations should describe accurately the island growth by quasi-steady reconnection in the system. With regards to the merging terms, although the incompressibility assumed by the model is not explicitly enforced by the code, in practice the density variations observed in Hall

MHD simulations of reconnection do not appear to be strong enough to significantly alter the merging rules described in §3.2, namely that the areas add but the flux of the merged island only takes on that of the larger of the two original islands. This quantitative difference in the two competing mechanisms for island growth will allow us to distinguish between them in the simulation. In particular, based on Eq. (4.25), K_{mrg} governs the relative importance of these two processes, so an important goal of these simulations is to fit to a value for K_{mrg} consistent with the results of the simulation.

Unfortunately, the Hall MHD code is not as effective in modeling the source term $S(\psi, A)$. PIC simulations have shown that in reconnecting current layers, islands form and are convected out, leaving behind a thin, elongated current sheet that is again unstable to island formation [46, 35, 63, 90, 93]. We therefore require $S(\psi, A)$ to generate islands continuously and at a steady rate. This process does not occur naturally in a Hall MHD simulation of reconnection. MHD simulations generate magnetic islands spontaneously for sufficiently large values of the Lundquist number, $S \gtrsim 3 \times 10^4$ [13, 8], but the onset of Hall reconnection during island formation sweeps away secondary islands, leaving a single large x-line [157]. Instead, we initialize the current sheets with a small perturbation to the magnetic field. The perturbations (with wavelengths down to $L_x/256$) eventually grow into hundreds of islands. Although the simulation does not properly describe spontaneous secondary island formation, the islands that do form as a result of the initial perturbation are quite small, comparable in size with those generated by a tearing mode instability. Also, this Hall MHD simulation does not model the convective loss term of Eq. (3.11)

because it employs periodic boundaries along the outflow. Periodicity is necessary because the simulation does not model island formation correctly yet, and it is preferrable that the islands remain in the simulation domain for as long as possible since the goal of the simulations is to explore the growth and dynamics of large numbers of magnetic islands.

5.1 F3D computational details

The 2D simulations were performed using the compressible two-fluid code F3D, which solves the Hall MHD equations [155]:

$$\frac{\partial n}{\partial t} = -\nabla \cdot \mathbf{J}_i \tag{5.1}$$

$$\frac{\partial \mathbf{J}_i}{\partial t} = -\nabla \cdot \frac{\mathbf{J}_i \mathbf{J}_i}{n} + \mathbf{J} \times \mathbf{B} - \frac{T}{n}\nabla n \tag{5.2}$$

$$\frac{\partial \mathbf{B}'}{\partial t} = -\nabla \times \mathbf{E}' \tag{5.3}$$

$$\mathbf{E}' = \frac{1}{n}\mathbf{J} \times \mathbf{B}' - \frac{1}{n}\mathbf{J}_i \times \mathbf{B} \tag{5.4}$$

$$\mathbf{B}' = (1 - d_e^2 \nabla^2)\mathbf{B} \tag{5.5}$$

$$\mathbf{J} = \nabla \times \mathbf{B} \tag{5.6}$$

where $\mathbf{J}_i$ is the ion flux, $\mathbf{u}_e = (\mathbf{J}_i - \mathbf{J})/n$ the electron velocity, and $d_e = c/\omega_{pe}$ the electron skin depth. The mass ratio $m_e/m_i = 1/25$, and the grid scale is $0.1d_i$, enough to marginally resolve the electron skin depth $d_e = 0.2d_i$. The system size is $L_x \times L_y = 1638.4d_i \times 204.8d_i$ with periodic boundary conditions. Magnetic fields and densities are normalized to their asymptotic values far from the current sheets, B_0 and n_0 respectively. (Quasineutrality is assumed, so that $n_i \approx n_e$). Time is

normalized to the ion cyclotron period, $t_0 = \Omega_i^{-1} = m_i c/eB_0$, length to the ion skin depth $L_0 = d_i = \sqrt{m_i c^2/4\pi n_0 e^2}$, velocity to the Alfvén velocity $v_0 = c_A = B_0/\sqrt{4\pi n_0 m_i}$, electric field to $E_0 = c_A B_0/c$, and temperature to $T_0 = m_i c_A^2$. The electron charge and ion mass are both normalized to unity.

The initial configuration consists of double Harris sheets of width $w_0 = d_i$:

$$B_x(y) = \begin{cases} B_0 \tanh\left(\dfrac{y - \frac{3}{4}L_y}{w_0}\right) & y < \dfrac{L_y}{2} \\ -B_0 \tanh\left(\dfrac{y - \frac{1}{4}L_y}{w_0}\right) & y > \dfrac{L_y}{2} \end{cases} \tag{5.7}$$

There is no initial guide field ($B_z = 0$). The density at the center of the current sheets is $1.5n_0$ and falls to $1.0n_0$ to balance magnetic pressure. The initial configuration also includes a magnetic perturbation with wave numbers up to $k = (5/32)d_i^{-1}$. This perturbation acts as the seed for magnetic islands. The maximum k produces perturbations with wavelength $L_x/256$. This ensures that each current sheet will produce $\gtrsim 100$ islands, sufficient for a statistically significant analysis. The simulation includes neither viscosity nor resistivity explicitly, but does include a fourth-order diffusion term for B in Faraday's law, Eq. (5.3). The fourth-order diffusion coefficient is initially $2 \times 10^{-5} d_i^4 \Omega_{ci}$ but later, in order to prevent grid-scale instabilities, is increased to $5 \times 10^{-5} d_i^4 \Omega_{ci}$ after the islands have grown from the initial perturbation to a discernible size. The time step starts off as $\Delta t = 0.04\Omega_{ci}^{-1}$ but is adjusted to $\Delta t = 0.025\Omega_{ci}^{-1}$ at the time of the increase of the fourth-order diffusion coefficient.

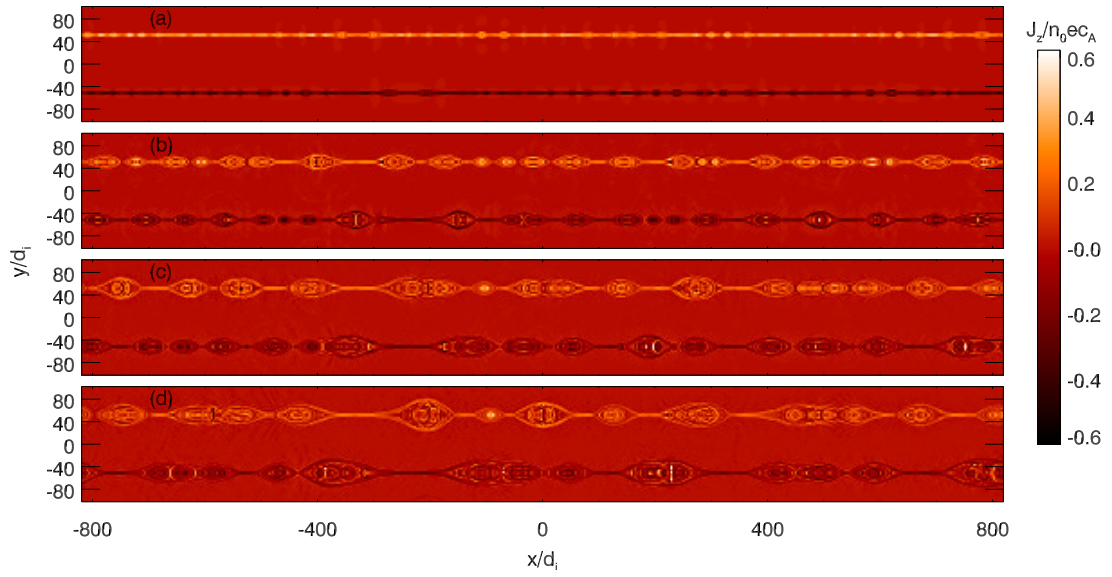

Figure 5.1: Snapshots of J_z in the Hall MHD simulation showing island formation, growth, and merging at (a) $t = 420\Omega_{ci}^{-1}$, (b) $t = 520\Omega_{ci}^{-1}$, (c) $t = 620\Omega_{ci}^{-1}$, and (d) $t = 686\Omega_{ci}^{-1}$. Values of J_z shown are capped at $J_z = \pm 0.6 n_0 e c_A$.

5.2 Simulation results and analysis

Fig. 5.1 shows the time-evolution of this system. The initial perturbations grow into magnetic islands that undergo the dynamics described above. The islands begin as very small perturbations that first grow into discernible islands in Fig. 5.1(a). In Fig. 5.1(b) these islands have reached scales large enough so that islands on a single layer interact with one another. The full merger of several islands is evident by Fig. 5.1(c). The final state of our simulation is shown in Fig. 5.1(d). Fig. 5.2 shows the positions of all the o-lines in the lower current sheet in time. The convergence of two or more o-lines indicates the coalescence of those islands.

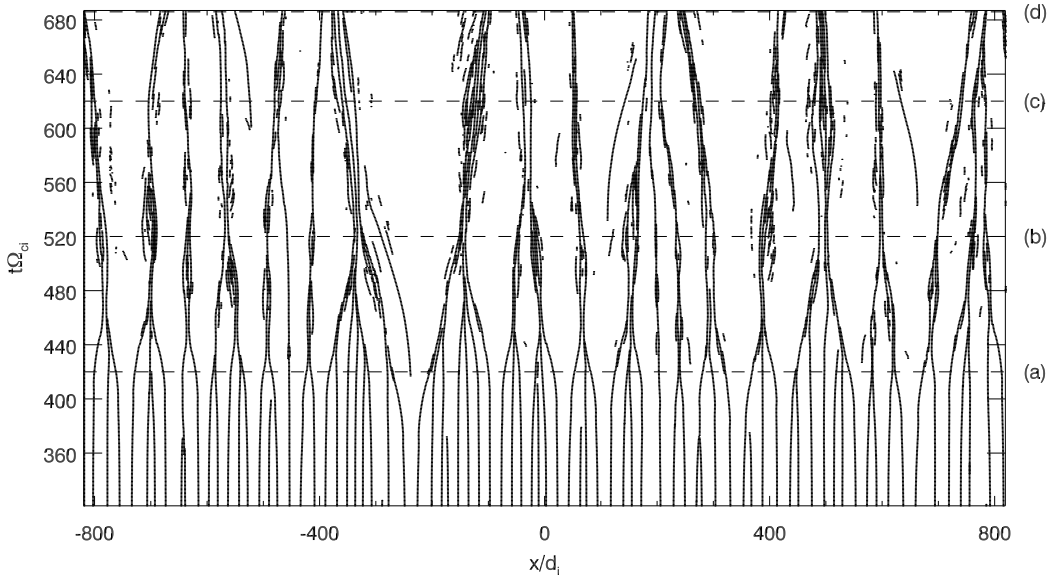

Figure 5.2: Location of all o-lines in time. Horizontal dashed lines correspond to snapshots of J_z in Fig. 5.1.

5.2.1 Characterizing the flux and size of islands

An automated algorithm goes through successive frames of the simulation and tracks the size and flux of each of the magnetic islands in a particular current sheet. The tracking algorithm calculates the flux function $\Psi(x, y)$ defined such that

$$\mathbf{B}(x, y) = \hat{\mathbf{z}} \times \nabla\Psi(x, y) + B_z(x, y)\hat{\mathbf{z}} \tag{5.8}$$

Contours of the flux function uniquely define the in-plane magnetic field. For a horizontal cut of the flux function $\Psi_{cut}(x)$ along the current sheet, the symmetry across the current sheet ensures that a local extremum in $\Psi_{cut}(x)$ corresponds to either a saddle point (x-line) or a local extremum (o-line) in $\Psi(x, y)$. For example, using the lower current sheet in our simulations, the x-lines (o-lines) correspond to local minima (maxima) in $\Psi_{cut}(x)$. (Fig. 5.2 tracks the positions of the o-lines

according to this definition.)

A magnetic island can now be defined by associating it with a particular x-line and a particular o-line. To do this, x-lines and o-lines are paired off by starting with the most highly embedded x-line, say, at $x_{X,1}$, and after considering each of those o-lines located within its separatrices on both the left and the right, pairing it with the o-line $x_{O,1}$ that minimizes $|\Psi_{cut}(x_{X,1}) - \Psi_{cut}(x_{O,1})$. This is repeated for the second most highly embedded x-line, and so on, eventually matching $x_{X,i}$ with $x_{O,i}$ for $i = 1, 2, ..., n$ for all n x-lines. Fig. 5.3(a) demonstrates this pairing scheme for a simple example. Note that defining islands in this way allows for islands to be contained entirely within other islands. This allows for a more realistic description of the merging process.

If the x-line between the two islands is pushing the two islands apart, as in Fig. 5.3(b), this definition introduces a small error in that the lesser island (island A on the left, in green), despite being very nearly the same size as the dominant island (island B on the right, in red), has a border completely within the dominant island. These two islands will both grow at similar rates, and their difference (signified by the region on the left surrounding island A but belonging to island B) becomes eventually negligible compared to their overall size. On the other hand, if the two islands are merging with one another as in Fig. 5.3(c), then the size of the dominant island (island A, in green) steadily increases as it consumes the lesser island (island B, in blue). Meanwhile, island B gradually shrinks until it is fully subsumed within island A.

Once all of the x-lines and o-lines have been paired off, then the flux ψ_i and

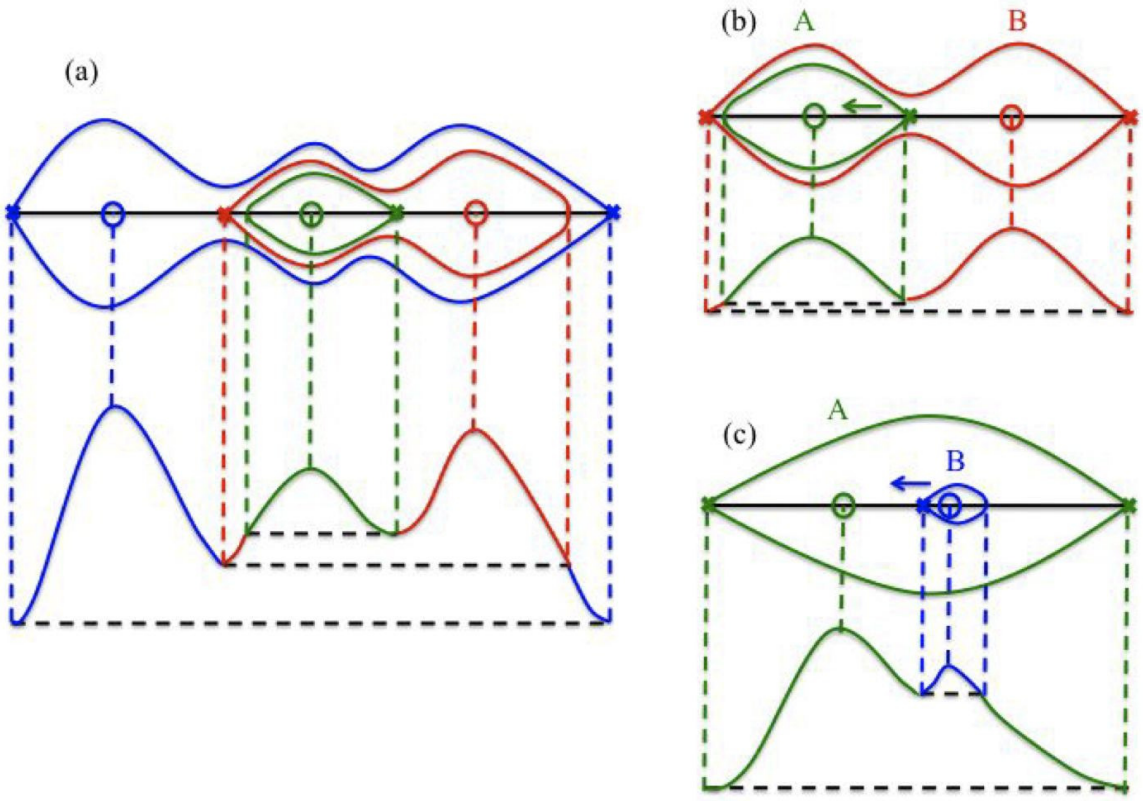

Figure 5.3: (a) A simple cartoon example of how magnetic islands can be defined by an x-line, o-line, and separatrix, all of the same color for a particular island. The corresponding $\Psi_{cut}(x)$ is shown below its current sheet, x-lines aligned with local minima and o-lines with local maxima. (b) A similar cartoon for two islands with a reconnecting x-line in between them pushing them apart. (c) Another example of two islands, now with a merging x-line in between. The lesser island shrinks as it is consumed by the dominant island.

area A_i of magnetic island i are simply given by:

$$\psi_i = \Psi_{cut}(x_{O,i}) - \Psi_{cut}(x_{X,i}) \tag{5.9}$$

$$A_i = \int_{R_i} dA \tag{5.10}$$

where R_i is the region defined by the separatrix of the x-line at $x_{X,i}$ for island i on the side that encompasses its o-line at $x_{O,i}$, but subtracting the regions of other islands entirely contained within R_i.

5.2.2 Tracking islands in $\psi - r$ phase space

Using this technique for any given time slice, each island can be plotted in the $\psi - r$ phase space as in Fig. 5.4. The selected times correspond to the snapshots in Fig. 5.1, with a green x corresponding to a particular magnetic island with flux ψ and characteristic radius r. By following the trajectories of individual islands, we can see both mechanisms for island growth at play. During normal island growth (quasi-steady reconnection), an island's trajectory through the $\psi - r$ phase space in Fig. 5.4 is generally along a diagonal with slope B_0 as reconnection injects flux into the island and consequently increases its area. Occasionally, a merger between two islands will push the dominant island off that diagonal into higher r, while not affecting its flux ψ. Meanwhile, the lesser island gravitates back towards the origin as it is consumed by the dominant one, losing both flux and area and eventually disappearing. The merging process therefore breaks the $\psi - r$ symmetry and allows islands to move above the symmetry diagonal $\psi = B_0 r$. The region below the symmetry diagonal in Fig. 5.4 is prohibited since no mechanism exists for increasing

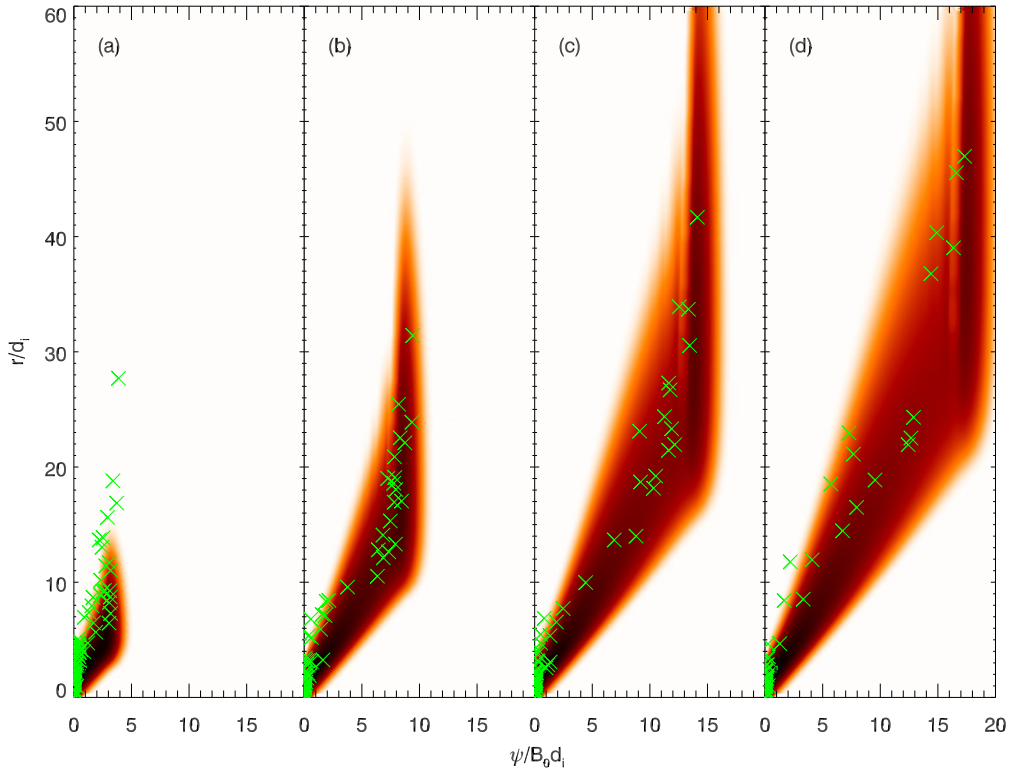

Figure 5.4: The distribution of islands in $\psi - r$ phase space in the Hall MHD simulation overlaid upon the the integrated numerical solution shown in red. Each island is marked by a green x – overlaid on top of a numerical solution to Eq. (3.11) at times (a) $t = 420\Omega_{ci}^{-1}$, (b) $t = 520\Omega_{ci}^{-1}$, (c) $t = 620\Omega_{ci}^{-1}$, and (d) $t = 686\Omega_{ci}^{-1}$. The numerical solution in red shows the evolution of Eq. (3.11) on a logarithmic scale with the parameters $L = 1638.4d_i$, $\varepsilon = 0.055$, $S_N = 1.5\Omega_{ci}$, and $K_{mrg} = 6$. This figure is also available as a movie in the online auxiliary material in Fermo et al. (2011) [62].

the flux ψ without also proportionally increasing the scale size r. In other words, the model predicts an allowed region,

$$\psi < B_0 r \tag{5.11}$$

that is consistent with all of the islands in the simulation.

5.3 Matching to the numerical solution

The results of the simulation allow us to study the two mechanisms for the growth of large islands by examining their trajectories in $\psi - r$ space and also to benchmark Eq. (3.11). Using the system size $L = 1638.4 d_i$, we empirically match the numerical solution of Eq. (3.11) to determine appropriate values for the reconnection rate ε and the merging coefficient K_{mrg} in the simulation. The quasi-steady reconnection rate ε governs the speed with which the distribution travels along the main diagonal $\psi = B_0 r$. In particular, since growth due to reconnection is the only mechanism that allows for growth in ψ, a simple empirical fit for $\dot{\psi} = \varepsilon c_A B_0$ yields ε.

A non-trivial numerical solution to Eq. (3.11) requires a source of island creation. The rate of island creation in Eq. (3.11) is $S_N = \int_0^\infty dr \int_0^\infty d\psi S(\psi, r)$. However, since the Hall MHD simulations do not produce islands naturally, this method is not a reliable predictor for S_N in actual space plasmas. (Future PIC simulations may produce a better model for predicting this quantity.) The choice of S_N will instead reflect a value that generates a total number of islands $N(t) = \int_0^\infty dr \int_0^\infty d\psi f(\psi, r, t)$ consistent with the number of islands in the Hall MHD simu-

lation exceeding some threshold flux $\psi_{min} \approx 0.5 B_0 d_i$. Although most of the islands arise directly from the initial perturbation, rapid island growth $\propto \varepsilon$ proceeds only after an initial period of stagnation. Different islands reach this stage of growth at different times; only after starting its rapid growth phase do we count an island towards the total number of islands N. For most islands, this growth phase was in a rougly $60\Omega_{ci}^{-1}$ interval (between $370\Omega_{ci}^{-1}$ and $430\Omega_{ci}^{-1}$ in Fig. 5.2).

We can also fit the merging coefficient K_{mrg}, which controls the relative magnitudes of the merging and island growth terms and drives the $\psi - r$ asymmetry. We adjust K_{mrg} until the asymmetry of the numerical solution accounts for all of the islands in the Hall MHD simulation.

Choosing $\varepsilon = 0.055$, $S_N = 1.5\Omega_{ci}$, and $K_{mrg} = 6$ produces the numerical solution shown in red in Fig. 5.4, or alternatively in the online auxiliary material for Fermo et al. (2011) [62]. The fact that K_{mrg} is greater than unity emphasizes that merging plays an even more important role than was hypothesized by the original model described in §3.3.1. The distributions of islands in the Hall MHD simulation (at the times of the panels shown in Fig. 5.1) are overlaid on top of the numerical solution of Eq. (3.11) in red in Fig. 5.4 as both evolve in time. The distribution of islands follows the numerical solution quite well. The number of islands tracked in the simulation still is not enough to interpolate this data to a smooth distribution function, so this is largely still just a qualitative comparison. Generating a smooth two-parameter distribution function from discrete data would require still many more islands, especially in the regions of our distribution that are of greatest interest (i.e., the largest islands). Nevertheless, the behavior of the

islands in our Hall MHD simulation shows that Eq. (3.11) effectively describes island growth by quasi-steady reconnection (along the diagonal in $\psi - r$ phase space) and coalescence (adding to the characteristic radius r but not its flux ψ). It is clear that island merging, and the subsequent asymmetry in $\psi - r$ phase space described in §4.2, plays an important role in the dynamics of this system.

Chapter 6

Island formation in a PIC simulation of guide field reconnection

In the previous chapter, we explored our model's two mechanisms for island growth using a Hall MHD simulation. A better understanding of the generation mechanism for magnetic islands (and consequently of the source term S_N in our model) is also highly desirable, and has been explored in other recent literature [46, 106, 144, 37]. The results of the present study point towards PIC simulations as the preferred method. Global simulations of the magnetopause, which often show at most a few FTEs at a time [135, 38, 121], might lack the resolution to see the small-scale FTEs generated at kinetic scales.

To this end, we return to the simulations performed by Drake et al. discussed in Ch. 2 and shown in Fig. 2.13 [46]. In those simulations, reconnection with a guide field led to elongated electron current sheets as described in §2.3.2, within which secondary islands developed. In this chapter, we perform similar simulations at high resolutions for the purpose of investigating how these secondary islands first form at scales of the electron skin depth. The 2D simulations were performed using the particle-in-cell code P3D, which evolves the electromagnetic field using the full Maxwell equations and steps particles forward using the Lorentz force law [187].

6.1 P3D computational details

The basic equations in the code use a normalization based on a reference density n_0 and magnetic field B_0 – for our reconnection simulations, the peak Harris sheet density (corresponding to about 100 particles per cell in our simulation) and the asymptotic upstream B_x. Given n_0 and B_0, we can normalize lengths to the ion skin depth $d_i = c\sqrt{m_i/4\pi n_0 e^2}$, time to the ion cyclotron period $\Omega_{ci}^{-1} = m_i c/eB_0$, velocities to the Alfvén speed $c_A = B_0/\sqrt{4\pi m_i n_0}$, the electric field to $E_0 = B_0 v_A/c$, and temperatures to $T_0 = m_i v_A^2$. With these normalizations, the relevant equations for P3D are Maxwell's equations

$$\frac{\partial \mathbf{B}}{\partial t} = -\nabla \times \mathbf{E} \tag{6.1}$$

$$\frac{\partial \mathbf{E}}{\partial t} = c^2(\nabla \times \mathbf{B} - \mathbf{J}) \tag{6.2}$$

$$\nabla \cdot \mathbf{B} = 0 \tag{6.3}$$

$$\nabla \cdot \mathbf{E} = c^2 \rho, \tag{6.4}$$

the equations of motions for ions

$$\frac{d\mathbf{x}}{dt} = \mathbf{v} \tag{6.5}$$

$$\frac{d(\gamma \mathbf{v})}{dt} = \mathbf{E} + \mathbf{v} \times \mathbf{B}, \tag{6.6}$$

and the equations of motions for electrons

$$\frac{d\mathbf{x}}{dt} = \mathbf{v} \tag{6.7}$$

$$\frac{d(\gamma \mathbf{v})}{dt} = -\frac{m_i}{m_e}(\mathbf{E} + \mathbf{v} \times \mathbf{B}) \tag{6.8}$$

where $\rho = e(n_i - n_e)$, $\mathbf{J} = e(n_i \mathbf{v}_i - n_e \mathbf{v}_e)$, and $\gamma = 1/\sqrt{1 - v^2/c^2}$.[1] In our simulation, $e = 1$, $c = 15$, and $m_i/m_e = 25$.

The equations of motion advance the particles relativistically in the Lorentz force law using the Boris algorithm [10]. Faraday's law steps the magnetic field and Ampère's law steps the electric field using a trapezoidal leapfrog algorithm, for which spatial derivatives are taken to second order. It turns out that this method also ensures that $\nabla \cdot \mathbf{B} = 0$ remains true for all times, as long as it holds true in the initial conditions. Gauss' law, on the other hand, can be violated due to accumulated discretization errors, so a correction to the electric field is regularly applied using a multigrid Poisson solver [179]. The simulation domain is $L_x \times L_y = 102.4 d_i \times 51.2 d_i$ with periodic boundary conditions, using 8192×4096 cells, ensuring that we comfortably resolve the electron skin depth $d_e = 0.2 d_i$. The time step is $0.0025 \Omega_{ci}^{-1}$.

The initial configuration consists of double Harris sheets of width $w_0 = d_i$:

$$B_x(y) = \begin{cases} B_0 \tanh\left(\dfrac{y - 3L_y/4}{w_0}\right) & y < L_y/2 \\ -B_0 \tanh\left(\dfrac{y - L_y/4}{w_0}\right) & y > L_y/2 \end{cases} \tag{6.9}$$

and a uniform guide field $B_g = 2B_0$. A magnetic field perturbation in each current sheet places x-lines at $(L_x/4, 3L_y/4)$ and $(3L_x/4, L_y/4)$, producing a single primary magnetic island on each current sheet. An ambient background density of $0.2 n_0$ supplements the Harris sheet density necessary to maintain pressure balance. The initial distribution is a Maxwellian with $T_e = 0.4 m_i c_A^2$ for the electrons and $T_i =$

[1] We distinguish between an individual particle's velocity $\mathbf{v}$ and the bulk ion or electron flow in a particular cell $\mathbf{v}_i$ or $\mathbf{v}_e$.

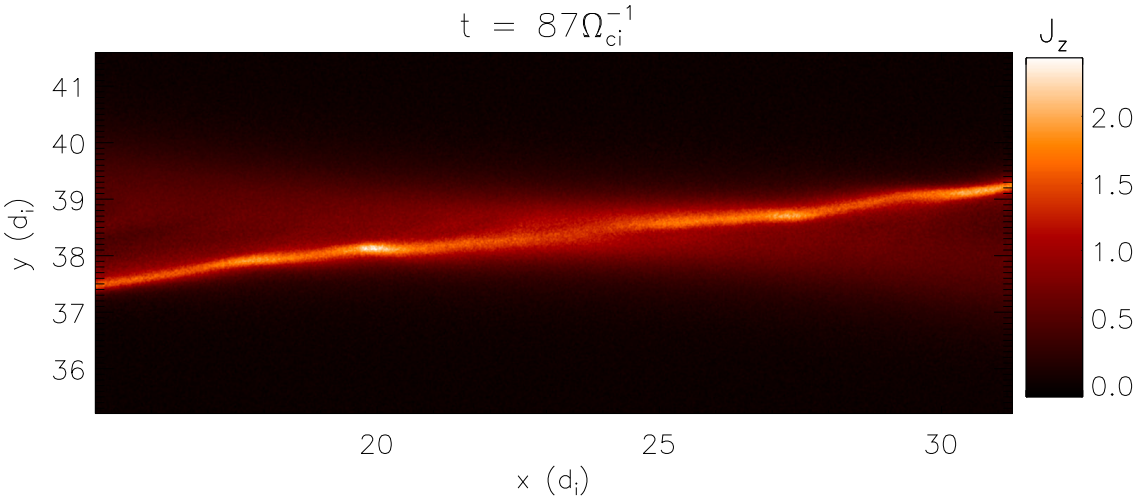

Figure 6.1: The out-of-plane current density J_z at $t = 87\Omega_{ci}^{-1}$ depicting the tilted electron current sheet. Compare with the simulation by Pritchett and Coroniti (2004) [133] in Fig. 2.11(a).

$0.1m_ic_A^2$ for the ions.

6.2 A non-tearing mechanism for island generation

Just as in the simulations of guide field reconnection by Drake et al. (2006) [46], our simulation produced a tilted electron current sheet along the separatrices, as described in §2.3.2 and depicted in Fig. 6.1. These current layers elongate and become unstable to the formation of secondary islands. In Drake et al. (2006), the creation of secondary islands is attributed to the tearing instability, citing that $k \sim 4.0d_i^{-1}$ and $w \sim 0.13d_i$ such that $kw \sim 0.5 < 1$ as required by Eq. (2.20). This is in accord with most of the present literature based on MHD theory [64, 17, 106],

MHD simulations [144], 2-D PIC simulations without a guide field [35, 63, 93], and most recently, in 3-D reconnection simulations [37]. However, we shall consider here whether a different mechanism can be responsible for the generation of magnetic islands.

6.2.1 Vortical flow in a secondary island

The impetus for such a consideration is illustrated in Fig. 6.2, which shows one such secondary magnetic island that had originally formed in the electron current sheet. The structure appears to be a simple magnetic island in Fig. 6.2(a), but a closer inspection reveals a surprising feature: vortical electron flows around the island. In Fig. 6.2(b), we see similarities to Kelvin-Helmholtz vortices associated with shear flows [91, 183].

Is it possible that the structure in Fig. 6.2 started out not as a magnetic island, but as a Kelvin-Helmholtz vortex? To answer this question, it would be beneficial to make a case study out of a single magnetic island, following it from its birth in the electron current sheet until it is expelled from the x-line region into the primary magnetic island. The island shown in Fig. 6.2 was born very close to the primary x-line around $4\Omega_{ci}^{-1}$ prior to the time shown. For this reason, the island continued to grow for some time without convecting away from the x-line. However, having been born so close to the primary x-line, it would be difficult to distinguish a tearing mode responsible for the island's birth from the primary x-line. A more interesting case study, then, is an island that was born along the tilted electron current sheet

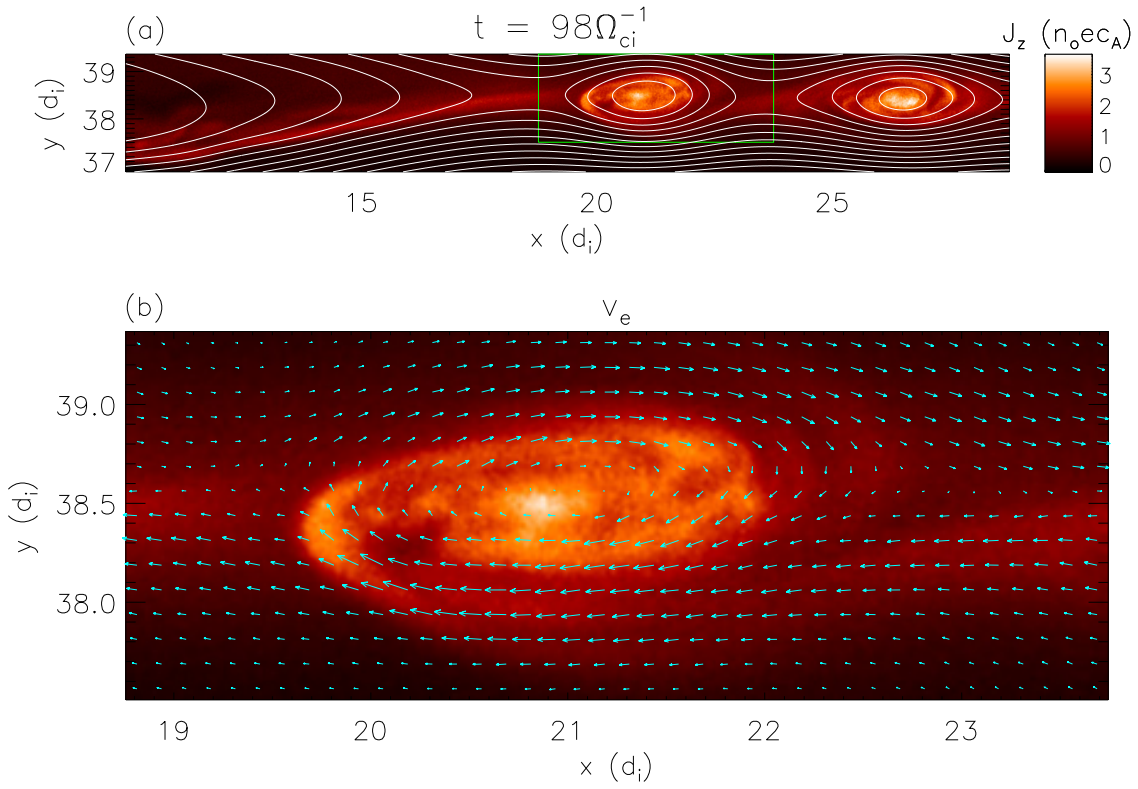

Figure 6.2: (a) The out-of-plane current density J_z and contours of the magnetic field near the x-line at $t = 98\Omega_{ci}^{-1}$. (b) A zoom-in of the region within the green box of (a), with arrows showing the electron flow v_e.

slightly away from the x-line, where it might be easier to distinguish between a fluid flow instability and the tearing instability.

6.2.2 Maturation of a d_e-scale vortex into a magnetic island

In particular, we observe an island along the tilted electron current sheet that started out quite small in Fig. 6.3, at the scale of the electron skin depth $d_e = 0.2d_i$, and $\sim 5d_i$ away from the primary x-line. Note in Fig. 6.3(a) that the J_z enhancement within the green box, which we might be inclined to call an "island," is in fact not an island at all. At this scale, within the electron current layer, the structure is still decoupled from the magnetic field. In fact, along the separatrix and away from the x-line, the current sheet is not close enough to the magnetic field reversal region to trigger the tearing instability. The lack of any inflow of plasma to either side of the structure in Fig. 6.3(b) corroborates this story. Instead, we find that (after transforming into the frame of the outflow of the primary reconnection x-line $v = -2c_A$) the electrons at this very early stage exhibit vortical flows, more consistent with a Kelvin-Helmholtz vortex than with a magnetic island generated by the tearing mode.

To verify the feasibility of such an explanation, Fig. 6.3(c) shows v_{ex} in the vicinity of this structure. Because it exists near the separatrix, there exists a sharp velocity gradient across the current sheet from $v_{ex} \approx 0$ to $v_{ex} \approx -2c_A$. The velocity shear is shown clearly in a vertical cut of v_{ex}, Fig. 6.3(d), along with the out-of-plane current sheet. Unsurprisingly, the vortex forms in the vicinity of the strongest

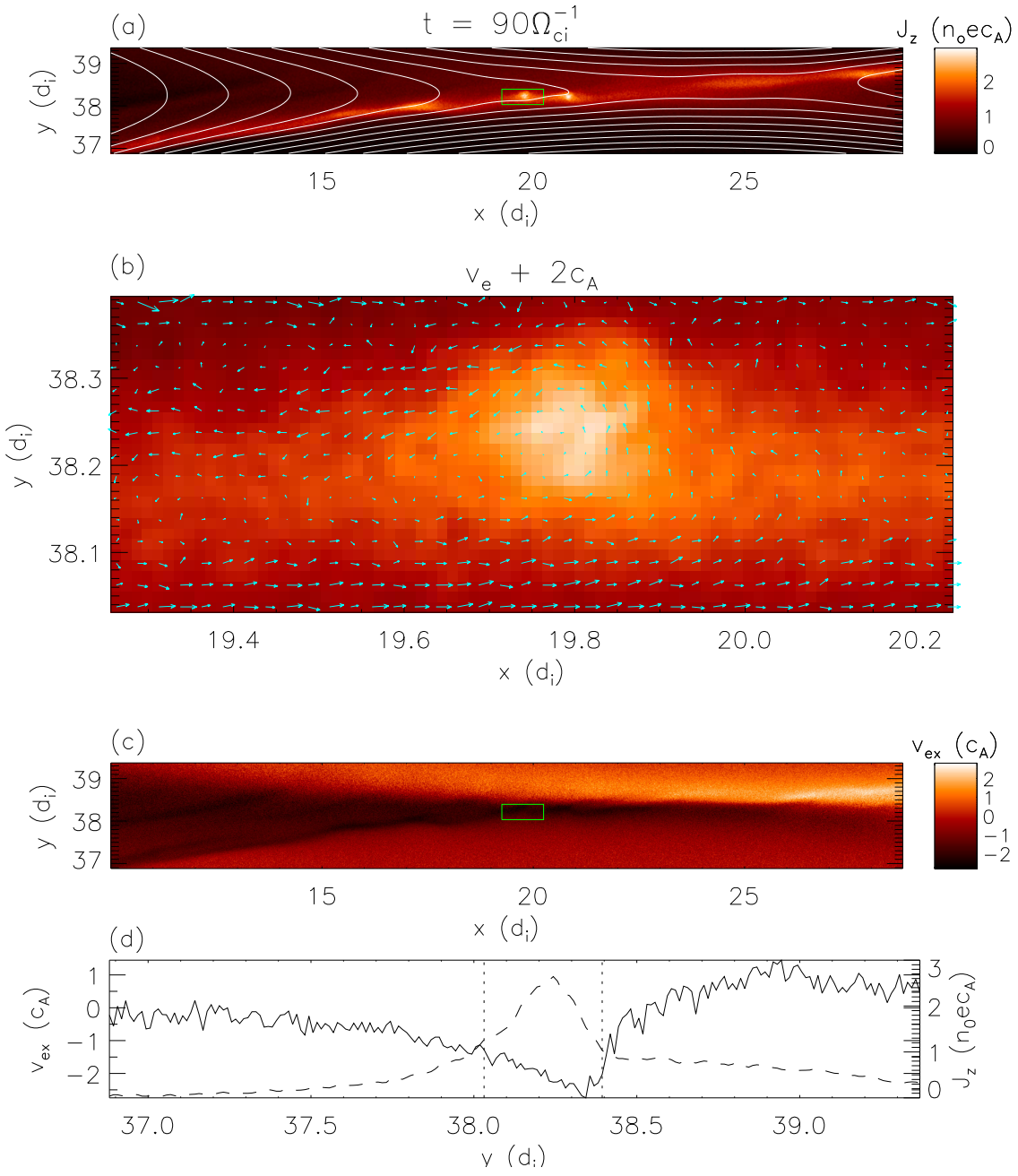

Figure 6.3: (a) The out-of-plane current density J_z and contours of the magnetic field near the x-line at $t = 90\Omega_{ci}^{-1}$. (b) A zoom-in of the region within the green box of (a), with arrows showing the electron flow in the frame of the outflow, $v_e + 2c_A$. (c) The reconnection electron outflow v_{ex}. (d) Vertical cuts of v_{ex} (solid curve) and J_z (dashed curve) through the center of the green box in (c), with dashed vertical lines denoting the top and bottom boundaries of the green box.

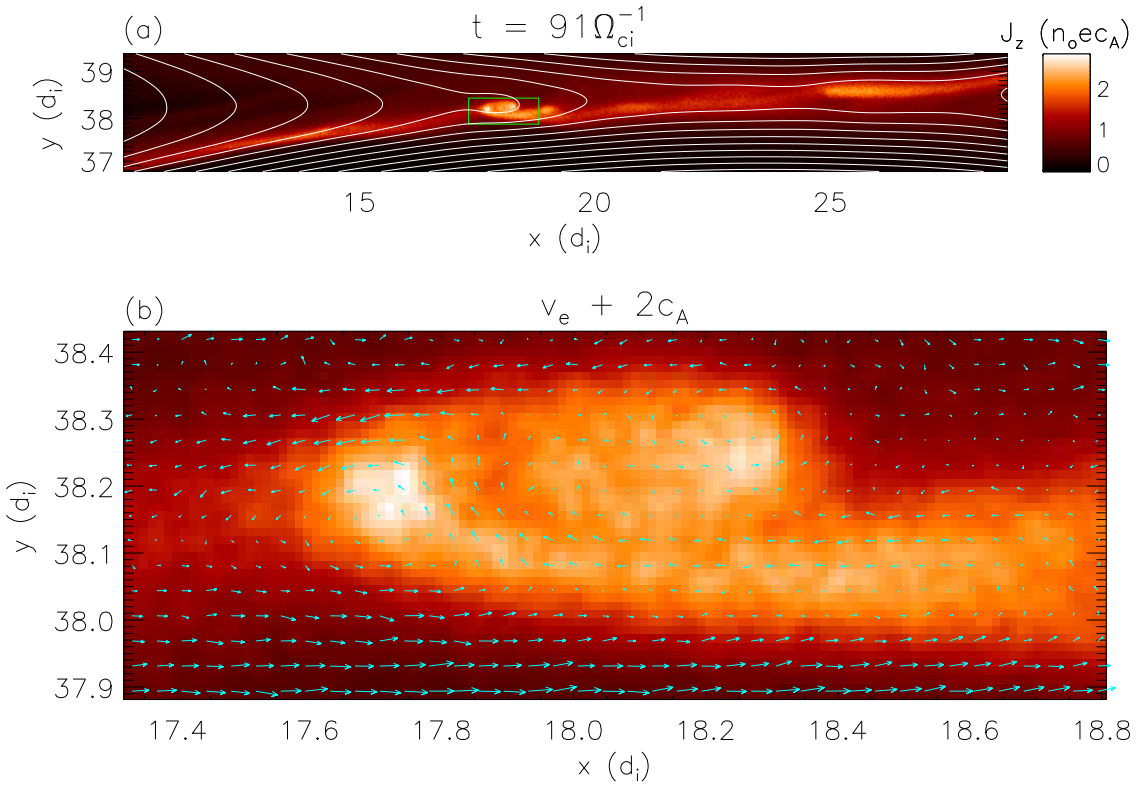

Figure 6.4: (a) The out-of-plane current density J_z and contours of the magnetic field near the x-line at $t = 91\Omega_{ci}^{-1}$. (b) A zoom-in of the region within the green box of (a), with arrows showing the electron flow in the frame of the outflow $v_e + 2c_A$.

velocity shear combined with the largest current density.

As the vortex flows away from the x-line, it appears to grow, as seen in Fig. 6.4. This growth is due to plasma flowing out from the x-line and piling up at the vortex. Although the vortex is itself flowing outwards, plasma accelerated by $E_\parallel$ streams along the current sheet and crashes into the vortex in Fig. 6.4(a). Another source of growth is that by $t = 91\Omega_{ci}^{-1}$, a vortex that was born slightly upstream of the vortex observed in Fig. 6.3 has collided with it, and the two are now spiraling

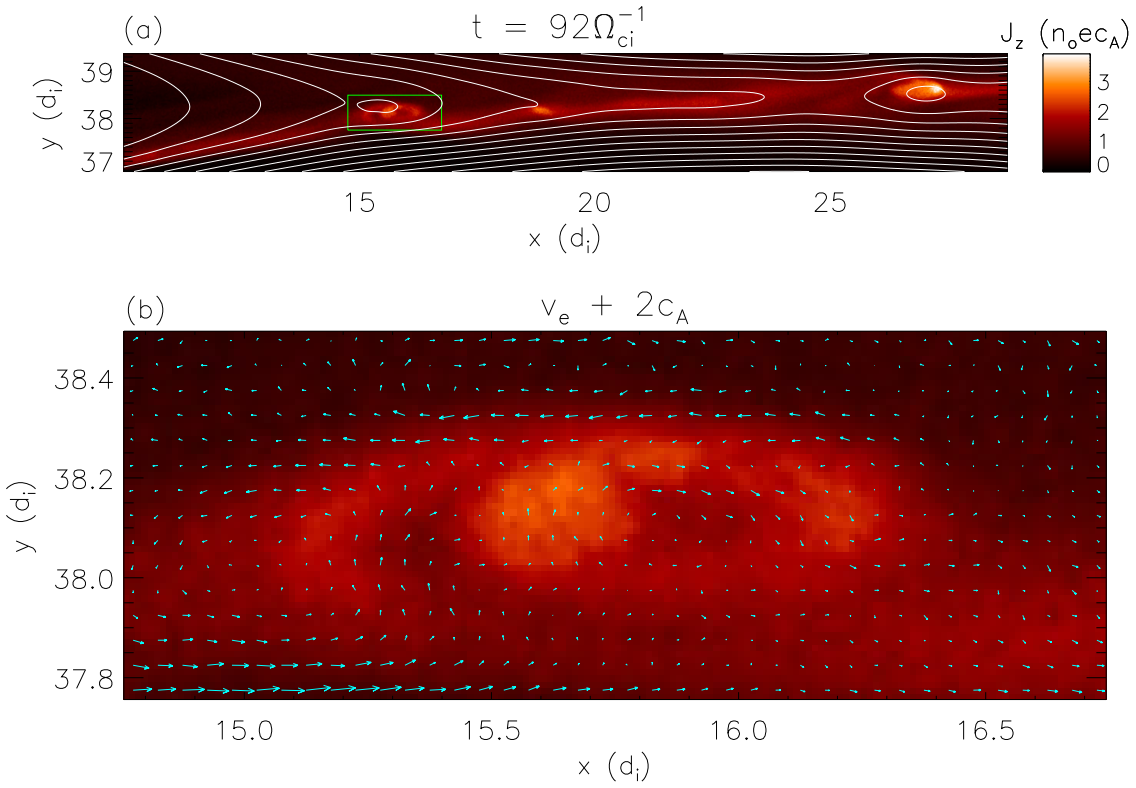

Figure 6.5: (a) The out-of-plane current density J_z and contours of the magnetic field near the x-line at $t = 92\Omega_{ci}^{-1}$. (b) A zoom-in of the region within the green box of (a), with arrows showing the electron flow in the frame of the outflow $v_e + 2c_A$.

around one another in Fig. 6.4(b). It is also worth pointing out that the vortex has now grown larger than a d_e, and consequently is now beginning to recouple to the magnetic field in Fig. 6.4(a).

In Fig. 6.5(a), the recoupling to the magnetic field has progressed even further so that the structure appears to be a true magnetic island. The coupling is still incomplete, however, as evidenced by the fact that the magnetic island is off-center from the J_z enhancement. Fig. 6.5(b) shows that the vortical flows have remained

intact, even though it is no longer a single coherent vortex. Unfortunately, we are not able to follow this particular structure much further because by now it has been ejected and is starting to interact with the primary island. Nonetheless, Fig. 6.2 showed that the flow vortices persisted for quite a long time in an island that had remained largely stationary. (Note that no frame transformation was necessary in Fig. 6.2(b) as was necessary for Figs. 6.3(b)-6.5(b).)

6.3 Implications for future work

The evidence from this simulation suggests that a fluid flow instability can be responsible for secondary island formation in component reconnection. The conditions under which this instability is dominant remain uncertain. To determine specifically whether these are Kelvin-Helmholtz vortices, as they appear to be, or the result of a type of streaming instability such as an electron-electron two-stream instability [172] or the Buneman instability [18], further studies of these types of simulations are warranted.

This distinction between islands generated by the is important for trying to understand the source term in our model. One might try to model the source term with linear MHD theories of plasmoid formation [106], but the results of this simulation and others [46, 35, 37] show that a complete picture of the dynamics of magnetic islands must start at scales as small as the electron skin depth d_e. If islands at these small scales are very numerous (corresponding to large S_N^* and large N), then solutions to our evolution equation will be in regimes where merging plays

an important role, as was found in our Hall MHD simulation of Ch. 5. Arguably, a more important question is whether the large scale current sheets in nature reside within these regimes of our model. In the following chapter, we shall address this question using observational data of flux transfer events observed by Cluster.

Chapter 7

Cluster observations of flux transfer events

As discussed in §2.2.1, flux transfer events (FTEs) were first identified by Russell and Elphic as flux ropes along the surface of the magnetopause, among the first observational evidence of reconnection [141, 142]. We equate them here with the magnetic islands seen in 2D simulations. The behavior of simulated FTEs in a global hybrid MHD simulation conducted by Omidi and Sibeck is consistent with that of the islands in our model [121]. The FTEs form (generally near the subsolar region), grow, merge, and convect poleward until they are ejected into the cusps. We therefore treat the magnetopause as a very long single current sheet with a length (south to north) of $L \sim 30R_E \sim 4000d_i$. In this chapter, based on this model of FTEs we shall compare observations by the four Cluster spacecraft to the predictions of our statistical model.

7.1 Dissecting the bipolar B_N signature

The distinct FTE signature is a magnetic field component normal to the magnetopause, B_N, that exhibits a bipolar signature [141, 142]. Fig. 7.1 shows a sample B_N profile for a flux transfer event. This data was taken from the ESA Cluster Active Archive, and also appeared in a study by Wang et al. [184]. The FTE exhibits the characteristic bipolar signature in B_N of Russell and Elphic [141]. This data

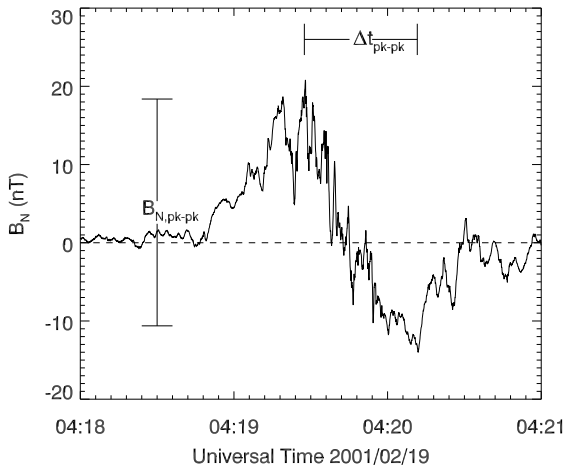

Figure 7.1: A sample flux transfer event observed by Cluster 4 at 0420 UT on 19 February 2001. The event occured at $(5.8, 4.7, 9.0)$ R_E in GSM coordinates.

was obtained from the fluxgate magnetotometer aboard Cluster spacecraft number 4 on a magnetopause crossing on 19 February 2001 at around 04:20 UT.

7.1.1 Extracting r and ψ from the bipolar B_N

During a three-year dayside phase of Cluster (2001-2003), the four spacecraft made numerous magnetopause crossings during which more than a thousand flux transfer events (FTEs) were identified for a statistical study by Wang et al. [184]. From each B_N profile and the plasma flow velocity, one can derive the approximate size of the FTE and the flux it contains. If the bipolar B_N signature is approximated by a sine wave, then we only need the time elapsed between peaks, Δt_{pk-pk}, the peak-to-peak magnitude of the B_N oscillation, $B_{N,pk-pk}$, and the plasma flow speed v_{FTE}. Fig. 7.1 shows how Δt_{pk-pk} and $B_{N,pk-pk}$ were calculated for the 19 February 2001

event. From these, a characteristic radius for the FTE can be calculated as

$$r_{meas} = v_{FTE}\Delta t_{pk-pk} \tag{7.1}$$

and its magnetic flux can be approximated by integrating half of the sine wave:

$$\psi_{meas} = \int_0^{\Delta t_{pk-pk}} dt v_{FTE} \frac{B_{N,pk-pk}}{2} \sin\left(\frac{\pi t}{\Delta t_{pk-pk}}\right) = \frac{1}{\pi} r_{meas} B_{N,pk-pk}. \tag{7.2}$$

As an example, the particular FTE whose B_N profile is shown in Fig. 7.1 has $v_{FTE} =$ 186 km/s, $\Delta t_{pk-pk} = 44$ s, and $B_{N,pk-pk} = 29$ nT, which yields $r_{meas} = 8214$ km $= 1.29 R_E$ and $\psi_{meas} = 2.38 \times 10^5$ nT $\cdot$ km.

This approach shows that an estimate for the scale size and flux of magnetic islands can be obtained from observational data, subject to a few assumptions. Consequently, there exist a few caveats to this approach for which we should account.

7.1.2 Magnetic field normalization

In our model and in the simulations, the magnetic field is normalized to the asymptotic magnetic field upstream of the reconnection site B_0, but the FTEs in our database span three years and many different solar wind and magnetospheric conditions. Therefore, in order to make a valid comparison with the model's predictions, the magnetic field $B_{N,pk-pk}$ should be normalized to the reconnecting component of the tangential (to the magnetopause) magnetic field surrounding the FTE, which we denote $B_{t,surr}$. The quantity $B_{t,surr}$ obtained from Cluster, however, may include a guide field component, for which we cannot account. The magnetic field normalization might therefore be overestimated if guide field reconnection is occurring in

the magnetopause. Determining the guide field requires knowledge of the flux rope orientation, which is itself a very difficult observational challenge.

Another concern is that the database of FTEs provides one of the $B_{t,surr}$ values for either the magnetosheath or the magnetosphere side, depending on which side of the magnetopause the particular spacecraft was on when it encountered the FTE. The proper normalization requires $B_{t,surr}$ for both sides. (Of the 1,098 events, 730 of them measured $B_{t,surr}$ on the magnetosheath side, 368 on the magnetosphere side.) For reconnection with asymmetric magnetic fields, the reconnection rate scales with the harmonic mean of the two upstream magnetic fields [21]:

$$B_0 = \frac{2B_{sheath}B_{sphere}}{B_{sheath} + B_{sphere}}. \tag{7.3}$$

Since our database only provides either B_{sheath} or B_{sphere}, the proper normalization B_0 may vary from the measured $B_{t,surr}$. After presenting the data we shall discuss how these normalization issues could potentially affect our data.

7.1.3 Dependence on spacecraft trajectory

Another limitation to consider is the uncertainty of the proximity of the spacecraft's trajectory to the center of the FTE. In principle, the method prescribed here should be most accurate for a trajectory that goes straight through the center of the FTE along the surface of the magnetopause, and more prone to error farther away from the center of the FTE. In actuality though, it is the FTE that passes over the spacecraft. Cluster 4 was traveling at an average speed of about 2.3 km/s when the 19 February 2001 FTE in Fig. 7.1 passed over the spacecraft, whereas the FTE flow

velocity was measured as 186 km/s in a direction effectively along the surface of the magnetopause (within 9°). Consequently, the spacecraft trajectory through the FTE is essentially parallel to the magnetopause surface. In the context of an island in the Hall MHD simulation performed in Ch. 5, such a trajectory corresponds to a horizontal cut through a magnetic island.

A typical island from the Hall MHD simulation performed in Ch. 5 is shown in Fig. 7.2(a). A typical spacecraft trajectory through the FTE at a distance $10d_i$ from the magnetopause surface (highlighted by a horizontal solid white line) would measure the bipolar B_N signature shown in Fig. 7.2(b). For this particular trajectory, r_{meas} can be calculated from the peak-to-peak separation and ψ_{meas} from the peak-to-peak B_N according to Eqs. (7.1)-(7.2). Performing this calculation for every horizontal cut across the magnetic island yields r_{meas} and ψ_{meas} as functions of y, the spatial separation between the trajectory and the current sheet. Both r_{meas} and ψ_{meas} as functions of y are shown in Fig. 7.2(c) and Fig. 7.2(d), respectively. The actual size r_{true} and flux ψ_{true} (determined as in §5.2) are displayed as dashed lines, for comparison. The measured values for both quantities are quite accurate when the trajectory passes through the island proper, even without going through the center. Far from the island, this method could overestimate the scale size and underestimate the flux, but in such cases where Cluster only passes by the outer edge of the FTE, the observed B_N profile will be weaker and generally more difficult to discern from the background noise. The signal-to-noise ratio is much lower in observational data such as Fig. 7.1 than in MHD simulations such as in Fig. 7.2(b). Therefore, such events are less likely to be recognized as FTEs by Cluster and should

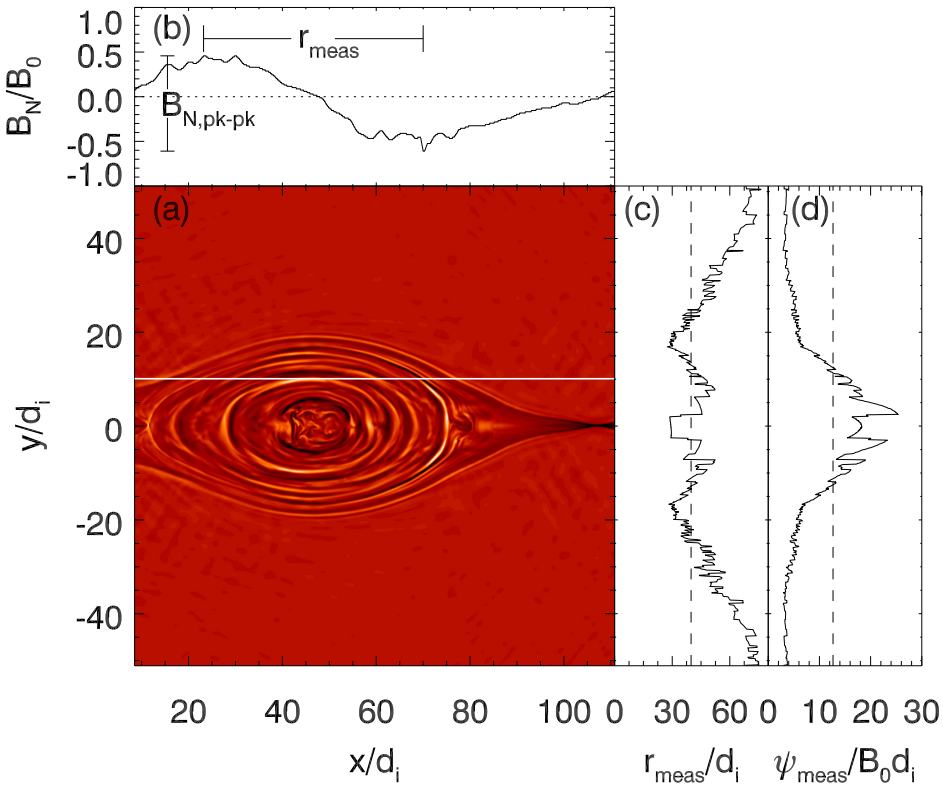

Figure 7.2: (a) J_z for a sample magnetic island from the Hall MHD simulation. (See Fig. 5.1.) (b) The bipolar B_N signature a spacecraft would measure from passing through this magnetic island traveling along the solid white horizontal line in (a), a distance $10d_i$ from the center of the main current sheet. To the right are (c) the scale size r_{meas} and (d) the magnetic flux ψ_{meas} that a spacecraft would measure by horizontally passing through the island a distance y from the current sheet. The dashed lines denote the actual scale size $r_{true} = (A_{true}/\pi)^{1/2}$ and magnetic flux ψ_{true}.

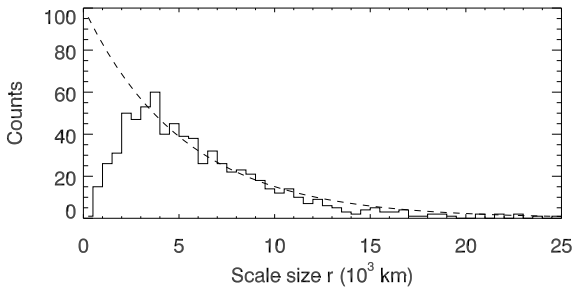

Figure 7.3: A distribution of the scale sizes of 1,098 flux transfer events detected by Cluster between 2001 and 2003. The dashed curve fits an exponential tail with $\hat{r} = 5277$ km to the tail of the distribution (beyond its peak).

not significantly skew the statistics.

7.2 A study of 1,098 FTEs

7.2.1 An exponential tail in r

The evolution equation, Eq. (3.11), normalizes length scales to εL. Direct measurements of the reconnection rate and magnetopause length are not possible, so in order to normalize the data properly, we approximate the numerical steady-state solution to Eq. (3.11) for the largest islands with an exponential tail for large r according to Eq. (4.24). Fig. 7.3 shows that the distribution of FTEs in r agrees well with an exponential fit for $\hat{r} = 5277$ km.

A numerical steady-state solution of the our evolution equation with $S_N^* = S_N K_{mrg} L/c_A = 24000$ yields an exponential tail with $\hat{r} = 2.64\varepsilon L$. (We now use $K_{mrg} = 6$ to match the results from §5.3.) Equating $\hat{r}$ with our FTE histogram so

that $\hat{r} = 2.64\varepsilon L = 5277$ km, we estimate that $\varepsilon L \approx 2000$ km. Using $L \approx 30 R_E$ for the magnetopause, one can also indirectly estimate the average reconnection rate to be $\varepsilon \approx 0.01$.

7.2.2 Asymmetry in $\psi - r$ phase space

Fig. 7.4(a) shows most of the 1,098 flux transfer events accordingly normalized, r to $\varepsilon L = 2000$ km and ψ to $B_{t,surr}\varepsilon L$. (Two events with ψ or r outside of the box are excluded.) These data points are overlaid on the aforementioned steady-state numerical solution to Eq. (3.11) with normalized source amplitude $S_N^* = S_N K_{mrg} L / c_A = 24000$. Qualitatively, the distribution of FTEs compares favorably with that predicted by the model, in that the distribution of islands appears to exhibit behavior consistent with island growth due to quasi-steady reconnection (along the symmetry diagonal) and merging (upward in phase space towards higher r). The large majority of the FTEs observed by Cluster fall into the region above the $\psi = B_{t,surr} r$ diagonal, as described by Eq. (5.11).

The 52 outliers below the diagonal (in red) have $\psi_{meas} > B_{t,surr} r_{meas}$. To account for these outliers, Fig. 7.4(b) shows the average in-plane magnetic field within the FTE $\psi_{meas}/B_{t,surr} r_{meas}$ versus $B_{t,surr}$. In this plot, we discover that the 52 outliers were normalized to a comparatively small $B_{t,surr}$, almost all less than the mean $B_{t,surr}$ of 23.4 nT. Furthermore, 42 out of the 52 outliers (or 81%) measured $B_{t,surr}$ in the magnetosheath, where typically $B_{sheath} < B_{sphere}$. In §7.1.2, we pointed out that the proper normalization for the magnetic field should have

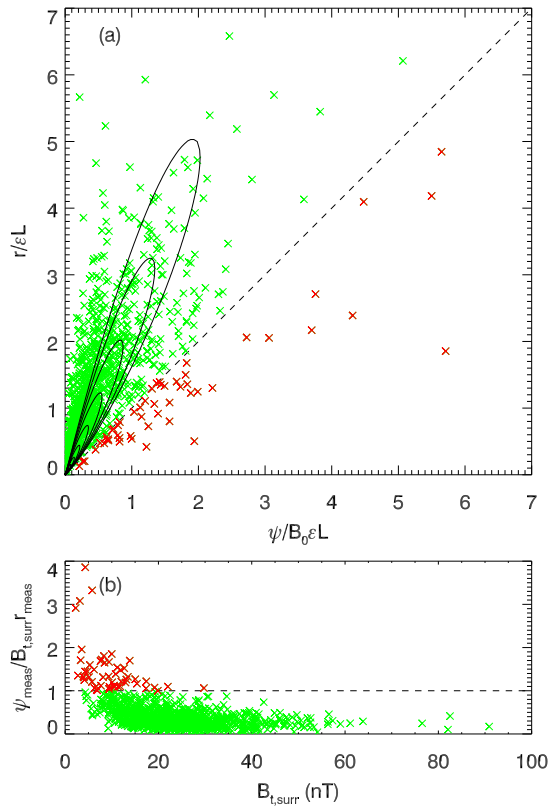

Figure 7.4: (a) The distribution of flux transfer events in $\psi - r$ phase space, overlaid on a numerical steady state solution to Eq. (3.11) for appropriate parameters. Flux transfer events above the $\psi = B_0 r$ diagonal are in green, whereas those in the prohibited region below the diagonal are marked in red. (b) The (normalized) average in-plane magnetic field within the FTE versus the absolute (non-normalized) $B_{t,surr}$. The horizontal dashed line corresponds to the diagonal dashed line of (a). Most of the outlier events have small $B_{t,surr}$.

accounted for B_t both in the magnetosheath and in the magnetosphere. When the measured $B_{t,surr}$ is quite small, it is quite likely that B_t is larger on the other side of the magnetopause. If this is the case, then Eq. (7.3) dictates that $B_0 > B_{t,surr}$ by as much as a factor of two. Although the data necessary to make this correction are not available, the fact that all of the outliers have low $B_{t,surr}$ suggests that the proper normalization could push many of those outliers back into the allowed region described by Eq. (5.11). On the other hand, if guide field reconnection is occurring, the presence of a guide field would have the opposite effect, since $B_{t,surr}$ would include the guide field component as well as B_0. Further observational work can be done to ascertain the guide field and magnetic field asymmetry in these events to obtain the corrent normalization for the magnetic fields, but obtaining this data remains a difficult challenge for observationalists.

7.3 Interpretation of the results

Normalization issues notwithstanding, the strong asymmetry in $\psi - r$ phase space indicates that, as in the Hall MHD simulations of Ch. 5, merging is a prominent factor in island dynamics. Yet for merging to play a significant role, very many islands must be present at any given time, most of them at small scales. How can we reconcile this statement with the precipitous dropoff in FTEs smaller than roughly 4000 km in Fig. 7.3? We attribute this dropoff not to a lack of FTEs $\lesssim$ 4000 km but to the decreased likelihood of a spacecraft passing through them.

Besides the indirect evidence for the preponderance of smaller FTEs on the

magnetopause, it should also be noted that 4000 km does not correspond to any physically significant scale for flux tube generation. Even assuming a simple linear tearing mode that produces FTEs typically with $kw \sim 1$, where $w \sim d_i \sim 50$ km is the current sheet width as in Eq. (2.20), then islands can be generated by the tearing mode as small as $2\pi/k \sim 2\pi w \sim 300$ km. The results of Ch. 6, simulations of collisionless reconnection [46, 35, 37], and observations of FTEs [178] and magnetotail plasmoids [51, 28], all point to the generation of these structures at small scales. Therefore, Fig. 7.3 probably does not paint the whole picture. A more likely scenario is that FTEs first form at d_e or d_i scales, then grow to macroscales $\gtrsim$ 4000 km. These smaller FTEs are probably much more numerous than those which can actually be observed by the spacecraft.

Chapter 8

Conclusions

Magnetic reconnection is a widespread phenomenon in laboratory, space, and astrophysical plasmas, responsible for the rapid conversion of magnetic energy into plasma flows. Magnetic islands – or their 3-D analogue, flux tubes – are the product of patchy (multiple x-line) reconnection and have been observed in the magnetopause, the magnetotail, and in coronal post-flare loops. Recently, they have been the subject of much scrutiny because of the role they could play in enhanced reconnection rates, turbulent reconnection, and particle energization. Nonetheless, a unified picture of magnetic islands, from their birth at kinetic scales to their growth into observable macroscale objects, has been lacking. In this thesis, we have attempted to bridge that gap with a model that treats islands on a statistical level for very large current sheets.

8.1 Summary of the model and relevant simulations

Because the current sheets in question are so large, we have proposed to model islands with a statistical distribution function $f(\psi, A)$. We pattern the evolution of f in time after the behavior of magnetic islands observed in simulations and observations of magnetic islands: creation of islands at d_i or d_e scales, growth via quasi-steady reconnection, convection out of the current sheet, and coalescence of

islands. These four processes are formalized mathematically into Eq. (3.11), our evolution equation for f. We consider steady state solutions of Eq. (3.11) to correspond to the state of the current sheet when the system has itself reached a statistical steady state.

Of the four kinds of behaviors considered, island coalescence had the most profound effect on the steady state solutions of Eq. (3.11). While island growth by quasi-steady reconnection added to the flux and to its size proportionately, merging introduced a $\psi - r$ asymmetry. The magnitude of that asymmetry corresponds to the relative significance of the merging terms, dictated by the total number of islands N, or equivalently, by the normalized rate of island creation S_N^*. We find that the rate of growth for the largest islands is governed both by the quasi-steady reconnection rate ε and by the presence of smaller islands to be devoured by merging.

These two competing mechanisms for island growth were the subject of study for our Hall MHD simulation of a large current sheet with many islands. The trajectories of islands in $\psi - r$ phase space was consistent with island growth by both quasi-steady reconnection (adding both area and flux along a diagonal in $\psi - r$) and merging (adding only to the area). Consequently, the predicted $\psi - r$ asymmetry was borne out in these simulations. We have also used the Hall MHD simulations to benchmark the model by comparing a numerical solution of Eq. (3.11) to the distribution of islands in the simulation. In particular, in fitting a value to the merging coefficient K_{mrg}, which regulates the relative importance of island merging and quasi-steady growth by reconnection, the result that $K_{mrg} \approx 6$ in our simulations underscores the importance of merging in very large systems with many

islands.

Whereas the Hall MHD simulation was capable of modeling the large simulation domains necessary to explore island growth, a PIC simulation was more suitable for investigating the small scales in which islands are created. Following upon the simulations of guide field reconnection in Drake et al. (2006) [46], we found that secondary islands are created when the tilted electron current sheet becomes narrow and elongated. Surprisingly, it was discovered that the islands did not appear to be generated by a tearing mode, but by a flow instability. The islands start off as a d_e-scale flow vortex disconnected from the magnetic field in a region of high velocity shear. As outflowing plasma piles up at these vortices, they grow and start to recouple to the magnetic field.

8.2 Comparing statistical studies of FTEs and SADs

Observations of 1,098 flux transfer events [184] from the four Cluster spacecraft are also consistent with the predictions of the model. The islands in the Hall MHD simulation and the FTEs observed by Cluster show good qualitative agreement with the predicted distributions of islands. More particularly, the preponderance of these islands reside in the allowed region predicted by Eq. (5.11). Just as in the Hall MHD simulations, this asymmetry is further evidence that island merging plays a significant role in the dynamics of the magnetopause. In this scenario, patchy reconnection generates many FTEs at small scales.

This suggests that reconnection is quite bursty at the magnetopause. Further-

more, the bulk of these islands will be quite small, perhaps too small for spacecraft instrumentation to resolve or to distinguish from noise. Even a large, detailed statistical study of FTEs such as that performed by Wang et al. [184] is likely to miss the preponderance of FTEs at small scales. Despite the dropoff in FTEs smaller than roughly 4000 km in Fig. (7.3), there is little reason to believe that flux tubes should spontaneously form at that particular size. Most likely, FTEs are generated at much smaller scales, whether by the tearing mode or otherwise, and then grow into the macroscale objects observed by Cluster.

We can also compare the results of our statistical study of magnetopause FTEs with another statistical study of magnetic islands observed in a very large current layer, namely, the work by McKenzie and Savage on supra-arcade downflows in post-flare coronal current sheets [148]. (Recall the discussion of these structures in §2.2.3, and in particular, Fig. 2.8.) As part of the work for her Ph.D. thesis, Sabrina Savage wrote a semiautomated algorithm to recognize these supra-arcade downflows in images of post-CME flare arcades. By tracking them through successive movie frames, they characterized these flux tubes by their speeds, sizes, and magnetic flux and generated histograms for this data [112].

The right hand side of Fig. 8.1 shows histograms for the areas and fluxes for SADs and SADLs observed by the SXT, XRT, and TRACE satellites [147, 148]. The resulting histogram could be described as consistent with exponential tails in r or ψ as described by Eq. (4.24). However, this assertion comes with many caveats. The histogram was generated from a composite of many different flares of different sizes observed by three different instruments with different resolution

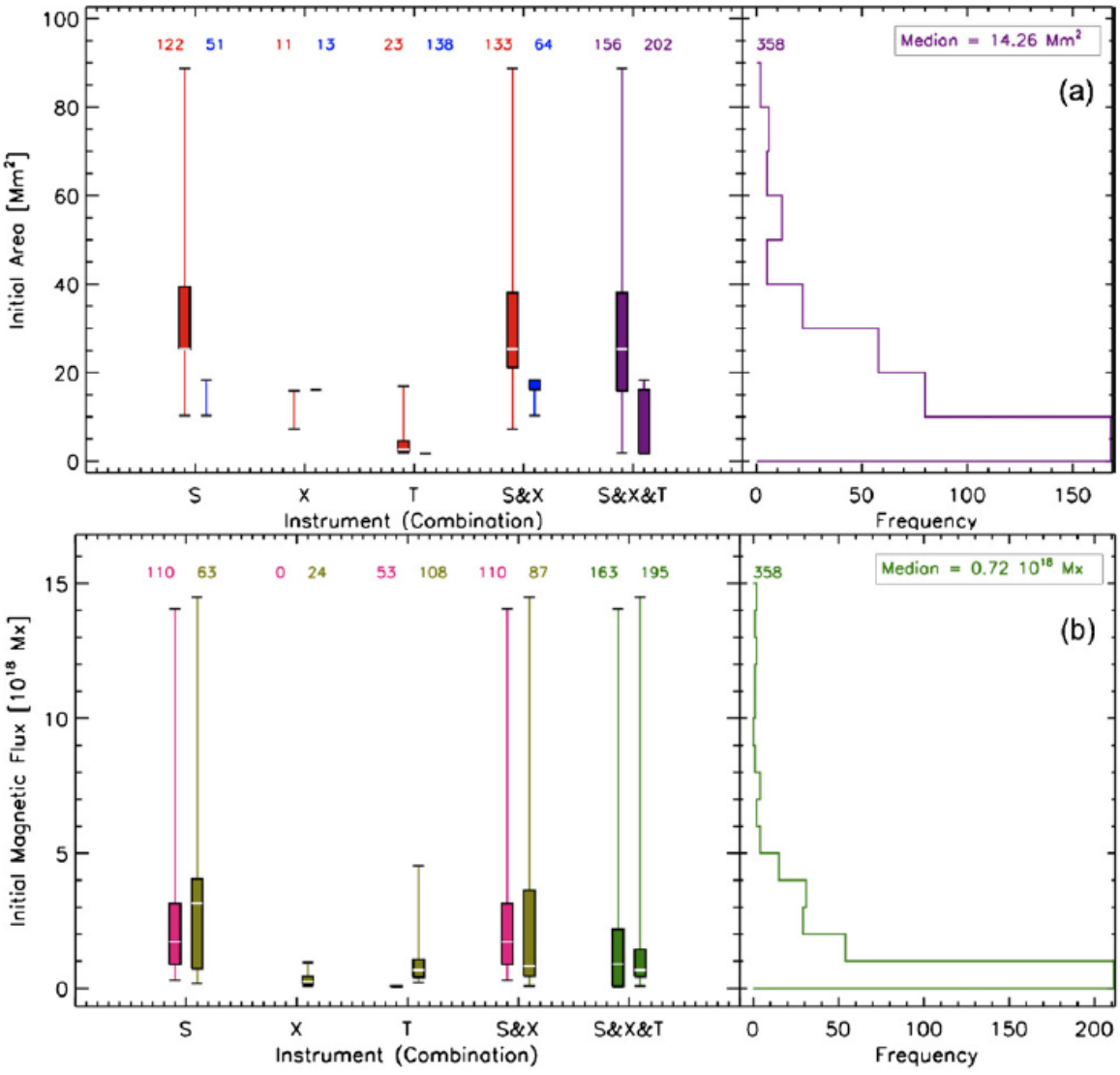

Figure 8.1: Histograms for the (a) areas and (b) fluxes of SADs and SADLs observed by SXT (S), XRT (X), and TRACE (T), accompanied on the left by quartile plots for each instrument's measurements of areas for SADs (left) and SADLs (right). Reprinted with permission from Savage and McKenzie (2011) [148]. ©2011 by the Institute of Physics.

capabilities at different viewing angles. The quartile plots on the left show the varying ranges observed by each instrument. Nonetheless, the plots are suggestive of the reasonableness of an exponential distribution.

To address some of these concerns, Fig. 8.2 shows histograms of area and flux for SADs (excluding SADLs) observed by SXT [113]. The TRACE images have higher resolution than SXT and accordingly revealed smaller SADs (as seen in their respective quartile plots in Fig. 8.1(a)), but their TRACE data set only included 23 SADs, insufficient for a statistically significant analysis. In comparison, 122 SADs were detected in their SXT data. By fitting to the SXT cumulative distribution functions, McKenzie and Savage concluded that the areas of SADs exhibit a log-normal distribution, while their fluxes are consistent with either a log-normal distribution or an exponential. However, as with the lack of FTEs $\lesssim 4000$ km in Fig 7.3, it is possible that a selection bias is responsible for the lack of SAD areas $\lesssim 30$ Mm^2 in Fig. 8.2. Near the resolution limitations of SXT, differentiating these smaller SADs from the background becomes more challenging. In a system with d_i on the order of meters, it is highly unlikely that flux tubes are being generated spontaneously at $\sim (30 \text{ Mm}^2)^{1/2} \sim 5$ Mm scales. Whether such a consideration would make either an exponential or a power-law distribution more likely remains to be determined.

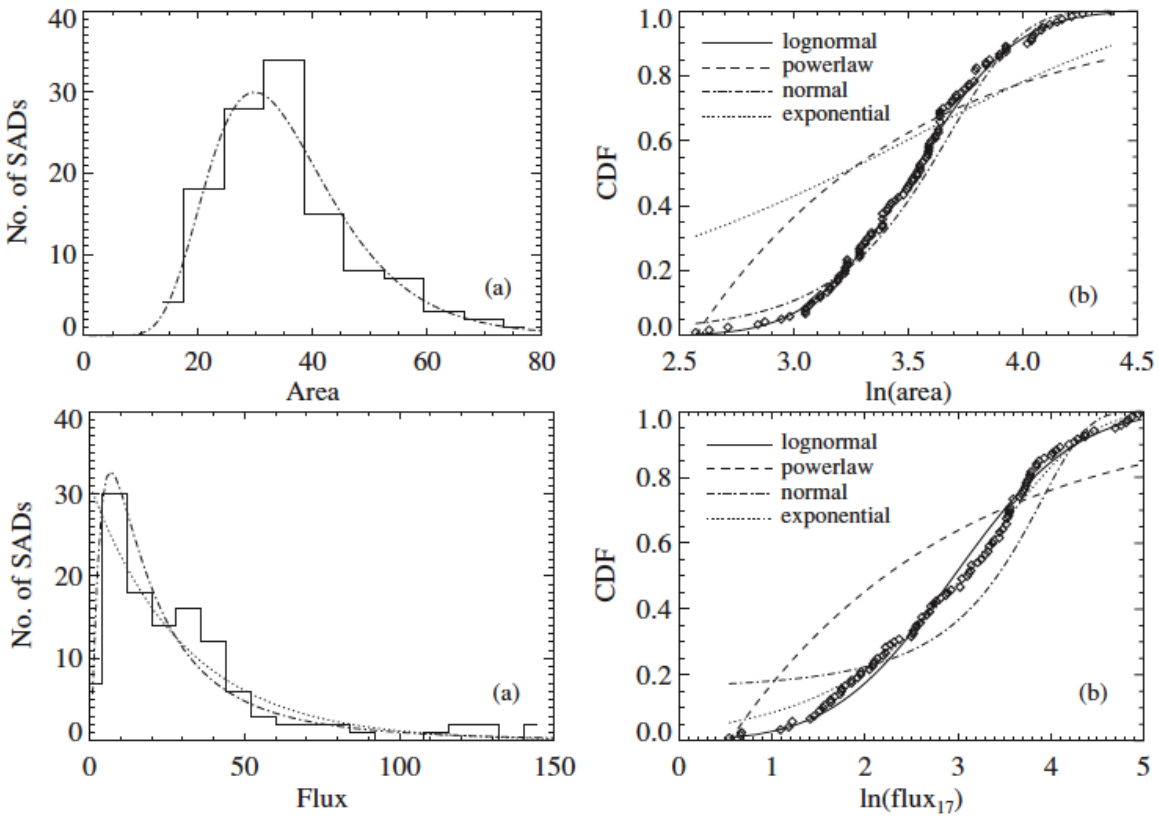

Figure 8.2: (a) Histograms for the areas and fluxes of SADs observed by SXT, shown with a fitted log-normal distribution (dash-dotted) and for the latter an exponential distribution (dotted). (b) Cumulative distribution functions of SAD areas and fluxes with corresponding theoretical CDFs. Reprinted with permission from McKenzie and Savage (2011) [113]. ©2011 by the Institute of Physics.

8.3 Future work

The results of the simulations and the observations of magnetic islands in nature show good qualitative agreement with the model's predicted distributions of islands. For example, the allowed region predicted by Eq. (5.11) and the corresponding $\psi - r$ asymmetry was observed both in the Hall MHD simulation and in the distribution of FTEs observed by Cluster. This is further evidence that island merging plays a significant role in the dynamics of long current layers. In this scenario, bursty reconnection generates many islands, most of which are smaller than the resolving capabilities of spacecraft instrumentation.

Nevertheless, continued work on this model would be profitable. The nature of 3-D reconnection, and in particular of flux tubes, is not yet well understood. Only very recent simulations have begun to explore the dynamics of flux tubes in 3-D reconnection simulations [37], so expanding this model into three dimensions would be very challenging. This thesis is just a first step towards understanding 2-D magnetic islands. A Hall MHD simulation that generates islands spontaneously and convects those islands outwards towards an open boundary would allow for a more direct comparison with our model. Further studies of the guide field PIC simulations would help to narrow down the nature of the flow instability responsible for secondary islands. The conditions under which this instability or tearing is the dominant mechanism for seeding magnetic islands are still being explored. Additional development of observational techniques to determine the FTE guide field and account for the magnetopause asymmetry using the Cluster data would increase

confidence in the magnetic field normalizations. The expected launch of Magnetospheric Multiscale Mission (MMS) will open doors to new microscale reconnection physics.

Lastly, the statistical study by McKenzie and Savage [112, 147, 148, 113] shows great promise for validating this model with observations of SADs in coronal post-flare loop arcades, especially if applied to images from the recently launched SDO mission. SDO images have higher resolution than the SXT images used to produce the distributions in Fig. 8.2. With more SDO images of coronal current sheets to complement the limited data from TRACE, one might find enough SADs at a sufficiently broad range of scales to compare with the predictions of this model. Despite the inherent challenges in describing systems with such a wide separation of scales, steady improvement in computational power, instrumentation capabilities, and observational techniques should enable a fuller and more complete theory of magnetic reconnection and magnetic islands.

Appendix A

Solar flare energy calculations

The largest flares release as much as 3×10^{32} erg of energy [131]. We consider a large flare (height $L \sim 10^5$ km, volume $V \sim h^3$) under coronal conditions (particle density $n \sim 3 \times 10^9$ cm^{-3}, temperature $T \sim 10^6$ K, and magnetic field $B \sim 100$ G). The energy in the magnetic fields is

$$E_B \sim \frac{B^2}{8\pi} L^3 \sim 4 \times 10^{32} \text{ erg.} \tag{A.1}$$

In constrast, the thermal energy available is just

$$E_T \sim nTL^3 \sim 10^{29} \text{ erg} \tag{A.2}$$

and the gravitational energy available is

$$E_G \sim G \frac{(m_H n L^3) M_\odot}{R_\odot^2} L \sim 5 \times 10^{29} \text{ erg} \tag{A.3}$$

where G is the gravitational constant, m_H the mass of hydrogen, $M_\odot$ the solar mass, $R_\odot$ the solar radius. Only the magnetic energy is adequate to explain the energy released by the largest solar flares.

Appendix B

Area conservation in merging terms

Consider the merging terms in Eq. (3.11):

$$\left(\frac{\partial f}{\partial t}\right)_{mrg} = \frac{1}{L}\int_0^A dA' f(\psi, A') \int_0^\psi d\psi' v(\psi, A', \psi', A - A') f(\psi', A - A') - \frac{1}{L} f(\psi, A) \int_0^\infty dA' \int_0^\infty d\psi' v(\psi, A, \psi', A') f(\psi', A'). \tag{B.1}$$

To find the rate of change in area from the merging terms, we multiply Eq. (B.1) by $AdAd\psi$ and integrate over all A and ψ:

$$\frac{dA_{mrg}}{dt} = \frac{1}{L}\int_0^\infty dAA \int_0^\infty d\psi \int_0^A dA' f(\psi, A') \int_0^\psi d\psi' v(\psi, A', \psi', A - A') f(\psi', A - A') - \frac{1}{L}\int_0^\infty dAA \int_0^\infty d\psi f(\psi, A) \int_0^\infty dA' \int_0^\infty d\psi' v(\psi, A, \psi', A') f(\psi', A'). \tag{B.2}$$

Note in the first term that $\int_0^\infty dA \int_0^A dA'$ is an integral over half of the $A - A'$ plane, namely, the $A' < A$ half, and so can also be written as $\int_0^\infty dA' \int_{A'}^\infty dA$. Thus,

$$\frac{dA_{mrg}}{dt} = \frac{1}{L}\int_0^\infty dA' \int_{A'}^\infty dA \int_0^\infty d\psi \int_0^\psi d\psi' A v(\psi, A', \psi', A - A') f(\psi, A') f(\psi', A - A') - \frac{1}{L}\int_0^\infty dA \int_0^\infty dA' \int_0^\infty d\psi \int_0^\infty d\psi' A v(\psi, A, \psi', A') f(\psi, A) f(\psi', A')). \tag{B.3}$$

Now, we define $A'' = A - A'$ and substitute for A into the first term:

$$\begin{aligned}
&\frac{dA_{mrg}}{dt} \\
&\quad = \frac{1}{L}\int_0^\infty dA' \int_0^\infty dA'' \int_0^\infty d\psi \int_0^\psi d\psi' (A' + A'') v(\psi, A', \psi', A'') f(\psi, A') f(\psi', A'') \\
&\qquad - \frac{1}{L}\int_0^\infty dA \int_0^\infty dA' \int_0^\infty d\psi \int_0^\infty d\psi' A v(\psi, A, \psi', A') f(\psi, A) f(\psi', A'). \quad \text{(B.4)}
\end{aligned}$$

Note that A, A', A'' are all simply dummy variables, so we may replace $A' \to A$ and $A'' \to A'$ in the first term. In doing so, the A part of the $(A + A')$ in the first term will cancel part of the second term, namely the $\psi' \in [0, \psi]$ part. The remainder is

$$\begin{aligned}
&\frac{dA_{mrg}}{dt} \\
&\quad = \frac{1}{L}\int_0^\infty dA \int_0^\infty dA' \int_0^\infty d\psi \int_0^\psi d\psi' A' v(\psi, A, \psi', A') f(\psi, A) f(\psi', A') \\
&\qquad - \frac{1}{L}\int_0^\infty dA \int_0^\infty dA' \int_0^\infty d\psi \int_\psi^\infty d\psi' A v(\psi, A, \psi', A') f(\psi, A) f(\psi', A') \\
&\quad = \frac{1}{L}\int_0^\infty dA \int_0^\infty dA' \int_0^\infty d\psi \int_0^\psi d\psi' A' v(\psi, A, \psi', A') f(\psi, A) f(\psi', A') \\
&\qquad - \frac{1}{L}\int_0^\infty dA \int_0^\infty dA' \int_0^\infty d\psi' \int_0^{\psi'} d\psi A v(\psi, A, \psi', A') f(\psi, A) f(\psi', A') \quad \text{(B.5)}
\end{aligned}$$

where, as we did with A and A', we have swapped the order of integration in ψ and ψ' in the second term while keeping $\psi < \psi'$. The merging velocity v is of course interchange symmetric, so

$$\frac{dA_{mrg}}{dt} = 0. \quad \text{(B.6)}$$

Bibliography

[1] S.-I. Akasofu. The development of the auroral substorm. *Planet. Space Sci.*, 12:273, 1964.

[2] S.-I. Akasofu, S. Chapman, and D. Vankatesan. The main phase of great magnetic storms. *J. Geophys. Res.*, 68:3345–3350, 1963.

[3] H. Alfvén. Existence of electromagnetic-hydrodynamic waves. *Nature*, 150:405–406, 1942.

[4] V. Angelopoulos, J. P. McFadden, D. Larson, C. W. Carlson, S. B. Mende, H. Frey, T. Phan, D. G. Sibeck, K.-H. Glassmeier, U. Auster, E. Donovan, I. R. Mann, I. J. Rae, C. T. Russell, A. Runov, X.-Z. Zhou, and L. Kepko. Tail reconnection triggering substorm onset. *Science*, 321(18):931, 2008.

[5] V. Angelopoulos, D. G. Mitchell, D. J. Williams, R. W. McEntire, A. T. Y. Lui, R. B. Decker, E. C. Roelof, S. P. Christon, S. Kokubun, T. Yamamoto, W. J. Hughes, J. C. Samson, E. Friis-Christensen, and K. Hayashi. Growth and evolution of a plasmoid associated with a small, isolated substorm: IMP 8 and GEOTAIL measurements in the magnetotail. *Geophys. Res. Lett.*, 22(22):3011–3014, 1995.

[6] K. Beckwith, J. F. Hawley, and J. H. Krolik. The influence of magnetic field geometry on the evolution of black hole accretion flows: similar disks, drastically different jets. *Ap. J.*, 678(2):1180, 2008.

[7] A. Bhatnagar and W. Livingston. *Fundamentals of solar astronomy.* World Scientific Publishing Co. Pte. Ltd., Singapore, 1949.

[8] A. Bhattacharjee, Yi-Min Huang, H. Yang, and B. Rogers. Fast reconnection in high-Lundquist-number plasmas due to the plasmoid instability. *Phys. Plasmas*, 16:112102, 2009.

[9] L. Biermann. Kometenschweife und solare korpuskularstrahlung. *Z. Astrophys.*, 29:274, 1951.

[10] C. K. Birdsall and A. B. Langdon. *Plasma Physics via Computer Simulations.* McGraw-Hill, New York, 1991.

[11] J. Birn, J. F. Drake, M. A. Shay, B. N. Rogers, R. E. Denton, M. Hesse, M. Kuznetsova, Z. W. Ma, A. Bhattacharjee, A. Otto, and P. L. Pritchett. Geospace Environmental Modeling (GEM) Magnetic Reconnection Challenge. *J. Geophys. Res.*, 106:3715, 2001.

[12] J. Birn, M. Hesse, and K. Schindler. MHD simulations of magnetotail dynamics. *J. Geophys. Res.*, 101(A6):12939–12954, 1996.

[13] D. Biskamp. Magnetic reconnection via current sheets. *Phys. Fluids*, 29:1520, 1986.

[14] G. S. Bisnovatyi-Kogan and S. I. Blinnikov. Disc accretion onto a black hole at subcritical luminosity. *Astron. Astrophys.*, 59(1):111–125, 1977.

[15] L. Boltzmann. Weitere Studien über das Wärmegleichgewicht unter Gasmolekülen. *Wiener Ber.*, 66:275, 1872.

[16] M. R. Brown and A. Martin. Spheromak experiment using separate guns for formation and sustainment. *Fusion Tech.*, 30:300, 1996.

[17] S. V. Bulanov, S. I. Syrovatskii, and J. Sakai. Stabilizing influence of plasma flow in dissipative tearing instability. *Pis'ma Zh. Eksp. Teor. Fiz.*, 28:177, 1978.

[18] O. Buneman. Instability, turbulence, and conductivity in current-carrying plasma. *Phys. Rev. Lett*, 1:8–9, 1958.

[19] R. C. Carrington. Description of a singular appearance seen in the sun on September 1, 1859. *Mon. Not. R. Astron. Soc.*, 20:13–15, 1859.

[20] P. Cassak. *Catastrophic model for the onset of fast magnetic reconnection.* PhD thesis, University of Maryland, 2006.

[21] P. Cassak and M. A. Shay. Scaling of asymmetric magnetic reconnection: general theory and collisional simulations. *Phys. Plasmas*, page 102114, 2007.

[22] P. A. Cassak, M. A. Shay, and J. F. Drake. Scaling of Sweet-Parker reconnection with secondary islands. *Phys. Plasmas*, 16:120702, 2009.

[23] S. Chapman. An outline of a theory of magnetic storms. In *Proc. R. Soc. Lond. A*, volume 95, pages 61–83, 1918.

[24] S. Chapman. The motion of a neutral ionized stream in the earth's magnetic field. In *Proc. Camb. Phil. Soc.*, volume 21, page 577, 1923.

[25] S. Chapman and V. C. A. Ferraro. A new theory of magnetic storms. *Nature*, 126:129–130, 1930.

[26] S. Chapman and V. C. A. Ferraro. A new theory of magnetic storms. *Terr. Magn. Atmos. Electr.*, 36(3):171–186, 1931.

[27] P. Charbonneau, S. W. McIntosh, H.-L. Liu, and T. J. Bogdan. Avalanche model for solar flares. *Solar Phys.*, 203(2):321–353, 2001.

[28] L.-J. Chen, N. Bessho, B. Lefebvre, H. Vaith, A. Fazakerley, A. Bhattacharjee, P. A. Puhl-Quinn, A. Runov, Y. Khotyaintsev, A. Vaivads, E. Georgescu, and R. Torbert. Evidence of an extended electron current sheet and its neighboring magnetic island during magnetotail reconnection. *J. Geophys. Res.*, 113:A12213, 2008.

[29] L.-J. Chen, A. Bhattacharjee, P. A. Puhl-Quinn, H. Yang, N. Bessho, S. Imada, S. Muhlbachler, P. W. Daly, B. Lefebvre, Y. Khotyaintsev, A. Vaivads, A. Fazakerley, and E. Georgescu. Observation of energetic electrons within magnetic islands. *Nature Phys.*, 4:19–23, 2008.

[30] A. Ciaravella and J. C. Raymond. The current sheet associated with the 2003 November 4 coronal mass ejection: density, temperature, thickness, and line width. *Ap. J.*, 686:1372–1382, 2008.

[31] G. C. Claridge. Coronium. *R. Astron. Soc. Can.*, 31(8):337–346, 1937.

[32] E. W. Cliver and L. Svalgaard. The 1859 solar-terrestrial disturbance and the current limits of extreme space weather activity. *Sol. Phys.*, 224:407–422, 2004.

[33] C. D. Cothran, M. Landreman, M. R. Brown, and W. H. Mattheaus. Generalized Ohm's law in a 3-D reconnection experiment. *Geophys. Res. Lett.*, 32:L03105, 2005.

[34] R. Dailey, C. A. Cattell, F. S. Mozer, and J. Berchem. Electric fields and convection velocities associated with flux transfer events. *Geophys. Res. Lett.*, 12(12):843–846, 1985.

[35] W. Daughton, H. Karimabadi, and J. Scudder. Fully kinetic simulations of undriven magnetic reconnection with open boundary conditions. *Phys. Plasmas*, 13:072101, 2006.

[36] W. Daughton, V. Roytershteyn, B. J. Albright, H. Karimabadi, L. Yin, and K. J. Bowers. Transition from collisional to kinetic regimes in large-scale reconnection layers. *Phys. Rev. Lett.*, 103:065004, 2009.

[37] W. Daughton, V. Roytershteyn, H. Karimabadi, L. Yin, B. J. Albright, B. Bergen, and K. J. Bowers. Role of electron physics in the development of turbulent magnetic reconnection in collisionless plasmas. *Nature Phys.*, 7:539–542, 2011.

[38] J. C. Dorelli and A. Bhattacharjee. On the generation and topology of flux transfer events. *J. Geophys. Res.*, 114:A06213, 2009.

[39] J. C. Dorelli and J. Birn. Electron magnetohydrodynamic simulations of magnetic island coalescence. *Phys. Plasmas*, 8(9), 2001.

[40] J. G. Doyle, P. B. Byrne, and G. H. J. van den Oord. Ultraviolet flares on II Pegasi. *Astron. Astrophys.*, 24:153–161, 1989.

[41] J. F. Drake, M. Opher, M. Swisdak, and J. N. Chamoun. A magnetic reconnection mechanism for the generation of anomalous cosmic rays. *Ap. J.*, 709:963–974, 2010.

[42] J. F. Drake and M. A. Shay. Fundamentals of collisionless reconnection. In J. Birn and E. R. Priest, editors, *Reconnection of Magnetic Fields: Magnetohydrodynamics and Collisionless Theory and Observations*. Cambridge University Press, Cambridge, U.K., 2007.

[43] J. F. Drake, M. A. Shay, and M. Swisdak. The hall fields and fast magnetic reconnection. *Phys. Plasmas*, 15:042306, 2008.

[44] J. F. Drake, M. A. Shay, W. Thongthai, and M. Swisdak. Production of energetic electrons during magnetic reconnection. *Phys. Rev. Lett.*, 94:095001–1–4, 2005.

[45] J. F. Drake, M. Swisdak, H. Che, and M. A. Shay. Electron acceleration from contracting magnetic islands during reconnection. *Nature*, 443:553, 2006.

[46] J. F. Drake, M. Swisdak, K. M. Schoeffler, B. N. Rogers, and S. Kobayashi. Formation of secondary islands during magnetic reconnection. *Geophys. Res. Lett.*, 33:L13105, 2006.

[47] J. F. Drake, M. Swisdak, M. A. Shay, B. N. Rogers, A. Zeiler, and C. Cattell. Formation of electron holes and particle energization during magnetic reconnection. *Science*, 299:873, 2003.

[48] J. W. Dungey. Conditions for the occurrence of electrical discharges in astrophysical systems. *Phil. Mag.*, 44:725, 1953.

[49] J. W. Dungey. *Cosmic Electrodynamics*. Cambridge University Press, Cambridge, Eng., 1958.

[50] J. W. Dungey. Interplanetary magnetic field and the auroral zones. *Phys. Rev. Lett.*, 6, 1961.

[51] J. P. Eastwood, T.-D. Phan, F. S. Mozer, M. A. Shay, M. Fujimoto, A. Retin, M. Hesse, A. Balogh, E. A. Lucek, and I. Dandouras. Multi-point observations of the Hall electromagnetic field and secondary island formation during magnetic reconnection. *J. Geophys. Res.*, 112:A06235, 2007.

[52] B. Edlén. An attempt to identify the emission lines in the spectrum of the solar corona. *Ark. Mat. Astron. Fys.*, 28B(1):1–4, 1941.

[53] B. Edlén. Die deutung der emissionlinien im spektrum der sonnenkorona. *Z. Astrophys.*, 22:30–64, 1942.

[54] J. Egedal and A. Fasoli. Single-particle dynamics in collisionless magnetic reconnection. *Phys. Rev. Lett*, 86:5047, 2001.

[55] J. Egedal, A. Lê, Y. Zhu, W. Daughton, M. Øieroset, T. Phan, R. P. Lin, and J. P. Eastwood. Cause of super-thermal electron heating during magnetotail reconnection. *Geophys. Res. Lett.*, 37:L10102, 2010.

[56] R. C. Elphic, C. A. Cattell, K. Takahashi, S. J. Bame, and C. T. Russell. ISEE-1 and 2 observations of magnetic flux ropes in the magnetotail: FTE's in the plasma sheet? *Geophys. Res. Lett.*, 13(7):648–651, 1986.

[57] A. G. Emslie, B. R. Dennis, G. D. Holman, and H. S. Hudson. Refinements to flare energy estimates: a followup to "Energy partition in two solar flare / CME events" by A. G. Emslie et al. *J. Geophys. Res.*, 110:A11103, 2005.

[58] D. H. Fairfield. Polar magnetic disturbances and the interplanetary magnetic field. *Space Res.*, 8:107–119, 1967.

[59] D. H. Fairfield and L. G. Cahill. Transition region magnetic field and polar magnetic disturbances. *J. Geophys. Res.*, 71:155–169, 1966.

[60] C. J. Farrugia, R. P. Rijnbeek, M. A. Saunders, D. J. Southwood, D. J. Rodgers, M. F. Smith, C. P. Chaloner, D. S. Hall, P. J. Christiansen, and L. J. C. Woolliscroft. A multi-instrument study of flux transfer event structure. *J. Geophys. Res.*, 93(A12):14465–14477, 1988.

[61] R. C. Fear, S. E. Milan, A. N. Fazakerley, E. A. Lucek, S. W. H. Cowley, and I. Dandouras. The azimuthal extent of three flux transfer events. *Ann. Geophys.*, 26:2353–2369, 2008.

[62] R. L. Fermo, J. F. Drake, M. Swisdak, and K.-J. Hwang. Comparison of a statistical model for magnetic islands in large current layers with hall mhd simulations and cluster fte observations. *J. Geophys. Res.*, 2011. In press; doi:10.1029/2010JA016271.

[63] K. Fujimoto. Time evolution of the electron diffusion region and the reconnection rate in fully kinetic and large system. *Phys. Plasmas*, 13:072904, 2006.

[64] H. P. Furth, J. Killeen, and M. N. Rosenbluth. Finite-resistivity instabilities of a sheet pinch. *Phys. Fluids*, 6(4):459, April 1963.

[65] E. Gaddy, R. Decker, M. K. Lockwood, L. Roufberg, G. Knutzen, and D. Marsh. The Solar Probe Plus solar array development and design. In *Photovoltaic Specialists Conference (PVSC), 2010 35th IEEE*, pages 717–722, June 2010.

[66] A. A. Galeev, R. Rosner, and G. S. Vaiana. Structured coronae of accretion disks. *Ap. J.*, 229:318–326, 1979.

[67] R. G. Giovanelli. Magnetic and electric phenomena in the sun's atmosphere associated with sunspots. *Mon. Not. R. Astron. Soc.*, 107:338, 1947.

[68] J. T. Gosling, S. Erkisson, R. M. Skoug, D. J. McComas, and R. J. Forsyth. Petschek-type reconnection exhausts in the solar wind well beyond 1 AU: Ulysses. *Ap. J.*, 644:613–621, 2006.

[69] J. T. Gosling, R. M. Skoug, and D. J. McComas. Direct evidence for magnetic reconnection in the solar wind near 1 AU. *Geophys. Res. Lett.*, 110:A01107, 2005.

[70] W. Grotrian. The question of the significance of the lines in the spectrum of the solar corona. *Naturwiss.*, 27:214, 1939.

[71] G. E. Hale. Some results and conclusions derived from a photographic study of the sun. *Astron. Astrophys.*, 11:811–815, 1892.

[72] G. E. Hale. On the probable existence of a magnetic field in sun-spots. *Ap. J.*, 28:315, 1908.

[73] G. E. Hale. Solar vortices (contributions from the Mt. wilson solar observatory, no. 26). *Ap. J.*, 28:100, 1908.

[74] E. G. Harris. On a plasma sheath separating regions of oppositely directed magnetic field. *Nuovo Cim.*, 23(1):115–121, 1962.

[75] H. Hasegawa, J. Wang, M. W. Dunlop, Z. Y. Pu, Q.-H. Zhang, B. Lavraud, M. G. G. T. Taylor, O. D. Constantinescu, J. Berchem, V. Angelopoulos, J. P. McFadden, H. U. Frey, E. V. Panov, M. Volwerk, and Y. V. Bogdanova. Evidence for a flux transfer event generated by multiple X-line reconnection at the magnetopause. *Geophys. Res. Lett.*, 37:L16101, 2010.

[76] M. Hesse and J. Birn. Plasmoid evolution in an extended magnetotail. *J. Geophys. Res.*, 96(A4):5683–5696, 1991.

[77] M. Hesse, Masha Kuznetsova, and M. Hoshino. The structure of the dissipation region for component reconnection: Particle simulations. *Geophys. Res. Lett.*, 29:1563, 2002.

[78] R. Hodgson. On a curious appearance seen in the sun. *Mon. Not. R. Astron. Soc.*, 20:15–16, 1859.

[79] E. W. Hones, Jr. Transient phenomena in the magnetotail and their relation to substorms. *Space Sci. Rev.*, 23:393, 1979.

[80] E. W. Hones, Jr., D. N. Baker, S. J. Bame, W. C. Feldman, J. T. Gosling, D. J. McComas, R. D. Zwickl, J. A. Slavin, E. J. Smith, and B. T. Tsurutani. Structure of the magnetotail at $220r_e$ and its response to geomagnetic activity. *Geophys. Res. Lett.*, 11(1):5–7, 1984.

[81] F. Hoyle. *Some recent researches in solar physics*. Cambridge [Eng.] University Press, Cambridge, Eng., 1949.

[82] Y.-M. Huang and A. Bhattacharjee. Scaling laws of resistive magnetohydrodynamic reconnection in the high-Lundquist-number, plasmoid-unstable regime. *Phys. Plasmas*, 17(6):062104, 2010.

[83] J. D. Huba, N. T. Gladd, and K. Papadopoulos. The lower-hybrid-drift instability as a source of anomalous resistivity for magnetic field reconnection. *Geophys. Res. Lett.*, 4:125, 1977.

[84] W. J. Hughes. The magnetopause, magnetotail, and magnetic reconnection. In M. G. Kivelson and C. T. Russell, editors, *Introduction to Space Physics*. Cambridge University Press, New York, 1995.

[85] K. Hurley, S. E. Boggs, D. M. Smith, R. C. Duncan, R. Lin, A. Zoglauer, S. Krucker, G. Hurford, H. Hudson, C. Wigger, W. Hajdas, C. Thompson, I. Mitrofanov, A. Sanin, W. Boynton, C. Fellows, A. von Kienlin, G. Lichti, A. Rau, and T. Cline. An exceptionally bright flare from SGR 1806-20 and the origins of short-duration *gamma*-ray bursts. *Nature*, 434:1098–1103, 2005.

[86] A. Ieda, S. Machida, T. Mukai, Y. Saito, T. Yamamoto, A. Nishida, T. Teresawa, and S. Kokubun. Statistical analysis of the plasmoid evolution with Geotail observations. *J. Geophys. Res.*, 103(A3):4453–4465, 1998.

[87] C. M. Jackman, N. Achilleos, E. J. Bunce, S. W. H. Cowley, M. K. Dougherty, G. H. Jones, S. E. Milan, and E. J. Smith. Interplanetary magnetic field at 9 au during the declining phase of the solar cycle and its implications for saturn's magnetospheric dynamics. *J. Geophys. Res.*, 109:A11203, 2004.

[88] J. R. Jokipii and B. Thomas. Effects of drift on the transport of cosmic rays IV. Modulation by a wavy interplanetary current sheet. *Ap. J.*, pages 1115–1122, 1981.

[89] B. B. Kadomtsev. On disruptive instability in tokamaks. *Fiz. Plazmy*, 1:710–715, 1975.

[90] H. Karimabadi, W. Daughton, and J. Scudder. Multi-scale structure of the electron diffusion region. *Geophys. Res. Lett.*, 34:L13104, 2007.

[91] W. T. Kelvin. Hydrokinetic solutions and observations. *Phil. Mag.*, 4:362–377, 1871.

[92] W. T. Kelvin. President's address. In *Proc. R. Soc.*, volume 52, pages 299–310, 1892.

[93] A. Klimas, M. Hesse, and S. Zenitani. Particle-in-cell simulation of collisionless reconnection with open outflow boundaries. *Phys. Plasmas*, 15:082102, 2008.

[94] Y.-K. Ko, J. C. Raymond, J. Lin, G. Lawrence, J. Li, and A. Fludra. Dynamical and physical properties of a post-coronal mass ejection current sheet. *Ap. J.*, 594:1068–1084, 2003.

[95] S. Krucker, H. S. Hudson, L. Glesener, S. M. White, S. Masuda, J.-P. Wuelser, and R. P. Lin. Measurements of the coronal acceleration of a solar flare. *Ap. J.*, 714:1108–1119, 2010.

[96] I. Langmuir. The interaction of electron and positive ion space charges in cathode sheaths. *Phys. Rev.*, 39:954–989, 1929.

[97] G. Lapenta. Self-feeding turbulent magnetic reconnection on macroscopic scales. *Phys. Rev. Lett.*, 100:235001, 2008.

[98] A. Lazarian and M. Opher. A model of acceleration of anomalous cosmic rays by reconnection in the heliosheath. *Ap. J.*, 703(1):8–21, 2009.

[99] L. C. Lee and Z. F. Fu. A theory of magnetic flux transfer at the earth's magnetopause. *Geophys. Res. Lett.*, 12:105, 1985.

[100] J. Lin, Y.-K. Ko, L. Sui, J. C. Raymond, G. A. Stenborg, Y. Jiang, S. Zhao, and S. Mancuso. Direct observations of the magnetic reconnection site of an eruption on 2003 November 18. *Ap. J.*, 622:1251–1264, 2005.

[101] R. P. Lin and H. S. Hudson. 10-100keV electron acceleration and emission from solar flares. *Sol. Phys.*, 17:412–435, 1971.

[102] R. P. Lin and H. S. Hudson. Non-thermal processes in solar flares. *Sol. Phys.*, 50(1):153–178, 1976.

[103] F. A. Lindemann. Note on the theory of magnetic storms. *Philos. Mag.*, 39:669–684, 1919.

[104] M. G. Linton and D. W. Longcope. A model for patchy reconnection in three dimensions. *Ap. J.*, 642:1177–1192, 2006.

[105] G. D. Liveing and J. Dewar. Note on the unknown chromospheric substance of young. *Proc. R. Soc. Lond.*, 28:475–477, 1878.

[106] N. F. Loureiro, A. A. Schekochihin, and S.C. Cowley. Instability of current sheets and formation of plasmoid chains. *Phys. Plasmas*, 14:100703, 2007.

[107] A. T. Y. Lui, P. H. Yoon, C. Mok, and C.-M. Ryu. Inverse cascade feature in current disruption. *J. Geophys. Res.*, 113:A00C06, 2008.

[108] H. B. Maris and E. O. Hulburt. A theory of auroras and magnetic storms. *Phys. Rev.*, 33:412–431, 1929.

[109] E. W. Maunder. Magnetic disturbances, 1882 to 1903, as recorded at the royal observatory, greenwich, and their association with sunspots. *Mon. Not. R. Astron. Soc.*, 65:2–34, 1905.

[110] H. J. McAndrews, C. J. Owen, M. F. Thomsen, B. Lavraud, A. J. Coates, M. K. Dougherty, and D. T. Young. Evidence for reconnection at Saturn's magnetopause. *J. Geophys. Res.*, 113:A04210, 2008.

[111] D. E. McKenzie and H. S. Hudson. X-ray observations of motions and structure above a solar flare arcade. *Ap. J.*, 519:L93–L96, 2009.

[112] D. E. McKenzie and S. L. Savage. Quantitative examination of supra-arcade downflows in eruptive solar flares. *Ap. J.*, 697:1569–2009, 2009.

[113] D. E. McKenzie and S. L. Savage. Distribution functions of sizes and fluxes determined from supra-arcade downflows. *Ap. J.*, 735:L6, 2011.

[114] F. S. Mozer, S. D. Bale, and T. D. Phan. Evidence of diffusion regions at a subsolar magnetopause crossing. *Phys. Rev. Lett.*, 89:015002, 2002.

[115] T. Nagai, M. Fujimoto, Y. Saito, S. Machida, T. Teresawa, R. Nakamura, T. Yamamoto, T. Mukai, A. Nishida, and S. Kokubun. Structure and dynamics of magnetic reconnection for substorm onsets with Geotail observations. *J. Geophys. Res.*, 103(A3):4419–4440, 1998.

[116] T. Nagai, K. Takahash, H. Kawano, T. Yamamoto, S. Kokubun, and A. Nishida. Initial GEOTAIL survey of magnetic substorm signatures in the magnetotail. *Geophys. Res. Lett.*, 21(25):2991–2994, 1994.

[117] J. D. Nichols, S. W. H. Cowley, and D. J. McComas. Magnetopause reconnection rate estimates for Jupiter's magnetosphere based on interplanetary measurements at 5 au. *Ann. Geophys.*, 24:393–406, 2006.

[118] M. Øieroset, R. P. Lin, T. D. Phan, D. E. Larson, and S. D. Bale. Evidence for electron acceleration up to 300keV in the magnetic reconnection diffusion region in the earth's magnetotail. *Phys. Rev. Lett.*, 89:195001–1–4, 2002.

[119] M. Øieroset, T. D. Phan, M. Fujimoto, R. P. Lin, and R. P. Lepping. In situ detection of collisionless reconnection in the earth's magnetotail. *Nature*, 412:417, 2001.

[120] M. Oka, T.-D. Phan, S. Krucker, M. Fujimoto, and I. Shinohara. Electron acceleration by multi-island coalescence. *Ap. J.*, 714:915–926, 2010.

[121] N. Omidi and D. G. Sibeck. Flux transfer events in the cusp. *Geophys. Res. Lett.*, 34:L04106, 2007.

[122] M. Opher, J. F. Drake, M. Swisdak, K. M. Schoeffler, J. D. Richardson, R. B. Decker, and G. Toth. Is the magnetic field in the heliosheath laminar or a turbulent sheet of bubbles? *Ap. J.*, 734(1):71, 2011.

[123] E. N. Parker. Dynamics of the interplanetary gas and magnetic fields. *Ap. J.*, 128:664, 1958.

[124] E. N. Parker. The solar-flare phenomenon and the theory of reconnection and annihilation of magnetic fields. *Ap. J.*, 8:177, 1963.

[125] E. N. Parker. Magnetic neutral sheets in evolving fields: II. Formation of the solar corona. *Ap. J.*, 264:642–647, 1983.

[126] E. N. Parker. Nanoflares and the solar x-ray corona. *Ap. J.*, 330:474–479, 1988.

[127] H. E. Petschek. Magnetic field annihilation. In W. N. Ness, editor, *AAS/NASA Symposium on the Physics of Solar Flares*, page 425. NASA, Washington, DC, 1964.

[128] T. D. Phan, J. T. Gosling, M. S. Davis, R. M. Skoug, M. Øieroset, R. P. Lin, R. P. Lepping, D. J. McComas, C. W. Smith, H. Reme, and A. Balogh. A magnetic reconnection x-line extending more than 390 earth radii in the solar wind. *Nature*, 439:175, 2006.

[129] T. D. Phan, G. Paschmann, C. Twitty, F. S. Mozer, J. T. Gosling, J. P. Eastwood, M. Øieroset, H. Reme, and E. A. Lucek. Evidence for magnetic reconnection initiated in the magnetosheath. *Geophys. Res. Lett.*, 34:L14104, 2007.

[130] S. C. Prager, A. F. Almagri, S. Assadi, J. A. Beckstead, R. N. Dexter, D. J. Den Hartog, G. Chartas, S. A. Hokin, T. W. Lovell, T. D. Rempel, J. S. Sarff, W. Shen, C. W. Spragins, and J. C. Sprott. First results from the Madison Symmetric Torus reversed field pinch. *Phys. Fluids B*, 2:1367, 1990.

[131] E. R. Priest and T. G. Forbes. The magnetic nature of solar flares. *Astron. Astrophys. Rev.*, 10(4):313–377, 2002.

[132] P. L. Pritchett. Geospace environmental modeling magnetic reconnection challenge: simulations with a full particle electromagnetic code. *J. Geophys. Res.*, 106:3783, 2001.

[133] P. L. Pritchett and F. V. Coroniti. Three-dimensional collisionless magnetic reconnection in the presence of a guide field. *J. Geophys. Res.*, 109:A01220, 2004.

[134] P. L. Pritchett and C. C. Wu. Coalescence of magnetic islands. *Phys. Fluids*, 22(11):2140–2146, 1979.

[135] J. Raeder. Flux tranfer events: 1. Generation mechanism for nearly southward IMF. *Ann. Geophys.*, 24:381, 2006.

[136] Y. Ren, M. Yamada, S. Gerhardt, H. Ji, Russell Kulsrud, and A. Kuritsyn. Experimental verification of the Hall effect during magnetic reconnection in a laboratory plasma. *Phys. Rev. Lett.*, 95:005003, 2005.

[137] R. P. Rijnbeek, S. W. H. Cowley, D. J. Southwood, and C. T. Russell. A survey of dayside flux transfer events observed by isee 1 and 2 magnetometers. *J. Geophys. Res.*, 89(A2):786–800, 1984.

[138] C. R. Robinson and B. W. Bopp. A "helium flare" on the active G5 dwarf Kappa Ceti. In J. L. Linsky and R. E. Stencel, editors, *Cool Stars, Stellar Systems and the Sun*, volume 291 of *Lecture Notes in Physics, Berlin Springer Verlag*, page 509, 1987.

[139] B. B. Rossi and S. Olbert. *Introduction to the Physics of Space*. McGraw-Hill, New York, 1970.

[140] A. Runov, R. Nakamura, W. Baumjohann, R. A. Treumann, T. L. Zhang, M. Volwerk, Z. Vörös, A. Balogh, K.-H. Glabmeier, B. Klecker, H. Réme, and L. Kistler. Current sheet structure near magnetic X-line observed by Cluster. *Geophys. Res. Lett.*, 30(11):1579, 2003.

[141] C. T. Russell and R. C. Elphic. Initial isee magnetometer results: Magnetopause observations. *Space Science Rev.*, 22:681, 1978.

[142] C. T. Russell and R. C. Elphic. ISEE observations of flux transfer events at the dayside magnetopause. *Geophys. Res. Lett.*, 6:33, 1979.

[143] C. T. Russell, K. K. Khurana, D. E. Huddleston, and M. G. Kivelson. Localized reconnection in the near Jovian magnetotail. *Science*, 280:1061–1064, 1998.

[144] R. Samtaney, N. F. Loureiro, D. A. Uzdensky, A. A. Schekochihin, and S. C. Cowley. Formation of plasmoid chains in magnetic reconnection. *Phys. Rev. Lett.*, 103:105004, 2009.

[145] T. Sato and T. Hayashi. Externally driven magnetic reconnection and a powerful magnetic energy converter. *Phys. Fluids*, 22:1189, 1979.

[146] M. A. Saunders, C. T. Russell, and N. Sckopke. Flux transfer events: scale size and interior structure. *Geophys. Res. Lett.*, 11:131–134, 1984.

[147] S. L. Savage. *Using extreme ultra-violet and soft X-ray observations as probes of magnetic reconnection during solar flares*. PhD thesis, Montana State University, 2010.

[148] S. L. Savage and D. E. McKenzie. Quantitative examination of a large sample of supra-arcade downflows in eruptive solar flares. *Ap. J.*, 730:98, 2011.

[149] S. L. Savage, D. E. McKenzie, K. K. Reeves, T. G. Forbes, and D. W. Longcope. Reconnection outflows and current sheet observed with Hinode/XRT in the 2008 April 9 "Cartwheel CME" flare. *Ap. J.*, 722:329–342, 2010.

[150] E. Schatzman. The heating of the solar corona and chromosphere. *Ann. Astrophys.*, 12:203, 1949.

[151] M. Scholer. Magnetic flux transfer at the magnetopause based on single x line bursty reconnection. *Geophys. Res. Lett.*, 15:291, 1988.

[152] J. D. Scudder, F. S. Mozer, N. C. Maynard, and C. T. Russell. Fingerprints of collisionless reconnection at the separator, I, Ambipolar-Hall signatures. *J. Geophys. Res.*, 107:1294, 2002.

[153] M. A. Shay, J. F. Drake, B. N. Rogers, and R. E. Denton. The scaling of collisionless, magnetic reconnection for large systems. *Geophys. Res. Lett.*, 26:2163, 1999.

[154] M. A. Shay, J. F. Drake, and M. Swisdak. Two-scale structure of the electron dissipation region during collisionless magnetic reconnection. *Phys. Rev. Lett.*, 99:155002, 2007.

[155] M. A. Shay, J. F. Drake, M. Swisdak, and B. N. Rogers. The scaling of embedded collisionless reconnection. *Phys. Plasmas*, 11(5):2199, 2004.

[156] N. R. Sheeley, H. P. Warren, and Y.-M. Wang. The origin of postflare loops. *Astrophys. J.*, 616:1224, 2004.

[157] L. S. Shepherd and P. A. Cassak. Comparison of secondary islands in collisional reconnection to hall reconnection. *Phys. Rev. Lett.*, 105:015004, 2010.

[158] K. Shibata, S. Masuda, M. Shimojo, H. Hara, T. Yokoyama, S. Tsuneta, T. Kosugi, and Y. Ogawara. Hot-plasma ejections associated with compact-loop solar flares. *Ap. J.*, 451:L83–L85, 1995.

[159] K. Shibata and S. Tanuma. Plasmoid-induced-reconnection and fractal reconnection. *Earth, Planets and Space*, 53:473–482, 2001.

[160] A. Y. Shih, R. P. Lin, and D. M. Smith. RHESSI observations of the proportional acceleration of relativistic > 0.3 MeV electrons and > 30 MeV protons in solar flares. *Ap. J.*, 698:L152–L157, 2009.

[161] D. G. Sibeck, M. Kuznetsova, V. Angelopoulos, K.-H. Glaßmeier, and J. P. McFadden. Crater FTEs: Simulation results and THEMIS observations. *Geophys. Res. Lett.*, 35:L17S06, 2008.

[162] J. A. Slavin, M. H. Acuña, B. J. Anderson, D. N. Baker, M. Benna, S. A. Boardsen, G. Gloeckler, R. E. Gold, G. C. Ho, H. Korth, S. M. Krimigis, R. L. McNutt, Jr., J. M. Raines, M. Sarantos, D. Schriver, S. C. Solomon, P. Trávníček, and T. H. Zurbuchen. MESSENGER observations of magnetic reconnection in Mercury's magnetosphere. *Science*, 324:606–610, 2009.

[163] J. A. Slavin, B. J. Anderson, D. N. Baker, M. Benna, S. A. Boardsen, G. Gloeckler, R. E. Gold, G. C. Ho, H. Korth, S. M. Krimigis, R. L. McNutt, Jr., L. R. Nittler, J. M. Raines, M. Sarantos, D. Schriver, S. C. Solomon, R. D. Starr, P. Trávníček, and T. H. Zurbuchen. MESSENGER observations of extreme loading and unloading of Mercury's magnetic tail. *Science*, 329:665–668, 2010.

[164] J. A. Slavin, R. P. Lepping, J. Gjerloev, D. H. Fairfield, M. Hesse, C. J. Owen, M. B. Moldwin, T. Nagai, A. Ieda, and T. Mukai. Geotail observations of magnetic flux ropes in the plasma sheet. *J. Geophys. Res.*, 108(A1):1015, 2003.

[165] J. A. Slavin, C. J. Owen, M. M. Kuznetsova, and M. Hesse. ISEE 3 observations of plasmoids with flux rope magnetic topologies. *Geophys. Res. Lett.*, 22(15):2061–2064, 1995.

[166] J. A. Slavin, M. F. Smith, E. L. Mazur, D. N. Baker, E. W. Hones, Jr., T. Iyemori, and E. W. Greenstadt. ISEE 3 observations of traveling compression regions in the Earth's magnetotail. *J. Geophys. Res.*, 98(A9):15425–15446, 1993.

[167] B. U. Ö. Sonnerup. Magnetopause structure during the magnetic storm of September 24, 1961. *J. Geophys. Res.*, 76(28):6717–6735, 1971.

[168] B. U. Ö. Sonnerup. Magnetic field reconnection. In L. J. Lanzerotti, C. F. Kennel, and E. N. Parker, editors, *Solar System Plasma Physics*, volume 3, page 46. North Halland Pub., Amsterdam, 1979.

[169] D. J. Southwood, C. J. Farrugia, and M. A. Saunders. What are flux transfer events? *Planet. Space Sci.*, 36:503–508, 1988.

[170] E. C. Stone, A. C. Cummings, F. B. McDonald, B. C. Heikkila, N. Lal, and W. R. Webber. Voyager 1 explores the termination shock region and the heliosheath beyond. *Science*, 309:2017–2020, 2005.

[171] E. C. Stone, A. C. Cummings, F. B. McDonald, B. C. Heikkila, N. Lal, and W. R. Webber. An asymmetric solar wind termination shock. *Nature*, 454:71–74, 2008.

[172] T. E. Stringer. Electrostatic instabilities in current-carrying and counterstreaming plasmas. *J. Nucl. Energy, Part C Plasma Phys.*, 6:267–279, 1964.

[173] L. Sui and G. D. Holman. Evidence for the formation of a large-scale current sheet in a solar flare. *Ap. J.*, 596:L251–L254, 2003.

[174] P. A. Sweet. The neutral point theory of solar flares. In B. Lehnert, editor, *Electromagnetic Phenomena in Cosmical Physics*, page 123. Cambridge University Press, New York, 1958.

[175] M. Swisdak and J. F. Drake. Orientation of the reconnection x-line. *Geophys. Res. Lett.*, 34:L11106, 2007.

[176] M. Tanaka. Asymmetry and thermal effects due to parallel motion of electrons in collisionless magnetic reconnection. *Phys. Plasmas*, 3:4010, 1996.

[177] S. Tanuma, T. Yokoyama, T. Kudoh, and K. Shibata. Two-dimensional magnetohydrodynamic numerical simulations of magnetic reconnection triggered by a supernova shock in the interstellar medium: generation of X-ray gas in the galaxy. *Ap. J.*, 551(1):312, 2001.

[178] W.-L. Teh, S. Eriksson B. U. Ö Sonnerup, R. Ergun, V. Angelopoulos, K.-H. Glassmeier, J. P. McFadden, and J. W. Bonnell. THEMIS observations of a secondary magnetic island within the hall electromagnetic field region at the magnetopause. *Geophys. Res. Lett.*, 37:L21102, 2010.

[179] U. Trottenberg, C. W. Oosterlee, and A. Schüller. *Multigrid*. Academic Press, San Diego, CA, 2001.

[180] S. Tsuneta. Moving plasmoid and formation of the neutral sheet in a solar flare. *Ap. J.*, 483:507–514, 1997.

[181] D. A. Uzdensky, N. F. Loureiro, and A. A. Schekochihin. Fast magnetic reconnection in the plasmoid-dominated regime. *Phys. Rev. Lett.*, 105(23):235002, 2010.

[182] S. von Goeler, W. Stodiek, and N. R. Sautoff. Studies of internal disruptions and $m = 1$ oscillations in tokamak discharges with soft x-ray techniques. *Phys. Rev. Lett.*, 1974.

[183] H. von Helmholtz. Über discontinuierliche Flüssigkeits bewegungen. *Monats. Königl. Preuss. Akad. Wiss. Berlin*, 23:215, 1868.

[184] Y. L. Wang, R. C. Elphic, B. Lavraud, M. G. G. T. Taylor, J. Birn, J. Raeder, C. T. Russell, H. Kawano, Q.-G. Zong, H. Zhang, X. X. Zhang, and R. H. Friedel. Initial results of high-latitude magnetopause and low-latitude flank flux transfer events from 3 years of Cluster observations. *J. Geophys. Res.*, 110:A11221, 2005.

[185] Y. L. Wang, R. C. Elphic, B. Lavraud, M. G. G. T. Taylor, J. Birn, J. Raeder, C. T. Russell, H. Kawano, Q.-G. Zong, H. Zhang, X. X. Zhang, and R. H. Friedel. Initial results of high-latitude magnetopause and low-latitude flank flux transfer events from 3 years of Cluster observations. *J. Geophys. Res.*, 110:A11221, 2005.

[186] M. Yamada, H. Ji, S. Hsu, T. Carter, R. Kulsrud, N. Bretz, F. Jobes, Y. Ono, and F. Perkins. Study of driven magnetic reconnection in a laboratory plasma. *Phys. Plasmas*, 4:1936, 1997.

[187] A. Zeiler, D. Biskamp, J. F. Drake, B. N. Rogers, M. A. Shay, and M. Scholer. Three-dimensional particle simulations of collisionless magnetic reconnection. *J. Geophys. Res.*, 107:1230–1–9, 2002.

[188] H. Zhang, K. K. Khurana, M. G. Kivelson, V. Angelopoulos, Z. Y. Pu, Q.-G. Zong, J. Liu, and X.-Z. Zhou. Modeling a force-free flux transfer event probed by multiple Time History of Events and Macroscale Interactions during Substorms (THEMIS) spacecraft. *J. Geophys. Res.*, 113:A00C05, 2008.

[189] H. Zhang, M. G. Kivelson, K. K. Khurana, J. McFadden, R. J. Walker, V. Angelopoulos, J. M. Weygand, T. Phan, D. Larson, K.-H. Glassmeier, and H. U. Auster. Evidence that crater flux transfer events are initial stages of typical flux transfer events. *J. Geophys. Res.*, 115:A08229, 2010.

[190] Q.-G. Zong, T. A. Fritz, Z. Y. Pu, S. Y. Fu, D. N. Baker, H. Zhang, A. T. Lui, I. Vogiatzis, K.-H. Glassmeier, A. Korth, P. W. Daly, A. Balogh, and H. Reme. Cluster observations of earthward flowing plasmoid in the tail. *Geophys. Res. Lett.*, 31:L18803, 2004.